

Master Thesis

Preliminary Design Methodology Of Concrete Gravity-Based Foundations For Offshore Wind

European Wind Energy Master

Joey Hu

Master Thesis

Preliminary Design Methodology Of Concrete Gravity-Based Foundations For Offshore Wind

by

Joey Hu

to obtain the degree of Master of Science in Offshore Engineering at Delft University of Technology
& Master of Science in Technology-Wind Energy at Norwegian University of Science and Technology.

University	Student Number
TU Delft	4564413
NTNU	557405

Project duration: February, 2022 – August, 2022
Thesis committee: Ir. A. C. M. Van der Stap, TU Delft - chairman
Ir. J. Hoving, TU Delft - supervisor
Prof. dr. ir. T. Kristiansen, NTNU - supervisor
Prof. dr. ir. Z. Gao, NTNU - committee member
Dr. Ir. A. Verbart, Rambøll - supervisor

Cover: General representation of a gravity-based foundation design
for offshore wind (by courtesy of Rambøll)

Preface

This master thesis project: "Preliminary Design Methodology For Concrete Gravity-Based Offshore Wind Foundations", has been written to fulfil the graduation requirements of the European Wind Energy Master at the Delft University of Technology (TU Delft) and the Norwegian University of Science and Technology (NTNU). Before this research, an in-depth literature study of wave theories and hydrodynamic models was executed from November 2021 to January 2022.

The project was carried out at the wind department of Rambøll in Copenhagen, Denmark, from February 2022 to July 2022. As this was a collaboration between Rambøll, TU Delft, and NTNU, I have been fortunate enough to have received support and knowledge from all involved parties.

First, I would like to thank all the people at Rambøll for accepting me as part of the team since the first day. Although the past few months have flown by, I have noticed that Rambøll is an inspiring company that walks the talk regarding sustainability and truly cares about its employees. I am very grateful to Filipe Ângelo and Thomas Brink Laursen for granting me the opportunity to do my thesis in their department. Furthermore, I would like to thank my supervisor Alexander Verbart for guiding me throughout the whole process and directing me to the right people. You have been an amazing mentor and even became my friend in the past few months. Alberto Vera Vázquez was incredibly helpful during the structural modeling and natural frequency analysis in ROSAP, and I had a lot of fun during our after-work climbing sessions.

Additionally, I want to thank Tommi Højer Bondum and Baturay Batarlar from the concrete department for their cooperation and immense knowledge regarding the design guidelines and geotechnical stability requirements for offshore concrete structures. Last but not least, I am very grateful to Michael Karch and Matti Schilling from the wind department in Hamburg, Germany, for providing their extensive knowledge and scripts of hydrodynamic load modelling. This ever-growing offshore wind industry is still tiny, and I am sure I will meet many of you again in the near future.

Secondly, I am very grateful for the exceptional assistance from both my university supervisors. From TU Delft, I am impressed with Jeroen Hoving's ability to keep an eye on the ball and simplify any complex problem by working in a structured manner. This ensured I had a clear overview of my process throughout my thesis. From NTNU, I was honoured to have access to the immense knowledge of Trygve Kristiansen on hydrodynamics. I have learned a lot from our many deep discussions, and I am very grateful for that. Additionally, I would like to thank Zhen Gao for assisting me with WAMIT, even though you were officially not my supervisor.

Lastly, I would like to thank my beloved mother, girlfriend Yaslin Li, family, and friends for their unconditional love, support, and understanding throughout my master's program. Moving to a different country every six months can be stressful for the people around you. Therefore, I am very fortunate to have this kind of support throughout all the ups and downs. Furthermore, I am glad I decided to do the European Wind Energy Master. Besides the thorough knowledge about offshore wind, I have made countless friends and incredible experiences, which I will hold dear for the rest of my life.

*Joey Hu
Copenhagen, August 2022*

Abstract

To expand the economic operating range of offshore wind farms, less common but innovative solutions regarding support structures should be considered. To increase the popularity of gravity-based foundations (GBF) within the offshore wind industry, a better understanding of the hydrodynamics on GBFs, as well as an improved insight in the optimal design process for these structures is essential. Therefore, this thesis proposes a design methodology (hydrodynamic model, structural model, wind loads, foundation stability verification, and design guidelines) for the preliminary design of concrete GBFs for offshore wind turbines. The proposed methodology is developed for semi-floating conical GBFs, however it is a universal methodology that can be used for other types of concrete GBFs.

The hydrodynamic GBF load model is based on a linear potential flow solution created in the diffraction analysis program OrcaFlex, which requires a mesh panel model with sufficient elements to ensure convergence. This mesh panel model can be easily generated using a parametric design tool for GBFs in MATLAB. The hydrodynamic load model was validated using Computational Fluid Dynamics (CFD) simulations of seven wave conditions. Although the linear potential flow results slightly deviate from the CFD data, they provide a sufficiently accurate and highly cost-efficient approximation of the hydrodynamic loads during the conceptual design phase. For the detailed design phase, CFD is still required since it represents the state-of-the-art regarding hydrodynamic load modelling. Nevertheless, the accuracy depends on the user's knowledge and the applied turbulent models, hence it should only be considered as a tool rather than a complete model.

A simplified structural model was created in Rambøll Offshore Structural Analysis Programs (ROSAP) to perform a natural frequency analysis to ensure structural integrity. Due to the high stiffness of GBFs, it results in natural frequencies that are above the peak wave, wind, and 1P (rotor) frequency. This makes it reasonably easy to design the first natural frequency of the structure to be within the desired soft-stiff region, and thus resonance is only a minor challenge. The main concerns for GBFs rather depend on the weight and cost-efficiency of manufacturing, transportation, and installation.

The initial design is based on the environmental conditions, wind turbine data, and design guidelines. Since the guidelines are based on standard industry practice, it does not guarantee an optimal starting point for every project. Therefore, an iterative optimization procedure of the design will always be required. The complete model is verified using design checks based on industry standards, which ensures foundation stability for the primary limit states. These checks utilize simplified geotechnical calculations and partial load safety factors depending on the limit state.

The requirements for foundation stability are often driven by the size and weight of the structure. Therefore, sensitivity analyses were performed with various design parameters to identify the main factors influencing the design. In essence, if the weight or size of the structure increases, it will enhance the foundation's stability despite the increasing hydrodynamic loads. Additionally, as the corresponding weight increase is always larger than the stiffness increase, the first natural frequency of the GBF will always decrease with size increase.

As designs often have multiple objectives, the optimal design depends on the particular objective considered and thereby numerous optimal designs may exist. For a GBF, these objectives are often related to weight, costs, or even both. Furthermore, they can vary for different phases of the construction, transportation, installation, and operation of the wind turbine foundation. Generally, a combination of design objectives with varying priorities should be considered. In addition, implementing optimization algorithms is recommended as manual preliminary design optimization is labour-intensive and has difficulties taking into account all the various design objectives.

For future research, it is recommended to test the universality of this methodology. This can be done by modelling GBFs of varying shapes over a broad range of water depths and wave conditions. Additionally, more load conditions should be examined for a complete representative design to ensure safety within any scenario. Lastly, further investigations should be conducted regarding fully nonlinear wave models in the far-field combined with CFD simulations in the near-field.

Contents

Preface	i
Abstract	ii
Nomenclature	xiv
1 Introduction to offshore gravity-based foundation design	1
1.1 Outlook for offshore wind energy	1
1.2 Types of offshore support structures	3
1.3 Design of Gravity-Based Foundations	5
1.4 Research motivation and objectives	7
1.5 Structure of report	8
2 Theoretical background of wave-structure interaction	9
2.1 Hydrodynamic load models for offshore structures	9
2.1.1 Wave loads on slender cylinders: Morison equation	9
2.1.2 Empirical hydrodynamic coefficients	10
2.1.3 Wave loads on large cylinders: MacCamy-Fuchs diffraction theory	12
2.1.4 Wave loads on large bodies: linear potential flow	13
2.2 Computational Fluid Dynamics for offshore structures	14
2.2.1 Mesh and Domain	16
2.2.2 Turbulence models	16
2.2.3 Boundary layers	17
2.2.4 Multi-phase flow modeling	18
2.2.5 Conclusion regarding Computational Fluid Dynamics	19
2.3 Additional modeling factors	19
2.3.1 Irregularity	19
2.3.2 Tidal current	20
2.3.3 Breaking waves	20
2.3.4 Directionality	21
2.3.5 Ocean water properties	21
2.4 Summary of literature study	21

3	Description of hydrodynamic load model for Gravity-Based Foundations	22
3.1	Additional research regarding hydrodynamic load models	22
3.1.1	Total overturning moment based on a linear potential flow solution	22
3.1.2	Influence of conical shape on wave loads	25
3.2	Introduction to reference study for the validation of the hydrodynamic load model	27
3.3	Hydrodynamic load model based on linear potential flow	31
4	Validation of hydrodynamic load model for Gravity-Based Foundations	34
4.1	Validation of results using Computational Fluid Dynamics	34
4.2	Comparison with monopile	37
4.3	Comparison with cone study	39
4.4	Research regarding additional hydrodynamic effects	39
4.4.1	Wave loads up to the instantaneous linear free surface	40
4.4.2	Nonlinear wave loads	43
4.4.3	Contribution of drag load	44
4.5	Conclusion of hydrodynamic load model for GBFs	47
5	Design basis for Gravity-Based Foundations	48
5.1	Introduction to case study for the design basis	48
5.1.1	Environmental conditions	48
5.1.2	Initial design dimensions for the GBF	49
5.2	Environmental loads	51
5.2.1	Hydrodynamic loading	51
5.2.2	Wind turbine data and wind loading	53
5.3	Design checks of concrete Gravity-Based Foundations for offshore wind	54
5.3.1	Natural frequency analysis	55
5.3.2	Design load cases	57
5.3.3	Ultimate Limit State	58
5.3.4	Serviceability Limit State	61
5.3.5	Manufacturability of the structure	62
5.4	Scour protection	62
5.5	Preliminary analysis of initial design	63
6	Preliminary design based on sensitivity analysis	64
6.1	Sensitivity analysis of design parameters	64
6.1.1	Influence of ballast density	64

6.1.2	Influence of footprint	67
6.1.3	Influence of cone height	69
6.2	Sensitivity analysis for optimization	71
6.2.1	Influence of conical shape on the bearing capacity	72
6.2.2	Influence of conical shape on the natural frequency	73
6.2.3	Influence of conical shape on the cone slope angle	73
6.2.4	Influence of conical shape on the total concrete weight	74
6.3	Optimal preliminary design based on objectives	75
6.3.1	Minimal concrete material and cheapest ballast material	76
6.3.2	Ease of manufacturing	77
6.3.3	Balanced design	79
7	Methodology for preliminary design of gravity-based offshore wind foundations	80
8	Conclusion and Recommendations	82
	References	84
A	Data from literature study	88
B	Results of hydrodynamic load model validation	89
B.1	Comparison between CFD and LPF (OrcaWave)	89
B.2	Comparison between monopile and reference GBF	91
B.3	Comparison between first-order linear potential flow and second-order nonlinear potential flow	93
C	Scatter bin diagram for SLS loads	96
D	Sensitivity analysis results	98
D.1	Base diameter sensitivity analysis	98
D.2	Transition point sensitivity analysis	100
D.3	Optimization analysis results for preliminary design	101
D.4	Three-dimensional plots of sensitivity analysis	105

List of Figures

1.1	Annual offshore wind capacity additions, historical and future values	1
1.2	Global weighted average and range for total installed costs, capacity factors, and LCOE for offshore wind farms	2
1.3	Relationship between average distance from shore and water depth for offshore wind farms, 2000-2020	2
1.4	Capital expenditures for a reference fixed-bottom offshore wind farm	3
1.5	Types of common offshore wind turbine foundations, fixed and floating concepts	3
1.6	Cumulative number of installed foundations divided per concept	4
1.7	Gravity-based foundation under construction at Thornton bank offshore wind farm	5
1.8	Preliminary design workflow for concrete gravity-based offshore wind foundations.	6
2.1	Visualization of inline Morison forces on a section of a slender vertical cylinder	10
2.2	Inertial coefficient C_M as a function of KC for smooth cylinders.	11
2.3	MacCamy-Fuchs-corrected inertial coefficient $C_{M,MCF}$ as a function of the diameter-wavelength ratio $\frac{D}{\lambda}$	13
2.4	Example flowchart for a Computational Fluid Dynamics simulation	15
2.5	Overview of various turbulence models	16
2.6	Boundary layer velocity development on a flat plate	17
2.7	Visual representation of the volume of fluid method interface for an ocean wave.	18
2.8	Visualization of an irregular sea consisting of a summation of regular waves	20
3.1	Representation of a horizontal beam model for a gravity-based foundation subjected to wave loads.	23
3.2	Sign convention of a GBF model using both beam elements and panels	23
3.3	Total overturning moment on a reference GBF	24
3.4	Examined structures in the cone study	25
3.5	Hydrodynamic loads on monopile ($D = 7.0$ m) for varying wave periods	26
3.6	Hydrodynamic loads on cone ($D_{bot} = 8.0$ m) for varying wave periods	26
3.7	Hydrodynamic loads on cone ($D_{bot} = 14.0$ m) for varying wave periods	26
3.8	Hydrodynamic loads on cone ($D_{bot} = 20.0$ m) for varying wave periods	27
3.9	Hydrodynamic loads on cone ($D_{bot} = 30.0$ m) for varying wave periods	27

3.10 Hydrodynamic loads on cone ($D_{bot} = 40.0$ m) for varying wave periods	27
3.11 Hydrodynamic loads on cone ($D_{bot} = 60.0$ m) for varying wave periods	27
3.12 Dimensions of the reference gravity-based foundation with a water depth d of 36.8 m . .	28
3.13 Wave loads regime for all wave simulations with the reference gravity-based foundation	29
3.14 Wave theory suitability and wave breaking check for all wave simulations	30
3.15 Mesh panel model for a gravity-based foundation	32
3.16 Reference gravity-based foundation modelled in OrcaFlex	33
4.1 Hydrodynamic loads comparison for wave 3, using linear potential flow and Computation Fluid Dynamics	35
4.2 Base shear w.r.t. wave height	36
4.3 Base shear w.r.t. wave period	36
4.4 Overturning moment w.r.t. wave height	37
4.5 Overturning moment w.r.t. wave period	37
4.6 Reference gravity-based foundation and monopile modelled in OrcaWave	37
4.7 Hydrodynamic loads comparison between a gravity-based foundation and a monopile .	38
4.8 Comparison of the overturning moment, including and excluding the vertical contribution of the pressure	39
4.9 Reference gravity-based foundation, including a cylinder above the still waterline, mod- elled in OrcaFlex	40
4.10 Comparison between overturning moment and wave particle acceleration for wave 4 . .	42
4.11 Comparison between overturning moment and wave-particle acceleration for wave 7 . .	42
4.12 Free surface panelled zone combined with the mesh panel model of the reference gravity- based foundation	43
4.13 Representation of the Morison elements for the reference gravity-based foundation . . .	45
5.1 Initial design configuration of the reference gravity-based foundation.	50
5.2 Reduced omnidirectional scatter diagram for a sea with a significant 50-year wave height H_{s50} of 13.0 m	51
5.3 Overview of the 1P & 3P frequency ranges, wave spectrum, wind spectrum, and regions	54
5.4 Possible failure modes for gravity-based foundations	55
5.5 Scaled eigenmodes 1-4 for the fore-aft bending moments of the initial gravity-based foun- dation design, including the tower and RNA	56
5.6 Natural frequency domain including the first natural frequency of the initial gravity-based foundation design	57
5.7 Representation of a gravity-based foundation at the foundation-soil interface under ide- alised conditions	58
5.8 Effective foundation area for a circular gravity-based foundation	59

5.9	Force diagram of a gravity-based foundation on the seabed	61
5.10	Representation of the cone slope angle for a gravity-based foundation	62
5.11	OrcaFlex model of the initial gravity-based foundation design.	63
6.1	Dependency of the bearing capacity utilization ratio on the ballast density.	65
6.2	Dependency of the sliding capacity utilization ratio on the ballast density.	66
6.3	Dependency of the first natural frequency on the ballast density.	66
6.4	Dependency of the bearing capacity utilization ratio on the footprint/base diameter.	68
6.5	Dependency of the first natural frequency on the footprint/base diameter.	68
6.6	Dependency of the bearing capacity utilization ratio on the cone height (cylinder-cone transition point).	70
6.7	Dependency of the first natural frequency on the cone height (cylinder-cone transition point).	71
6.8	Contour plot of the dependency of the bearing capacity utilization ratio on the structure shape	72
6.9	Contour plot of the dependency of the first natural frequency on the structure shape	73
6.10	Contour plot of the dependency of the cone slope angle on the shape	74
6.11	Contour plot of the dependency of the required reinforced concrete weight on the structure shape	75
6.12	Mesh panel model for the preliminary design optimized for minimal concrete material and cheapest ballast material	77
6.13	Mesh panel model for the preliminary design optimized for manufacturing	78
6.14	Mesh panel model for the balanced preliminary design	79
8.1	Automated preliminary design workflow for concrete gravity-based offshore wind foundations	83
A.1	Reference GBF design with dimensions.	88
B.1	Wave 1: Hydrodynamic loads (LPF and CFD)	90
B.2	Wave 2: Hydrodynamic loads (LPF and CFD)	90
B.3	Wave 3: Hydrodynamic loads (LPF and CFD)	90
B.4	Wave 4: Hydrodynamic loads (LPF and CFD)	90
B.5	Wave 5: Hydrodynamic loads (LPF and CFD)	90
B.6	Wave 6: Hydrodynamic loads (LPF and CFD)	91
B.7	Wave 7: Hydrodynamic loads (LPF and CFD)	91
B.8	Wave 1: Hydrodynamic loads (MP and GBF).	91
B.9	Wave 2: Hydrodynamic loads (MP and GBF).	92

B.10 Wave 3: Hydrodynamic loads (MP and GBF).	92
B.11 Wave 4: Hydrodynamic loads (MP and GBF).	92
B.12 Wave 5: Hydrodynamic loads (MP and GBF).	92
B.13 Wave 6: Hydrodynamic loads (MP and GBF).	92
B.14 Wave 7: Hydrodynamic loads (MP and GBF).	92
C.1 Reduced omnidirectional scatter diagram for a sea with a significant 50-year wave height H_{s50} of 13.0 m	96
C.2 Complete omnidirectional scatter diagram for a sea with a significant 50 year wave height H_s of 13.0 m, which was obtained from MetoceanView hindcast data [62].	97
D.1 Three-dimensional plot of the dependency of the bearing capacity utilization ratio on the structure shape	105
D.2 Three-dimensional plot of the dependency of the first natural frequency on the structure shape	105
D.3 Three-dimensional plot of the dependency of the cone slope angle on the shape	106
D.4 Three-dimensional plot of the dependency of the required reinforced concrete weight on the structure shape	106

List of Tables

3.1	Environmental conditions and parameters for the cone study.	25
3.2	Environmental conditions for all seven examined wave simulations in GBF reference study. 28	
3.3	Hydrodynamic loads calculated using Computational Fluid Dynamics, for each wave simulation	31
3.4	Mesh sensitivity study results for wave 4	32
4.1	Comparison between hydrodynamic load results using Computational Fluid Dynamics and linear potential flow (OrcaWave)	35
4.2	Comparison between hydrodynamic loads on the reference gravity-based foundation and monopile	38
4.3	Comparison between hydrodynamic loads, including and excluding loads up to the instantaneous linear free surface	41
4.4	Comparison of hydrodynamic loads from Computational Fluid Dynamics and linear potential flow (including and excluding loads above the still water line)	41
4.5	Comparison between hydrodynamic loads using Computational Fluid Dynamics, linear potential flow and nonlinear second-order potential flow	44
4.6	Dimensions and colors of each Morison element	45
4.7	Comparison between hydrodynamic loads until the still waterline, including and excluding drag load contribution	46
4.8	Comparison between hydrodynamic loads until the free surface, including and excluding drag load contribution	46
5.1	Hydrodynamic loads comparison for minimum and maximum wave period	49
5.2	Environmental conditions for the gravity-based foundation case study.	49
5.3	Initial design parameters for the reference gravity-based foundation, based on the environmental conditions and common practice.	50
5.4	Standard values for JONSWAP spectral parameters.	52
5.5	Serviceability Limit State load results from the time-domain simulations.	52
5.6	Serviceability Limit State load results from the frequency-domain simulations	53
5.7	Design parameters for the reference wind turbine	53
5.8	Loads at interface height for the reference wind turbine	54
5.9	Extreme design load cases.	57
5.10	Results of the preliminary analysis for the initial configuration of the gravity-base foundation preliminary design	63

6.1	Design parameters for the sensitivity analyses	64
6.2	Ballast density sensitivity analysis results for the initial reference gravity-based foundation with a base diameter of 45.0 m and a cylinder-cone transition point located at -15.0 m.	65
6.3	Sensitivity analysis results for the reference gravity-based foundation with a base diameter of 35.0 m, a cylinder-cone transition point located at -5.0 m, and varying ballast density (1500/2000/2500 kg/m^3).	67
6.4	Sensitivity analysis results for the reference gravity-based foundation with a base diameter of 45.0 m, a cylinder-cone transition point located at -5.0 m, and varying ballast density (1500/2000/2500 kg/m^3).	67
6.5	Sensitivity analysis results for the reference gravity-based foundation with a base diameter of 55.0 m, a cylinder-cone transition point located at -5.0 m, and varying ballast density (1500/2000/2500 kg/m^3).	68
6.6	Sensitivity analysis results for the reference gravity-based foundation with a cylinder-cone transition point located at -5.0 m, a base diameter of 45.0 m, and varying ballast density (1500/2000/2500 kg/m^3).	69
6.7	Sensitivity analysis results for the reference gravity-based foundation with a cylinder-cone transition point located at -15.0 m, a base diameter of 45.0 m, and varying ballast density (1500/2000/2500 kg/m^3).	70
6.8	Sensitivity analysis results for the reference gravity-based foundation with a cylinder-cone transition point located at -30.0 m, a base diameter of 45.0 m, and varying ballast density (1500/2000/2500 kg/m^3).	70
6.9	Sensitivity analysis results of a preliminary design optimized for minimal concrete volume, where the base diameter is 35 m, the cylinder-cone transition point is located at -35.0 m, and the ballast density is varied (1500/2000/2500 kg/m^3).	76
6.10	Sensitivity analysis results of a preliminary design optimized for manufacturing, where the base diameter is 35 m, the cylinder-cone transition point is located at -20.0 m, and the ballast density is varied (1500/2000/2500 kg/m^3).	78
6.11	Sensitivity analysis results of a balanced preliminary design, where the base diameter is 35 m, the cylinder-cone transition point is located at -30.0 m, and the ballast density is varied (1500/2000/2500 kg/m^3).	79
A.1	Environmental conditions for the reference GBF study in [24].	88
B.1	Comparison between hydrodynamic load results of CFD and LPF (OrcaWave).	89
B.2	Comparison between hydrodynamic loads on reference GBF and monopile.	91
B.3	Values for used parameters for each executed simulation in the nonlinear potential flow study.	93
B.4	Resulting hydrodynamic loads for the CFD, LPF, and NLPF simulations for wave 1 ($H = 13.2$ m & $T = 9.0$ s).	93
B.5	Resulting hydrodynamic loads for the CFD, LPF, and NLPF simulations for wave 2 ($H = 19.7$ m & $T = 11.5$ s).	94
B.6	Resulting hydrodynamic loads for the CFD, LPF, and NLPF simulations for wave 3 ($H = 19.7$ m & $T = 14.0$ s).	94

B.7	Resulting hydrodynamic loads for the CFD, LPF, and NLPF simulations for wave 4 ($H = 4.0$ m & $T = 7.0$ s).	94
B.8	Resulting hydrodynamic loads for the CFD, LPF, and NLPF simulations for wave 5 ($H = 4.0$ m & $T = 9.0$ s).	95
B.9	Resulting hydrodynamic loads for the CFD, LPF, and NLPF simulations for wave 6 ($H = 4.0$ m & $T = 11.5$ s).	95
B.10	Resulting hydrodynamic loads for the CFD, LPF, and NLPF simulations for wave 7 ($H = 4.0$ m & $T = 14.0$ s).	95
D.1	Sensitivity analysis results for the reference GBF with a base diameter of 35.0 m, a cylinder-cone transition point located at -5.0 m, and varying ballast density (1500/2000/2500 kg/m^3).	98
D.2	Sensitivity analysis results for the reference GBF with a base diameter of 40.0 m, a cylinder-cone transition point located at -5.0 m, and varying ballast density (1500/2000/2500 kg/m^3).	98
D.3	Sensitivity analysis results for the reference GBF with a base diameter of 45.0 m, a cylinder-cone transition point located at -5.0 m, and varying ballast density (1500/2000/2500 kg/m^3).	99
D.4	Sensitivity analysis results for the reference GBF with a base diameter of 50.0 m, a cylinder-cone transition point located at -5.0 m, and varying ballast density (1500/2000/2500 kg/m^3).	99
D.5	Sensitivity analysis results for the reference GBF with a base diameter of 55.0 m, a cylinder-cone transition point located at -5.0 m, and varying ballast density (1500/2000/2500 kg/m^3).	99
D.6	Sensitivity analysis results for the reference GBF with a cylinder-cone transition point located at -10.0 m, a base diameter of 45.0 m, and varying ballast density (1500/2000/2500 kg/m^3).	100
D.7	Sensitivity analysis results for the reference GBF with a cylinder-cone transition point located at -15.0 m, a base diameter of 45.0 m, and varying ballast density (1500/2000/2500 kg/m^3).	100
D.8	Sensitivity analysis results for the reference GBF with a cylinder-cone transition point located at -20.0 m, a base diameter of 45.0 m, and varying ballast density (1500/2000/2500 kg/m^3).	100
D.9	Sensitivity analysis results for the reference GBF with a cylinder-cone transition point located at -25.0 m, a base diameter of 45.0 m, and varying ballast density (1500/2000/2500 kg/m^3).	101
D.10	Sensitivity analysis results for the reference GBF with a cylinder-cone transition point located at -30.0 m, a base diameter of 45.0 m, and varying ballast density (1500/2000/2500 kg/m^3).	101
D.11	Sensitivity analysis results for the reference GBF with a cylinder-cone transition point located at -10.0 m, a base diameter of 40.0 m, and varying ballast density (1500/2000/2500 kg/m^3).	101
D.12	Sensitivity analysis results for the reference GBF with a cylinder-cone transition point located at -15.0 m, a base diameter of 40.0 m, and varying ballast density (1500/2000/2500 kg/m^3).	102

D.13 Sensitivity analysis results for the reference GBF with a cylinder-cone transition point located at -20.0 m, a base diameter of 40.0 m, and varying ballast density (1500/2000/2500 kg/m^3).	102
D.14 Sensitivity analysis results for the reference GBF with a cylinder-cone transition point located at -25.0 m, a base diameter of 40.0 m, and varying ballast density (1500/2000/2500 kg/m^3).	102
D.15 Sensitivity analysis results for the reference GBF with a cylinder-cone transition point located at -30.0 m, a base diameter of 40.0 m, and varying ballast density (1500/2000/2500 kg/m^3).	103
D.16 Sensitivity analysis results for the reference GBF with a cylinder-cone transition point located at -15.0 m, a base diameter of 35.0 m, and varying ballast density (1500/2000/2500 kg/m^3).	103
D.17 Sensitivity analysis results for the reference GBF with a cylinder-cone transition point located at -20.0 m, a base diameter of 35.0 m, and varying ballast density (1500/2000/2500 kg/m^3).	103
D.18 Sensitivity analysis results for the reference GBF with a cylinder-cone transition point located at -25.0 m, a base diameter of 35.0 m, and varying ballast density (1500/2000/2500 kg/m^3).	104
D.19 Sensitivity analysis results for the reference GBF with a cylinder-cone transition point located at -30.0 m, a base diameter of 35.0 m, and varying ballast density (1500/2000/2500 kg/m^3).	104
D.20 Sensitivity analysis results for the reference GBF with a cylinder-cone transition point located at -35.0 m, a base diameter of 35.0 m, and varying ballast density (1500/2000/2500 kg/m^3).	104

Nomenclature

List of Abbreviations

Abbreviation	Definition
ALS	Accidental Limit State
CAPEX	Capital Expenditures
CFD	Computational Fluid Dynamics
DNV	Det Norske Veritas
FS	Free Surface
FLS	Fatigue Limit State
GBF	Gravity-Based Foundation
IEC	International Electrotechnical Commission
IRENA	International Renewable Energy Agency
ISO	International Organization for Standardization
LCOE	Levelized Cost Of Electricity
LDD	Load Duration Distribution
LPF	Linear Potential Flow
MCF	MacCamy-Fuchs
NLPF	Nonlinear Potential Flow
ROSAP	Rambøll Offshore Structural Analysis Programs
SLS	Serviceability Limit State
SWL	Still Water Line
ULS	Ultimate Limit State
VOF	Volume Of Fluid
WT	Wind Turbine

Introduction to offshore gravity-based foundation design

1.1. Outlook for offshore wind energy

As nearly 200 nations finally recognized the drastic need to cut carbon emissions to fight against climate change at the COP26 climate summit in Glasgow, the power sector was responsible for 25% of the global emissions [1]. As global energy demand is increasing, a global energy transition towards renewable energy is required, where the immense potential of offshore wind plays a key role. As shown in Figure 1.1, a significant increase in offshore wind development is expected for the incoming decades, with a goal of approximately 1000 GW global cumulative installed capacity in 2050 [2].

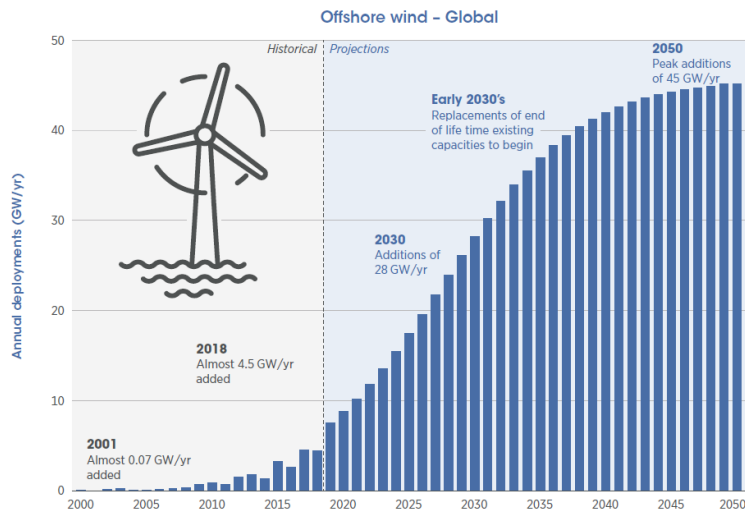


Figure 1.1: Annual offshore wind capacity additions, historical and future values [2].

To ensure that offshore wind farms can compete with traditional energy sources, the major challenge is the reduction of costs to make them more financially attractive for investments and globally accessible. However, the total installed cost and levelized cost of electricity (LCOE) have been successfully reduced in the past decade due to technological improvements and the growing maturity of the offshore wind industry. This observation is supported by data from the International Renewable Energy Agency (IRENA) [3], which has been provided in Figure 1.2. Here, it can be seen that in the past decade, the capacity factor increased while the total installed cost and LCOE declined.

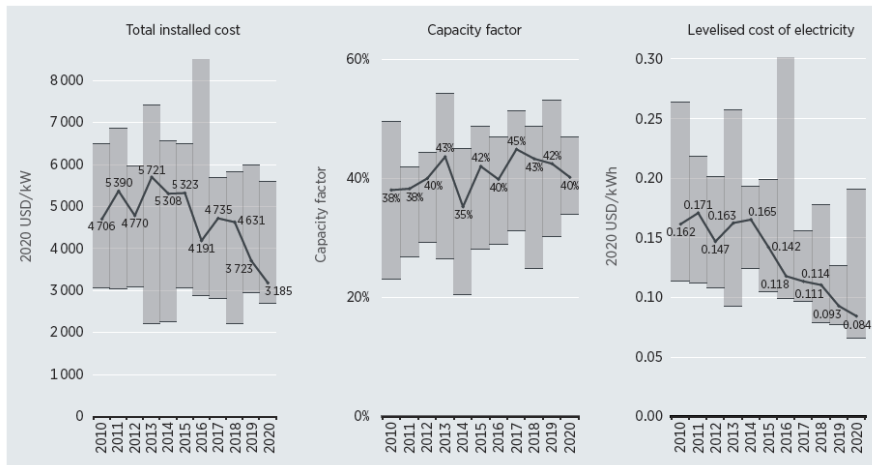


Figure 1.2: Global weighted average and range for total installed costs, capacity factors, and LCOE for offshore wind farms [3].

To stimulate the cost reduction of offshore wind energy, larger wind turbines are being produced and installed further away from the shore, from shallow water to intermediate-water depths (above 40 m). In Figure 1.3, besides the capacity, the average water depth of installed wind farms is also increasing over time, and this trend will likely continue.

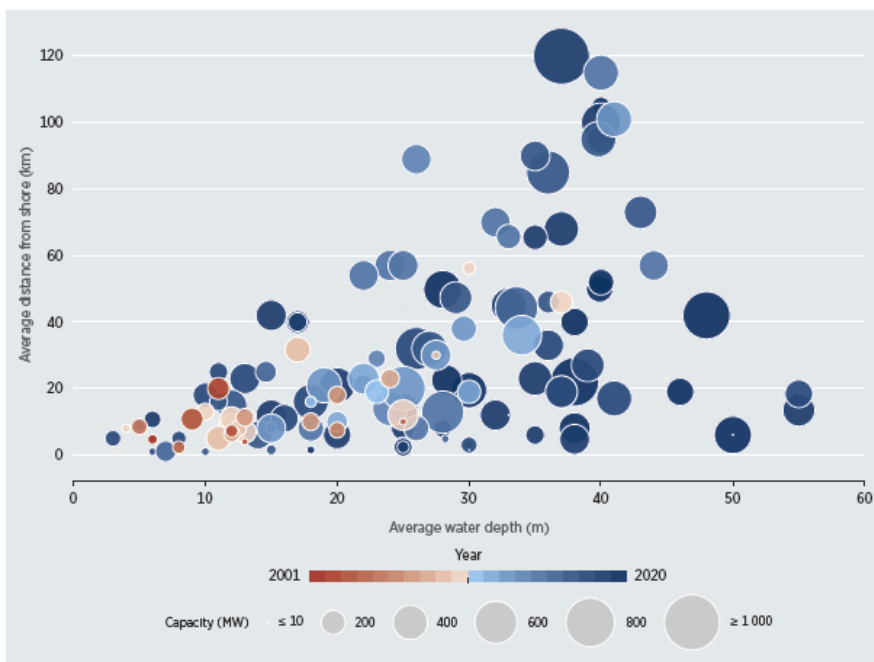


Figure 1.3: Relationship between average distance from shore and water depth for bottom-fixed offshore wind farms, 2000-2020 [3].

However, technological advancements in offshore support structures are crucial to minimizing costs to continue with this trend. Offshore support structures and foundations can account for approximately 20% of the capital expenditures (CAPEX) of a fixed-bottom offshore wind farm, which can be seen from Figure 1.4

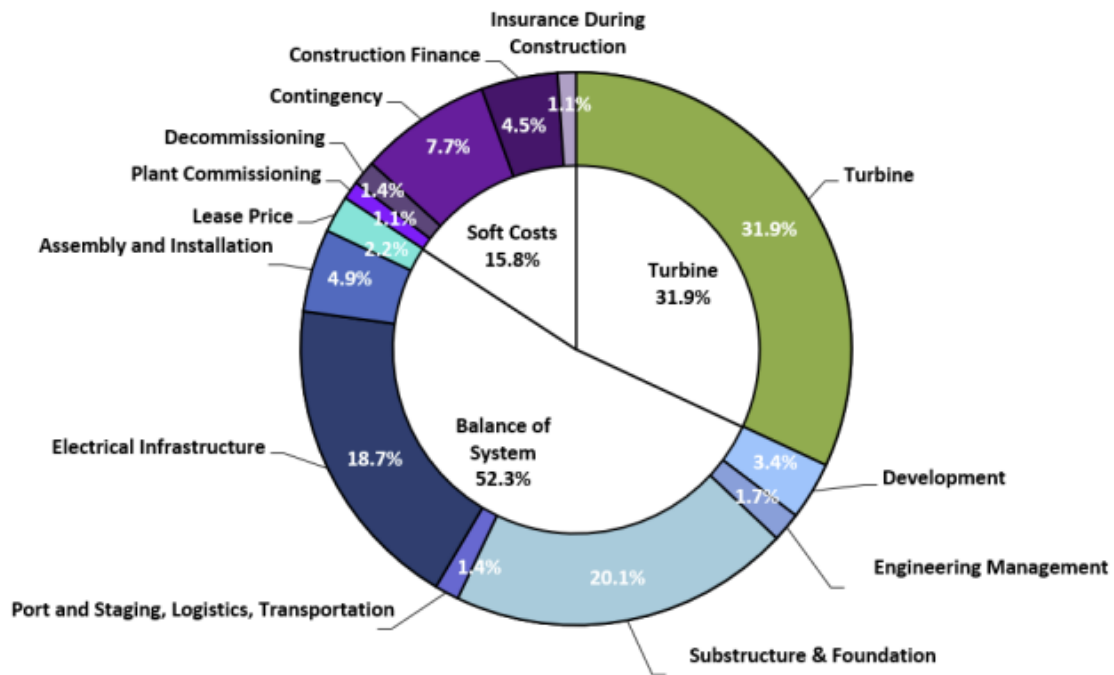


Figure 1.4: Capital expenditures for a reference fixed-bottom offshore wind farm [4].

1.2. Types of offshore support structures

First, to give an overview of existing offshore wind foundations, the main types of bottom-fixed and floating structures are provided in Figure 1.5. These bottom-fixed structures have already been widely implemented, whereas the floating concepts are still relatively new and have only been installed for a few wind farms. Their proof-of-concept still has to be demonstrated in practice before industry-wide adoption can start.

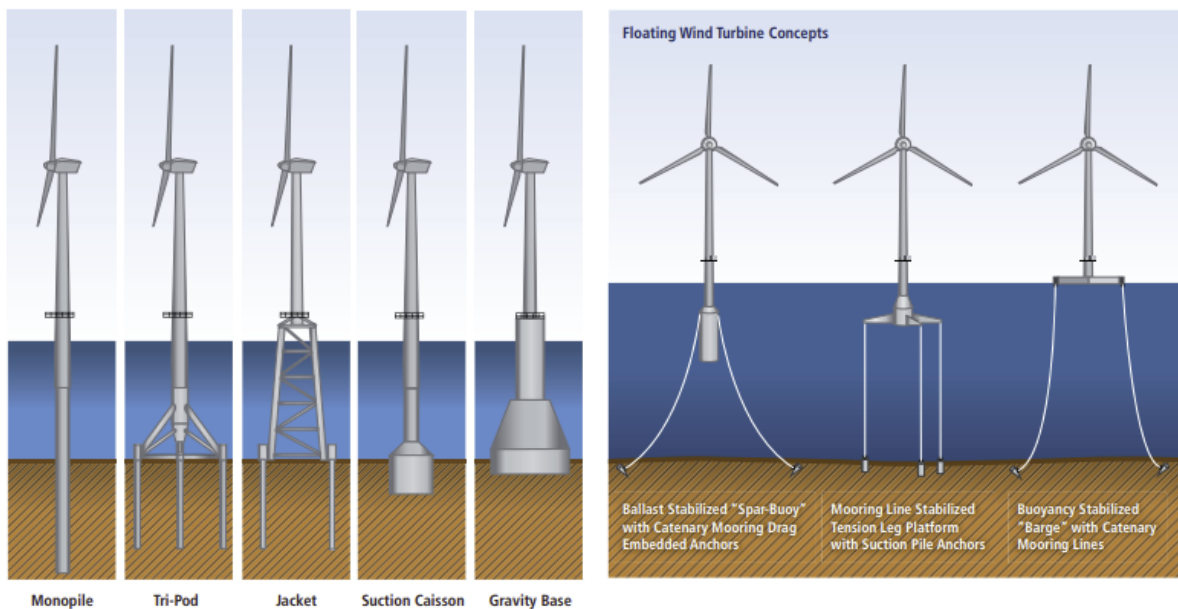


Figure 1.5: Types of common offshore wind turbine foundations, fixed and floating concepts [5].

As obtained from WindEurope [6], and shown in Figure 1.6, the currently operating offshore wind farms have predominantly been installed using monopiles with a global share of 81.2%. Monopiles are widely implemented due to the simplicity of the geometry and the broad knowledge available about this type of structure, which is highly beneficial during the manufacturing, installation, and maintenance, and also reduces the overall costs [7]. However, although XXL monopiles are being developed, they have only been deployed in shallow waters (below 40 m) [8].

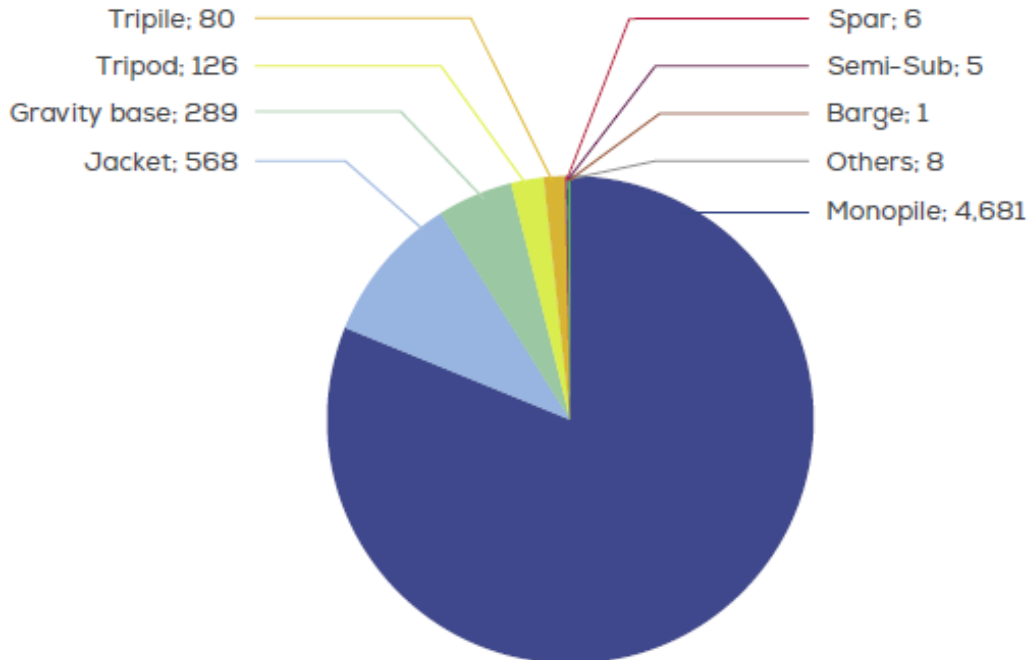


Figure 1.6: Cumulative number of installed foundations, divided per concept [6].

As the amount of offshore wind farms is quickly growing, they are being placed under various environmental conditions using wind turbine generators of different sizes. Therefore, for every offshore wind farm project, there is an optimal foundation type, which does not have to be the conventional monopile structure [9]. This report focuses solely on another viable type of support structure: Gravity-Based Foundations (GBF). Although, as seen in Figure 1.6, its contribution (5%) is relatively small, reinforced concrete GBFs can provide many advantages over other foundation types. A summary of the advantages and disadvantages of concrete GBFs is shown below:

Advantages:

- A GBF is less sensitive to the selection of a specific wind turbine.
- Concrete is relatively cheap and can be produced locally; hence its manufacturing can stimulate the local economy. Additionally, concrete is highly resistant to saltwater corrosion [10], which significantly reduces maintenance costs.
- As GBFs are installed on top of the seabed, pile driving is not required. For hard soils with high bearing capacities, pile driving for monopiles or jackets can be very difficult [7]. Furthermore, the noise emission during the installation can be harmful to marine life [11].
- Proven technology originated from oil and gas industries, as the first concrete gravity-based platform became operational in 1976 [12].
- State-of-the-art concepts are arising with semi-floating structures that can be tugged out during the transportation phase due to self-buoyancy [7]. This dramatically reduces transportation and installation costs because this diminishes the need for vessels with extreme heavy lifting capabilities. During the installation, these hollow GBFs are filled with ballast to secure them to the seabed.

Disadvantages:

- Detailed soil investigation and seabed preparation (e.g. removing the soft top layer and creating a new hard ground using dredging) is required to allow the installation of the GBF on a flat underground [7]. This process is extremely time- and labour-intensive, thus contributing significantly to the installation costs.
- To guarantee the stability and minimal fatigue of GBFs, local seabed deepening, i.e. scour, needs to be prevented by implementing expensive scour protection strategies [13].
- Storage, transport, and installation of GBFs are difficult because they take up much space and require hard ground (high bearing capacity) and heavy lift vessels with immense lifting capacities.
- The production of concrete is a very energy-intensive process and is, therefore, a major contributor to greenhouse gasses [14].

1.3. Design of Gravity-Based Foundations

In this master thesis, only the so-called "third-generation" GBF concept is used [7]. This type of reinforced concrete structure consists of a base slab, a conical shape, and a slender cylinder. Since it is mainly hollow inside, it can be designed to be semi-floating during transport and installation. Heavy lift vessels are used for transportation and installation. Thus the GBF needs to be lifted using lifting lugs (attachment point for the crane). After installation, the structure is filled with heavy ballast to secure it to the seabed with its weight. An example of this type of GBF during the construction at the Thornton Bank offshore wind farm is shown in Figure 1.7.



Figure 1.7: Gravity-based foundation under construction at Thornton bank offshore wind farm [7].

A general design framework is required to establish a design for any offshore wind support structure. In order to achieve an optimal design, an integrated design between all the complex disciplines within offshore wind farm design should be utilized. This sounds very promising, in theory. However, it is challenging to accomplish in practice. Therefore, this section will treat a simplified, integrated design approach, where several aspects are still considered independently. A design framework for the preliminary design of a concrete GBF for offshore wind is provided in Figure 1.8.

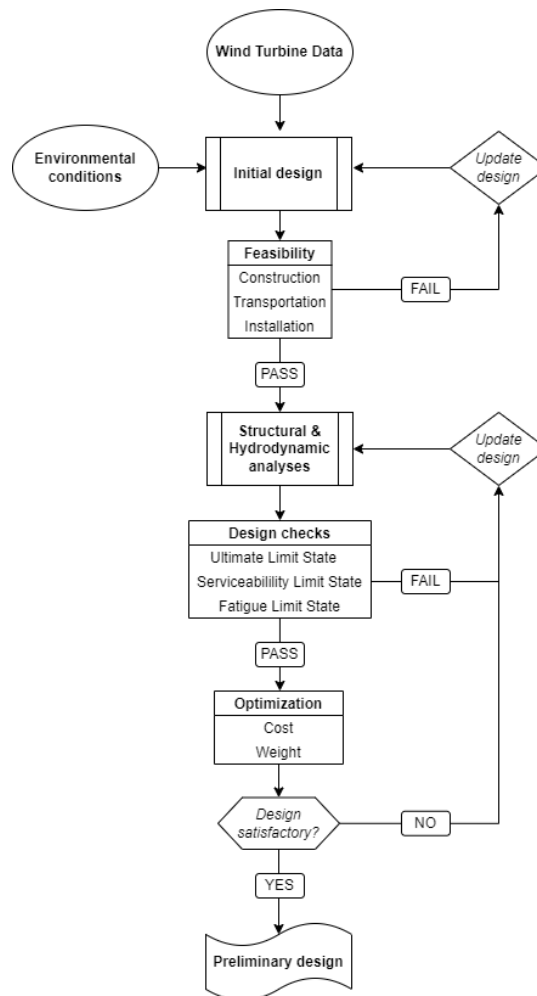


Figure 1.8: Preliminary design workflow for concrete gravity-based offshore wind foundations.

Here, it can be seen that an initial design is created based on given environmental conditions and wind turbine data. This initial design has to be feasible in terms of construction, transportation, and installation. Subsequently, an initial model is created, and structural and hydrodynamic analyses are executed. The results are verified using criteria from industry design codes (e.g. DNV/IEC) to ensure structural integrity. Finally, the design needs to be optimized based on various objectives (weight, costs, and manufacturability). If these design criteria are unmet or the model is not satisfactorily optimized, the design and models must be updated in an iterative process until the results are sufficient. In such an event, the design process has been completed, and a preliminary design has successfully been created.

First, the project needs to be described to determine the scope of the design. This is based on the design requirements, available data, and, most importantly, the environmental conditions. The environmental conditions are highly dependent on the geographical location of the project and, based on Van der Male [15] are described as:

- Wind (mean speed, turbulence, and direction)
- Wave (wave height, period, and direction)
- Current (wind-generated, tidal, and direction)
- Water depth (seabed variations, scour, and mean sea level)
- Soil (bearing capacity, cohesion, weight, and density)
- Marine growth (thickness)
- Ice (thickness, velocity, strength, direction, and frequency)
- Earthquakes (magnitude and frequency)

Besides obtaining all the environmental data and design parameters, an initial design of the structure needs to be created using estimated dimensions. Then, by combining all this data with hydrodynamic load and structural models, the design can be validated based on the design requirements.

The design requirements are fulfilled when a structure can withstand all loads described by the Ultimate State (ULS), Serviceability Limit State (SLS), and Fatigue Limit State (FLS). These checks are essential for structural integrity and are described in industry standards. Furthermore, as GBFs are quite rigid, the wave loads can be examined independently from the structural dynamics [16]. However, to avoid resonance, a simple natural frequency analysis also needs to be performed. Furthermore, soil stability needs to be ensured since these structures require a ground with high bearing capacities. Finally, if any design requirement is unmet, the structure has to be redesigned in an iterative process.

To create an optimal design, the design process requires objective functions to optimize. For offshore wind support structures, a few essential objectives could be weight, cost, and manufacturability. A final (preliminary) design is found when the initial design is satisfactorily optimized based on these objectives.

GBFs are primarily located in shallow to intermediate-depth waters. Hence they will likely be exposed to steep (nonlinear) extreme waves. Due to the complex and relatively large geometry of GBFs compared to monopiles, the determination of hydrodynamic loads is more complicated. Additionally, the structure will likely be affected due to diffraction and wave slamming. If these diffraction effects are not considered, it will likely result in overly conservative solutions. Another important aspect is that, as mentioned by Henderson and Zaaier [16], besides being lifted or tipped over, GBFs were found to be most vulnerable to sliding. Nevertheless, it must be noted that failure can also occur through a combination of different loads.

Lastly, as mentioned before, the design checks are based on guidelines from industry standards, with the following specifically being essential for the design of concrete GBFs for offshore wind:

- IEC 61400-3: Wind energy generation systems - Part 3-1: Design requirements for fixed offshore wind turbines [17];
- ISO 19903: Petroleum and natural gas industries – Concrete Offshore structures [18];
- DNV-ST-0126: Support structures for wind turbines [19];
- DNV-ST-0437: Loads and site conditions for wind turbines [20];
- DNV-RP-C205: Environmental conditions and environmental loads [21];
- DNV-RP-C212: Offshore soil mechanics and geotechnical engineering [22].
- DNV-ST-C502: Offshore concrete structures [23]

1.4. Research motivation and objectives

GBFs are not commonly used in the offshore wind industry despite their many advantages for specific cases. A better understanding of this substructure is required to increase the popularity of these types of foundations, and a straightforward preliminary design methodology should be established. As the most considerable uncertainties for GBF designs are based on the correct estimation of hydrodynamic loads, a large portion of this thesis will initially focus on establishing a valid hydrodynamic load model. This model will be based on a linear potential flow solution, which will be validated using Computational Fluid Dynamics (CFD). Furthermore, from practical experience, it is known that the resulting base shear and overturning moment on the GBF (SLS and ULS) are particularly highly interesting. Therefore, in combination with a structural model and provided input data (water level, wind, waves, current, turbine, and soil), a global GBF model can be created. Furthermore, by documenting all the executed steps, a preliminary design framework can be established and ultimately optimized.

Objectives

1. Literature review of hydrodynamics and gravity-based foundations.
2. Create a parametric design tool for GBF mesh panel models.
3. Establish a valid hydrodynamic load model based on linear potential flow.
4. Investigate essential hydrodynamic effects (drag load contribution, loads above still waterline, and wave nonlinearities).
5. Create a general structural model and perform a natural frequency analysis.
6. Perform design checks using relevant industry standards.
7. Identify the main factors that influence or limit a GBF design by executing sensitivity analyses.
8. Find an optimal GBF design for a given case study.
9. Establish a framework for the preliminary design of concrete GBFs for offshore wind.
10. Discover methods to enhance the preliminary design framework for future work.

Lastly, before this MSc. thesis started, a specialization project was executed as an initial theoretical foundation for this thesis: 'Comparison of Hydrodynamic Models for Gravity-Based Offshore Wind Foundations'. This literature research [24] was an in-depth comparison of various linear and nonlinear wave theories and hydrodynamic load models for GBFs. The objective was to analyze the differences between the results of commonly used hydrodynamic models. There is a knowledge gap concerning combining nonlinear wave kinematics with wave load models that include diffraction effects. It commenced in November 2021 and was finalized in January 2022.

1.5. Structure of report

This report initially started with an introduction (chapter 1) to the future of offshore wind energy, the basic support structures, and, more specifically, the design process for GBFs. Subsequently, the research motivation and objectives of this master thesis report were specified.

In chapter 2, a summary of the relevant theories regarding hydrodynamic load models is given, based on the work from the literature research [24].

In chapter 3, additional research regarding hydrodynamic load models is executed. An appropriate hydrodynamic load model for GBFs is described using a reference GBF study.

In chapter 4, the hydrodynamic load model for GBFs is validated using CFD data. Additionally, various comparison studies are carried out, and several potential hydrodynamic effects are investigated before the final hydrodynamic load model is composed.

In chapter 5, a design basis is established. Then, by introducing another reference study, an initial design is created based on the environmental data, design parameters, and wind turbine data. After that, a hydrodynamic load and structural model are made in Orcawave and Rambøll Offshore Structural Analysis Programs (ROSAP). Finally, through an iterative process using these models, the initial design is validated using guidelines from industry standards.

In chapter 6, the same GBF reference study as in chapter 5 is used in a sensitivity analysis, where the results of varying three essential design parameters are analyzed. Finally, based on the results, an optimal preliminary design is created.

In chapter 7, a general design methodology is described for the preliminary design of concrete GBFs for offshore wind, based on the experiences of the previously executed design process.

Lastly, in chapter 8, the findings from this report are concluded, and recommendations for future research are given.

2

Theoretical background of wave-structure interaction

This chapter describes the theory behind hydrodynamic load models from the previously executed literature research [24]. After successfully determining the wave-particle kinematics in [24], the wave-induced loads can be calculated using various models. Any structure in the ocean is subject to wave loads; hence the accurate determination of these forces is essential for a safe design. These models are based on wave-structure interaction, and similarly to wave kinematics theories, each has its domain of validity depending on the geometry and environmental conditions.

The three most popular hydrodynamic load models will be treated: Morison equation [25], MacCamy-Fuchs correction [26] and linear potential flow [27].

2.1. Hydrodynamic load models for offshore structures

2.1.1. Wave loads on slender cylinders: Morison equation

In 1950, Morison et al. [25] published an empirical method that could describe inline forces exerted by surface waves on fixed vertical cylinders. It provides a simple formula for stationary structures based on the combined inertial force dF_i and drag force dF_d , which results in the inline force on the centre of a small sectional cylinder:

$$dF_{morison} = dF_i + dF_d = \rho C_M \frac{\pi D^2}{4} a(z) dz + \rho C_D \frac{D}{2} u(z) |u(z)| dz, \quad (2.1)$$

where ρ is the water density, D is the pile diameter, C_M is the inertial coefficient, C_D is the drag coefficient, and $u(z)$ and $a(z)$ are respectively the wave-particle velocity and acceleration at height z .

The inertial force dF_i consists of the Froude-Krylov force and the added mass force. The Froude-Krylov force is generated due to the wave-particle acceleration a influencing the pressure distribution in the undisturbed wave and is obtained using $\rho \frac{\pi D^2}{4} a$. Whereas the added mass force is caused by the diffraction effects of the structure on the wave and is given as $\rho C_a \frac{\pi D^2}{4} a$, where C_a is the added mass coefficient. By combining these two terms, the formula for the inertial force is determined by Equation 2.1 using an inertial coefficient $C_M = C_a + 1$.

On the other hand, the drag force dF_d is the force experienced by the object due to the viscous fluid attempting to move through it. It is highly dependent on the size of the object and wave-particle velocity u . Furthermore, there is a 90-degree phase difference between the maximum inertial force and

maximum drag force since the acceleration a equals zero when the velocity u is maximal.

To obtain the total inline force on the structure $F_{morison}$, the sectional inline forces $dF_{morison}$ multiplied by the corresponding sectional height dz need to be summed up. Subsequently, the total overturning moment $M_{morison}$ can be calculated similarly; additionally, each section needs to be multiplied by its distance to the seabed (moment arm). In Figure 2.1, a visual representation of the inline sectional Morison forces on a slender monopile is shown.

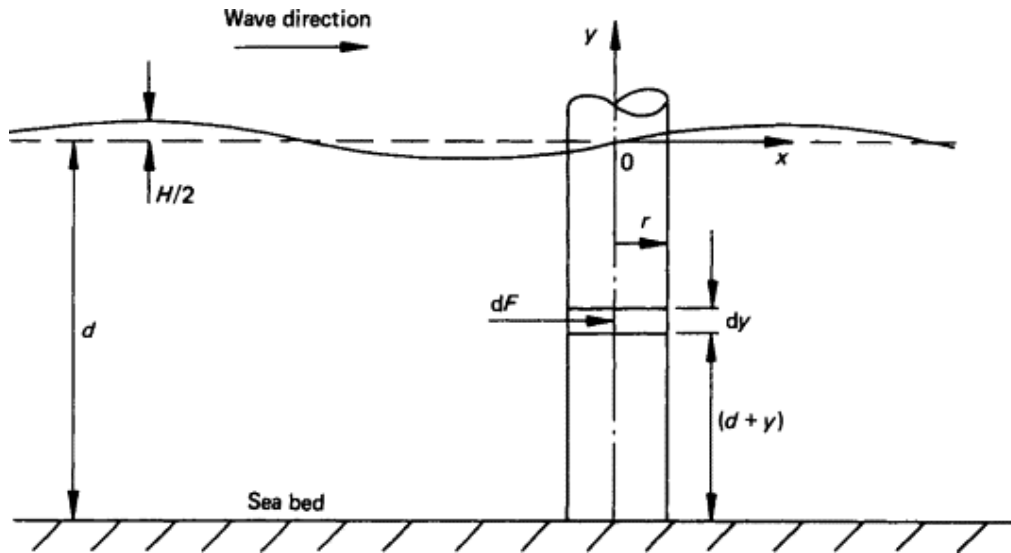


Figure 2.1: Visualization of inline Morison forces on a section of a slender vertical cylinder [28].

It must be noted that the Morison equation was developed for slender piles; therefore, according to DNV-RPC-205 [21], this method is only applicable when the wavelength is at least five times larger than the diameter: $\lambda > 5D$. If this condition is unmet, the method becomes invalid for two reasons: the flow at the centre of the structure can no longer represent the near-field flow, and the diffracted wave field becomes significant. Hence diffraction effects need to be taken into account. In short, if Morison's equation is used for relatively large bodies and the diffraction effects are neglected, it will overestimate the structure's hydrodynamic loads, producing overly conservative results.

Lastly, even though the linear sum of the inertia and drag force is incorrect from a fluid mechanics perspective, the neglect of the lift force fluctuations and interaction between neighbouring sections, the inaccurate estimation of the inline force, and many other flaws there has not been any apparent breakthrough for a superior method that is this easy to implement and does take viscous drag forces into account [29].

2.1.2. Empirical hydrodynamic coefficients

The loads calculated using Morison's equation highly depend on the hydrodynamic coefficients C_M and C_D . These coefficients are derived based on laboratory experiments or actual field measurements. A general guideline for estimating the hydrodynamic coefficients is provided in DNV-RP-C205 [21], which will be described in this section. They are highly dependent on the Keulegan-Carpenter (KC) number, a dimensionless quantity that displays the relative contribution of the drag forces compared to the inertial forces. According to Sumer and Fredsøe [30], the forces in the model are inertia dominated for small KC numbers ($KC \ll 20$) and drag dominated for large KC numbers ($KC \gg 20$). The KC number is determined using the following equation:

$$KC = \frac{U_{max}T}{D}, \quad (2.2)$$

where U_{max} is the maximum wave particle velocity estimated using linear wave theory, T is the wave period, and D is the cylinder diameter.

Furthermore, for an offshore structure, the surface roughness is highly dependent on corrosion and marine growth since they both can increase the surface roughness and thus would produce a higher drag coefficient C_D . However, the surface roughness is taken into account, and it would result in a higher drag coefficient C_D . Nonetheless, to avoid complicating the preliminary design methodology, within this master thesis, the surface of the structures is assumed to be completely smooth.

C_D is determined using Equation 2.3, where due to the assumption of a smooth surface ($\Delta < 10^{-4}$) the steady drag coefficient $C_{DS} = 0.65$. Furthermore, the wake amplification factor ψ is given by the KC -dependent Equation 2.4, where the empirical parameter $C_\pi = 1.50 - 0.024 \cdot (12/C_{DS} - 10)$.

$$C_D = C_{DS}(\Delta) \cdot \psi(K_C) \quad (2.3)$$

$$\psi(K_C) = \begin{cases} C_\pi + 0.10(K_C - 12) & 2 \leq K_C < 12 \\ C_\pi - 1.00 & 0.75 \leq K_C < 2 \\ C_\pi - 1.00 - 2.00(K_C - 0.75) & K_C \leq 0.75 \end{cases} \quad (2.4)$$

If $KC < 3$ the inertial coefficient $C_M = 2$ for both smooth and rough cylinders, otherwise C_M is obtained using Equation 2.5. This can also be visualized in a plot as shown in Figure 2.2.

$$C_M = \max \left\{ \begin{array}{l} 2.0 - 0.044(K_C - 3) \\ 1.6 - (C_{DS} - 0.65) \end{array} \right\}. \quad (2.5)$$

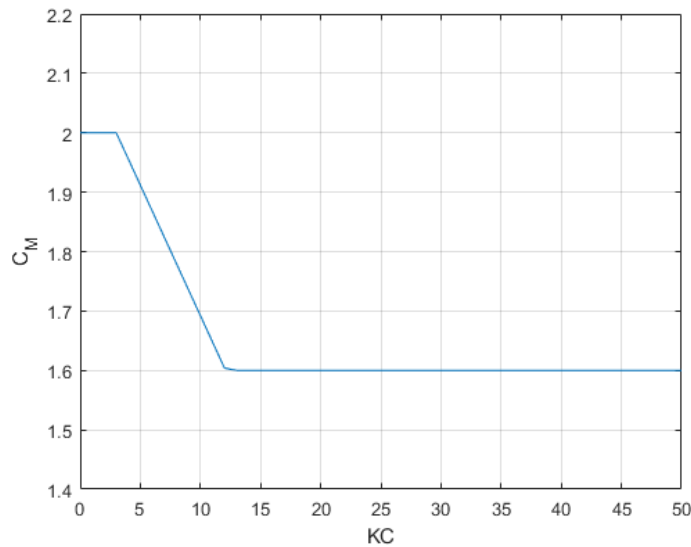


Figure 2.2: Inertial coefficient C_M as a function of KC for smooth cylinders.

Lastly, the following two observations regarding the inertia coefficient C_M can be made:

- As described in subsection 2.1.1, C_M is based on the added mass C_a . A larger diameter D will result in a larger C_a , hence a conical structure (e.g. GBFs) with an increasing D towards the seabed, will also have an increasing C_M .
- Since C_M is dependent on KC , which is determined by the diameter of the section D , it is logical that C_M is also dependent on D .

2.1.3. Wave loads on large cylinders: MacCamy-Fuchs diffraction theory

When a wave interacts with a bottom-fixed structure, it results in reflection, refraction, and diffraction. The effects due to reflection are dependent on the incoming angle of the wave. Refraction is determined by the density of the fluid, as this influences the wave speed and, therefore, the bending of the incident wave. Lastly, the waves are scattered in every direction due to the diffraction effects of the structure. Diffraction influences the pressure field around the body and the wave loads on the body.

As mentioned in the previous section, Morison's equation for slender bodies neglects diffraction effects and is, therefore invalid for large bodies. For large bodies with a relatively large diameter D compared to the wavelength λ , i.e. $\frac{D}{\lambda} > 0.2$ [21], the diffraction effects need to be taken into account. When diffraction effects increase, the problem simplifies since suddenly viscosity and flow separation can be neglected [29]. Additionally, the flow will be inertia-dominated due to the large diameter, hence the small KC number.

The diffraction effects can be considered by applying the MacCamy-Fuchs (MCF) correction [26] to Morison's equation. This simple correction presents a modified inertial coefficient $C_{M,MCF}$ and introduces a phase lag to α the inertial force, which both depend on the wave number k and the radius of the structure R . As k is dependent on the frequency, known from the linear dispersion relation, it essentially means that MCF utilizes a frequency-dependent inertial coefficient.

As described by Dean [31], ϕ_{MCF} is described using Equation 2.6, where J_1 and Y_1 are the Bessel's functions of the first and second kind. For more information about Bessel's functions, the reader is kindly referred to Watson [32]. With the use of α and the function G (Equation 2.7), the inline inertial force $dF_{i,MCF}$ acting on a section of the cylindrical structure is calculated with Equation 2.8.

$$\alpha = \arctan \frac{J_1'(kR)}{Y_1'(kR)} \quad (2.6)$$

$$G(kR) = [J_1^2(kR) + Y_1^2(kR)]^{-1/2} \quad (2.7)$$

$$dF_{i,MCF} = \frac{2\rho gH}{k} \frac{\cosh k(d+z)}{\cosh kd} G(kR) \cos(\omega t - \alpha) \quad (2.8)$$

By comparing the MCF-corrected inertial force formula Equation 2.8 with the inertial force formula from the Morison equation (Equation 2.1), a modified inertial coefficient $C_{M,MCF}$ as a function of the diameter D and the wave length λ can be established:

$$C_{M,MCF} = \frac{4G(kR)}{\pi^3(D/\lambda)^2}. \quad (2.9)$$

Hence, by using $C_{M,MCF}$, the sectional inertial force $dF_{i,MCF}$ formula from Equation 2.8 can be simplified into:

$$dF_{i,MCF} = C_{M,MCF} \rho \frac{\pi D^2}{4} a(z) \cos(\alpha) dz. \quad (2.10)$$

The sectional inline drag force dF_d remains unchanged as in the original Morison equation Equation 2.1, hence the sectional inline force including the MCF-correction is obtained using the following equation:

$$dF_{MCF} = dF_{i,MCF} + dF_d = C_{M,MCF} \rho \frac{\pi D^2}{4} a(z) \cos(\alpha) dz + \rho C_D \frac{D}{2} u(z) |u(z)| dz, \quad (2.11)$$

where ρ is the water density, g is the gravitational acceleration, H is the maximum wave height, k is the wavenumber, z is the vertical coordinate, d is the water depth, ω is the rotational wave speed, and d_z is the structure section's height.

By using Equation 2.11, the total inline force and the total overturning moment over the complete structure are calculated in the same manner as in subsection 2.1.1. The ratio $\frac{D}{\lambda}$ displays the influence of diffraction effects, hence a visual representation of $C_{M,MCF}$ as a function over this ratio is shown in Figure 2.3.

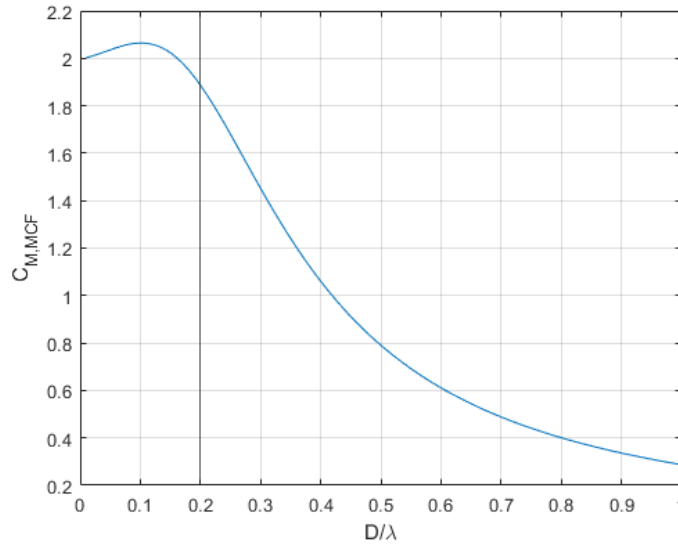


Figure 2.3: MacCamy-Fuchs-corrected inertial coefficient $C_{M,MCF}$ as a function of the diameter-wavelength ratio $\frac{D}{\lambda}$.

It can be observed that after a slight initial increase, the correction causes $C_{M,MCF}$ to decrease rapidly when the size of the structure increases. Nonetheless, it can be seen that for relatively small structures with $\frac{D}{\lambda} < 0.2$ (left of the vertical line), the inertial coefficient $C_{M,MCF}$ remains near the commonly used value of 2.

As seen from Equation 2.2 a low KC number generally occurs for relatively large structures, and therefore according to Figure 2.2 will have a high C_M of approximately 2. However, this neglects the diffraction effects of large structures that are supposed to decrease the inertial coefficient. Contrarily, they are considered in the MCF-modified inertial coefficient shown in Equation 2.9; hence this theory is more often used for large structures.

Lastly, it must be kept in mind that the MCF correction is an empirical method based on linear wave kinematics and cylindrical structures. Therefore, adding KC -dependent hydrodynamic coefficients still does not guarantee a correct physical solution.

2.1.4. Wave loads on large bodies: linear potential flow

Using the diffraction analysis program, OrcaWave [33], a linear potential flow (LPF) solution can be numerically obtained for a rigid body of any shape with relatively low computational costs. OrcaWave is an essential tool widely used to model wave effects on large offshore structures. Besides that, it solves the radiation and diffraction problem; another added benefit is that, in contrast to Morison's equation and MacCamy-Fuchs, potential flow considers not only horizontal pressure fields but also three-dimensional pressure fields. In other words, this will give a better approximation of the flow around the caisson. Additionally, it includes the effects of the interaction between neighbouring sections of the structure. This section summarises this method; hence, for a full description, the reader is kindly referred to the Orcina manual [33].

In essence, potential flow theory is based on the Bernoulli equation (Equation 2.12), which is essentially a simplified version of the Navier-Stokes equations. These simplifications are the assumptions of an inviscid and incompressible fluid combined with an irrotational flow. For more in-depth information regarding these equations, the reader is kindly referred to Kristiansen [34].

$$p = -\rho \frac{\partial \varphi}{\partial t} - \frac{\rho}{2} \nabla \varphi \cdot \nabla \varphi - \rho g z + C(t) \quad (2.12)$$

In Equation 2.12, the first term is the dynamic pressure, the second term is the quadratic pressure, the third term is the hydrostatic pressure, and the fourth term is constant, which is often equal to the atmospheric pressure.

Furthermore, it can be seen that if the velocity potential is known, the pressure can be calculated. By introducing the velocity potential, which simplifies the problem by neglecting vortices. In the LPF solution, the velocity potential ϕ can be decomposed as:

$$\phi = \phi_D + \phi_R = \phi_I + \phi_S + \phi_R, \quad (2.13)$$

where the potential of the diffracted wave ϕ_D consists of the incident wave potential ϕ_I and the scattered wave potential ϕ_S , additionally, the disturbance caused by the motion of the structure is described by the potential of the radiated wave ϕ_R , which is equal to zero for a fixed structure.

Secondly, to utilize this method, the surface of the offshore support structure is modelled by a substantial number of small quadrilateral panels. To obtain accurate results, the number of panels needs to be sufficient; however, this also increases the computational time. This can be optimized by performing convergence tests, where the size of the panels is decreased by a factor of two until the model keeps producing the same results, i.e. convergence.

After that, the velocity potential is solved for every panel using the Boundary Integral Equation Method, also widely known as the panel method. The panel method is essentially based on Green's theorem, which results in the three-dimensional flow problem being converted to a two-dimensional body surface source distribution problem [35]. Then, on each panel, the unknown source strengths are homogeneously distributed over the surface and solved using the normal velocity boundary condition [36]. Finally, each panel's linearised pressure force can be calculated after solving the potential problem using Bernoulli's equation as shown in [24].

It must be mentioned that generally, the LPF solution only considers linear waves as input and only calculates the loads up until still waterline (SWL). This simplifies the interaction between the waves and the structure since the loads are assumed to be linearly dependent on the wave amplitude. It is possible to produce a (weakly) 2nd-order nonlinear potential flow solution in OrcaFlex; however, this dramatically increases the complexity of the problem. Additionally, LPF does not produce any drag loads since it is based on irrotational flow and thus neglects flow separation (d'Alembert's paradox). Vortices are created due to flow separation on a body, resulting in a pressure drop behind the body. This pressure difference causes a drag load on the front of the body.

In short, according to Kristiansen [34], LPF and CFD can produce similar load results for the main parts of the body; however, LPF is inaccurate in areas where flow separation is crucial. Contrarily, the LPF solution is significantly less complex and time-consuming than CFD and, therefore, more practical.

2.2. Computational Fluid Dynamics for offshore structures

Computational Fluid Dynamics (CFD) is a numerical modelling method that can accurately solve complex fluid mechanics problems using large amounts of computational power. It solves the nonlinear discretized differential equations for continuity, momentum, energy, and species [37]. Unlike potential flow-based methods, they consider various effects (viscosity, breaking waves, and turbulence) by solving the Navier-Stokes equations to simulate the unsteady three-dimensional flow. The Navier-Stokes

equations are the governing equations of fluid motion, which describe a continuum fluid model. According to Kristiansen [34], for most marine hydrodynamic problems, it is sufficiently accurate to consider water as an incompressible fluid. Therefore, the continuity formula and three-dimensional momentum equations for an incompressible flow are:

$$\begin{aligned} \frac{\partial u}{\partial x} + \frac{\partial v}{\partial y} + \frac{\partial w}{\partial z} &= 0 \\ \rho \left[\frac{\partial u}{\partial t} + \frac{\partial u}{\partial x} u + \frac{\partial u}{\partial y} v + \frac{\partial u}{\partial z} w \right] &= -\frac{\partial p}{\partial x} + \mu \left(\frac{\partial^2 u}{\partial x^2} + \frac{\partial^2 u}{\partial y^2} + \frac{\partial^2 u}{\partial z^2} \right) + \rho g_x \\ \rho \left[\frac{\partial v}{\partial t} + \frac{\partial v}{\partial x} u + \frac{\partial v}{\partial y} v + \frac{\partial v}{\partial z} w \right] &= -\frac{\partial p}{\partial y} + \mu \left(\frac{\partial^2 v}{\partial x^2} + \frac{\partial^2 v}{\partial y^2} + \frac{\partial^2 v}{\partial z^2} \right) + \rho g_y \\ \rho \left[\frac{\partial w}{\partial t} + \frac{\partial w}{\partial x} u + \frac{\partial w}{\partial y} v + \frac{\partial w}{\partial z} w \right] &= -\frac{\partial p}{\partial z} + \mu \left(\frac{\partial^2 w}{\partial x^2} + \frac{\partial^2 w}{\partial y^2} + \frac{\partial^2 w}{\partial z^2} \right) + \rho g_z \end{aligned} \quad (2.14)$$

The reason behind the high accuracy of CFD is that these equations (in combination with boundary conditions) are numerically solved for the whole fluid domain, which increases the complexity and computational time tremendously. However, despite the usefulness and high accuracy of CFD when modelling waves, there are still some inaccuracy effects within CFD, as described by Kristiansen [34]:

- Numerical diffusion errors cause propagating waves to lose wave height over distance.
- Numerical dispersion errors lead to waves propagating at slightly wrong velocities.

In the following subsections, the foundation of a few relevant concepts within hydrodynamic load modelling using CFD is briefly explained; however, for more in-depth information, the reader is kindly referred to Andersson et al. [37]. Lastly, a global overview of the process for a CFD simulation is shown in Figure 2.4.

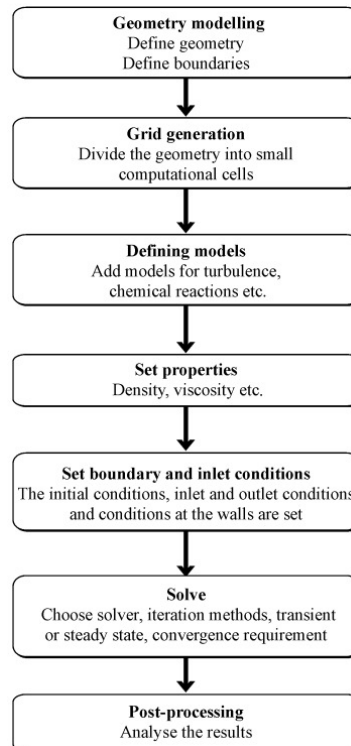


Figure 2.4: Example flowchart for a Computational Fluid Dynamics simulation [37].

2.2.1. Mesh and Domain

In CFD, the fluid volume is divided into discrete elements forming the so-called 'mesh'. There are different ways in which this mesh can be developed, and a few examples of mesh types are polyhedral, hexahedral, and tetrahedral mesh. The various mesh types have advantages and disadvantages for specific structures since they are often based on a trade-off between accuracy and computational speed. The simulation domain needs to be sufficiently large to properly visualize the waves around the structure. The size is sufficient when the waves at the domain's boundaries are unaffected by the structure. Also, the reflected waves at the boundaries must be filtered out to imitate an open sea environment.

Additionally, a crucial aspect of a proper mesh model is mesh refinement. If the whole fluid domain is modelled with high accuracy using an enormous amount of mesh elements, it will result in an unreasonably high calculation time. Hence, to get a sufficiently accurate solution within a reasonable calculation time, the mesh is only refined around critical regions (e.g. boundary layers around structure or free surface of waves) using mesh refinement zones. Here, the challenge is to correctly model smooth intersections between various zones using the available refinement tools without damping the waves.

2.2.2. Turbulence models

Within a fluid, the Reynolds number Re describes the ratio between inertial forces and viscous forces and is determined using:

$$Re = \frac{uL}{\nu}, \tag{2.15}$$

where u is the fluid velocity, L is the characteristic length, and ν is the kinematic fluid viscosity.

A low Re is generally associated with laminar flows, which are more like smooth uniform motions where viscous forces dominate. Contrarily, a high Re is linked with turbulent flows, described by unstable motions with eddies and vortexes, where inertial forces dominate.

As mentioned by Ong [38], offshore structures are generally exposed to turbulent flows with large Reynolds numbers ($Re > 10^6$). Therefore, turbulence models should be implemented to determine the hydrodynamic loads for offshore structures using CFD. A general turbulence model does not exist; however, various turbulence models are available with each applicability. A schematic overview of various commonly used turbulence models is given in Figure 2.5.

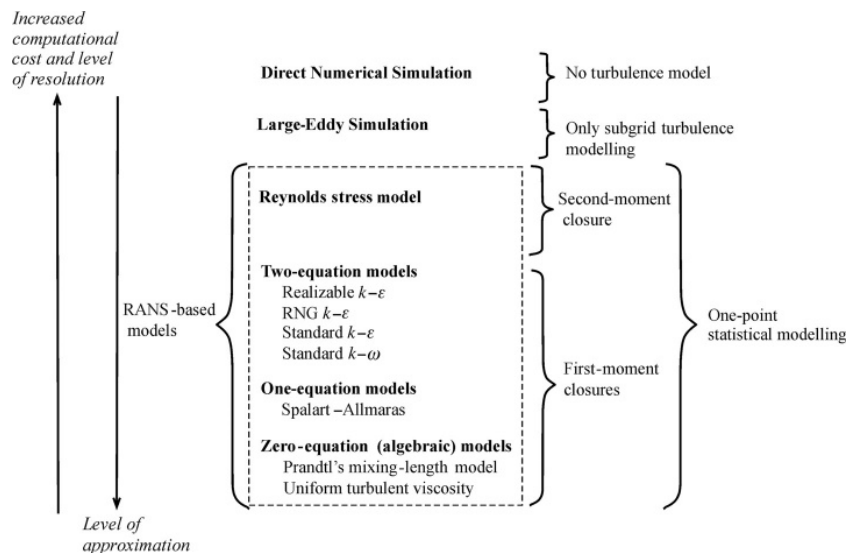


Figure 2.5: Overview of various turbulence models [37].

Turbulent flows can be described by the Direct Numerical Simulation of Navier-Stokes equations; however, in practice impossible due to the highly refined time and space resolutions required. The turbulent flows are described by fluctuating velocity fields with considerable variance in frequency, hence containing an immense amount of information that needs to be processed using computational power.

Therefore, a more cost-efficient alternative is to limit the solution to large-scale turbulence, which is called large-eddy simulation [39]. This method replaces the small-scale turbulence with flow-dependent effective viscosity and is commonly used for flows with high Re ; however, it is still very computationally expensive.

Currently, most complex flows are simulated using Reynolds-averaged Navier-Stokes (RANS) models. There are numerous RANS models available with each their advantages and disadvantages; however, the most versatile RANS model is the $k - \omega$ SST turbulence model [40], which is a combination of the standard $k - \epsilon$ and $k - \omega$. The full details of a few examples of these models are described by Alfonsi [41]. RANS models produce good results for velocity averages by producing a steady-state solution from the Navier-Stokes equations while time-averaging the turbulent flow variations. Due to the averaging nature of this method, the concept of Reynolds stresses arises. The Reynolds stresses describe the turbulent fluctuations in the flow, and precisely these terms are modelled. Lastly, additional adjustments must be made to the RANS model to incorporate specific phenomena.

2.2.3. Boundary layers

The flow of a fluid over a wall (i.e. the surface of the structure) leads to a velocity profile, which describes the velocity of the fluid from zero at the wall (no-slip condition) to the maximum mainstream value at the top of the boundary layer. Depending on the Re , a boundary layer can be laminar, transient, or turbulent. A low Re results in laminar boundary layers and a high Re in turbulent boundary layers. Additionally, the boundary layer thickness depends on the flow type (laminar/turbulent) and Re . The boundary layer should be appropriately modelled as the viscous forces on offshore structures are determined within these boundary layers.

An essential parameter for modelling boundary layers is the dimensionless wall distance y^+ . For laminar flows, turbulence models can integrate turbulence to the wall. Although this requires considerable computational power, it helps calculate viscous loads. Meanwhile, for turbulent flows, wall functions can be utilized. Different values for y^+ correspond to different layers and wall regions:

- For $y^+ < 5$, the fluid is dictated by viscous effects in the viscous sub-layer.
- For $5 < y^+ < 30$, a transition between the viscous and turbulent layers occurs in the so-called buffer layer.
- For $y^+ > 30$, the turbulent dominance occurs.

Lastly, the velocity development of the boundary layer on a flat plate is shown in Figure 2.6, where u_∞ is the free stream speed. For more information about boundary layer theory, please refer to Schlichting and Gersten [42].

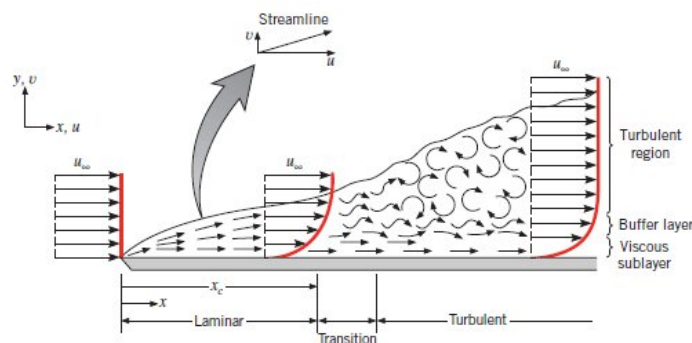


Figure 2.6: Boundary layer velocity development on a flat plate [43]. The fluid moves in the positive x and y directions and the layer becomes thicker over the distance, where it starts as laminar but becomes turbulent.

2.2.4. Multi-phase flow modeling

A multi-phase flow combines multiple phases (solid, fluid, or gas) within one flow. In the sea, there is multi-phase flow since every wave has a free surface. Additionally, in breaking waves, there are gas bubbles within the water or sediment transportation; hence, for offshore structures, multi-phase flow modelling is indeed of high importance. According to Andersson et al. [37], the most common multi-phase flow models are classified as:

- Euler–Lagrange
- Euler–Euler
- Mixture/Algebraic-slip
- Volume of Fluid (VOF)
- Porous-bed

These methods, except for the VOF (subsection 2.2.4), will not be described in this report. However, it must be noted that each of these models is based on different assumptions and have its drawbacks. Lastly, the European Research Community on Flow Turbulence and Combustion [44] gives recommended guidelines for dispersed multi-phase flows.

Volume of Fluid

In the field of CFD, many multi-phase flow models that can simulate free surface elevations have been established. This is crucial for determining the location of the free wave surface since that is where the highest loads and most uncertainties occur.

A well-known simple yet highly efficient method is the Volume of Fluid (VOF), established by Hirt and Nichols in 1979 [45]. This two-phase flow solution describes a numerical field where each mesh cell has a fractional volume of the fluid. Since it concerns the fractional volume, the fraction F is a value between 0 and 1, where 0 indicates that the cell is filled with air and 1 indicates that it is completely filled with water.

Furthermore, to simulate the flow, an estimation of the amount of fluid travelling between neighbouring cells is derived for each time step to track its location. Subsequently, the hydrodynamic loads are determined by integrating the pressure and viscous stresses along the structure's surface. An example of the VOF method applied to an ocean wave at the free surface is shown below in Figure 2.7.

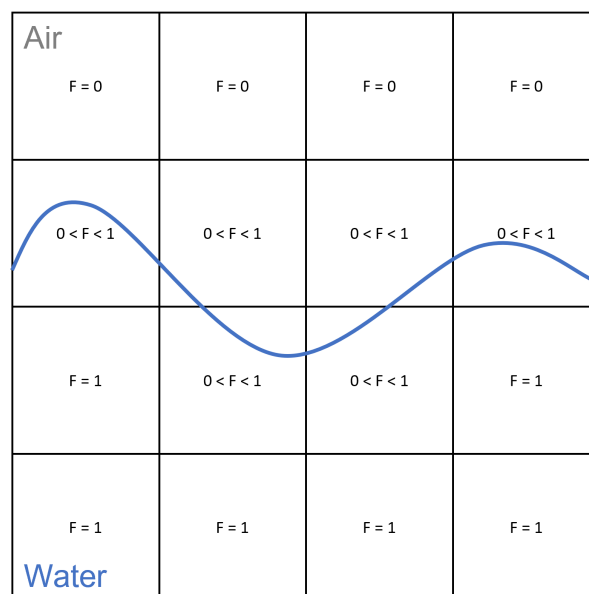


Figure 2.7: Visual representation of the volume of fluid method interface for an ocean wave.

2.2.5. Conclusion regarding Computational Fluid Dynamics

A few significant advantages of CFD are its flexible capability to easily adjust design parameters and environmental conditions, the comprehensive assessment of location- and time-dependent data, and the possibility to model a wide range of physical conditions on any geometry. Unlike other methods, CFD is not based on (semi-)empirical models but on fluid mechanics. In addition, essential phenomena (e.g. flow separation, viscous effects, turbulence, interaction effects between structure components, and wave-breaking effects [46]) can be simulated since the results are purely based on the flow field. As shown by Wu and Oakley [47], CFD models can produce reliable nonlinear wave fields that simulate wave-structure interactions correctly.

Nevertheless, to use CFD as a modelling tool for GBFs, a good understanding of fluid dynamics and the available CFD models is required. Additionally, a proper mesh refinement strategy must be set up, and the applied models must be validated. It must be emphasized that CFD is a handy tool; however, since it is not fully developed yet, it cannot replace physical model tests [34].

2.3. Additional modeling factors

In this section, various factors and phenomena are treated, which due to their complexity, have been simplified for this study. These factors must be considered for a true representation of hydrodynamics on a specific offshore structure.

2.3.1. Irregularity

The majority of the theories treated are only valid for regular waves. This literature study neglects irregular waves because it highly simplifies the problem. Additionally, regular waves can produce the conditions representing the wave kinematics with the highest loads, which is, in essence, the worst-case scenario of an irregular wave. However, waves have a high degree of randomness in a natural ocean environment due to the frequent variation of wind direction and speed. Therefore, to correctly portray the actual wave kinematics, the irregularity of waves should be included.

Various linear models for irregular waves exist. However, nonlinear models for irregular waves are uncommon. The most straightforward approach for irregular linear wave models is the superposition of random regular linear waves (Figure 2.8). This is acceptable for a first approximation; however, nonlinearities will impact large waves.

In the current industry, designers often implement an extreme regular wave into an irregular wave state. This might give a likeable representation of the wave on the free surface. However, it is physically incorrect since wave kinematics have been mistreated.

Alternatively, existing nonlinear irregular wave models are either computationally expensive (e.g. advanced Boussinesq models [48]) or weakly nonlinear (e.g. second-order irregular Stokes wave model [49]). Thus, for these nonlinear irregular waves, it is common practice to apply safety factors to linear irregular wave models to compensate for the underestimation of nonlinear wave loads [50].

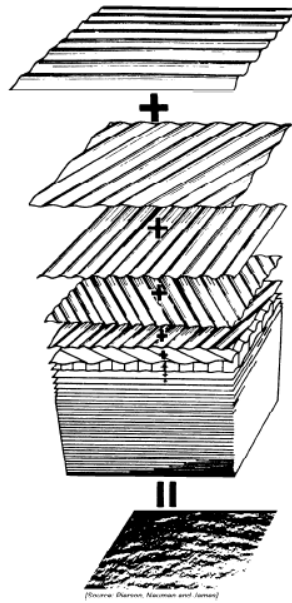


Figure 2.8: Visualization of an irregular sea consisting of a summation of regular waves [36].

2.3.2. Tidal current

Tidal currents are oscillating movements induced by the rise and fall of tides. These currents can be quite significant for the water particle velocity and thus also for the loads on the structure. According to Lewis et al. [51], by applying the 1/7th-power law to the vertical tidal current velocity profile, reasonably accurate estimations are obtained and widely used in the industry. The vertical tidal current velocity profile is determined using Equation 2.16, where u_c is the tidal current at position z , u_s is the tidal current velocity near the free surface, d is the water depth, and n is the power factor of 1/7.

$$u_c(z) = u_s \left(\frac{z}{d} \right)^n \quad (2.16)$$

To implement the tidal current into the wave kinematics, the resulting values for the tidal current velocity profile values are added to the horizontal wave-particle velocities u corresponding to each depth.

2.3.3. Breaking waves

When waves move from deep to shallower water, they lose their sinusoidal shape and start showing nonlinear characteristics. This continues while the water depth keeps decreasing until it eventually breaks. Wave breaking initiates when the water particle velocity a at the wave crest's tip exceeds the wave celerity c and is highly dependent on the wave steepness and the seabed. When waves break near the offshore structure, it can cause the structure to experience wave-slammings impacts with more significant magnitudes than inline wave loads. The duration of these breaking waves is very short; therefore, analyzing the resulting slamming loads is challenging. As GBFs are primarily located in shallow and intermediate-depth waters and have large diameters, wave slamming can have a critical impact on the structural stability of the structure [52].

On the other hand, as observed by Paulsen et al. [53], when wave slamming impacts do not cause the governing design loads, it can still result in more significant wave-particle accelerations near the free surface. Therefore, wave breaking and slamming should be considered if an accurate simulation is desired. It must be noted that most models consider breaking waves by incorporating empirical results or probabilistic methods, whereas CFD uses complex turbulent models [54]. Nonetheless, due to the complexity of breaking waves, it is regarded to be not within the scope of this master thesis.

2.3.4. Directionality

In this research, the waves are assumed to be unidirectional and approach the structure perpendicularly. However, natural ocean waves are omnidirectional. This simplifies the models by transforming the problem from a three-dimensional to a two-dimensional wave. As mentioned by Sarpkaya [29], the predicted forces on the structure based on a design wave are most likely more significant than the actual loads in the ocean. This is due to the mitigating effects of the chaotic nature of the environment, as disorder results in energy loss. This claim is supported by the worldwide measurements of directional wave spreading by Forristall and Ewans [55], where a lower wave spreading factor of 0.707 is used for omnidirectional waves instead of 1 for unidirectional waves. The wave spreading factor accounts for the directional spreading of waves based on empirical data, and a lower value means a higher directional wave spread. This factor must be applied to the water particle velocities and accelerations. On the contrary, despite the low probability, when considering omnidirectional exceptions may occur in the shape of extreme waves. When these extreme events occur, the directional wave-spreading factors change significantly and should not be underestimated.

2.3.5. Ocean water properties

The calculated wave-induced loads can vary slightly due to the incorrect presumption of values for ocean water properties. The most important properties are density and viscosity, which depend on the water's temperature and salinity. Furthermore, temperature and salinity are highly dependent on the geographical location of the sea because they can be influenced by ocean currents and water inflow from rivers. Lastly, the difference in density over the depth of the water can strengthen internal waves in the deeper region, which can significantly affect the structure [56].

2.4. Summary of literature study

Before this research, an in-depth comparative study of hydrodynamic models for GBFs [24] was already executed. The goal of that study was to research the differences between commonly used linear/nonlinear wave theories (Airy and stream function [57]) combined with simple wave load models (Morison [25], MacCamy-Fuchs [26], and linear potential flow [27]) when applied on in GBFs in intermediate-depth waters. Here, a summary of the conclusions found is given. In chapter 2, the theory behind standard hydrodynamic load models has already been described. For further information regarding the theories, method, and results, the reader is kindly referred to the previously performed literature study [24].

Summary

1. By including a velocity profile extension method of any type, it always increased hydrodynamic loads on the structure.
2. The importance of diffraction strongly depends on the environmental conditions and the structure's size.
3. The hydrodynamic loads on large bodies (e.g. GBFs) are greatly dominated by the inertial loads; therefore, drag is negligible.
4. If the relative contribution of the drag loads is insignificant, the tidal current loads will also be insignificant since they are both dependent on the wave-particle velocity.
5. Nonlinear waves will cause a small phase lag compared to linear waves.
6. The magnitude of the hydrodynamic loads (base shear and overturning moment) was similar for all simulations; however, the overturning moment was not calculated using the LPF solution. Therefore, this will be further investigated in subsection 3.1.1.

3

Description of hydrodynamic load model for Gravity-Based Foundations

This chapter establishes an appropriate method for determining wave loads on GBFs. First, based on previous works, additional research is performed in section 3.1. This research investigates the overturning moments using a diffraction solver (OrcaWave) and the influence of conical shapes on wave loads. Ultimately, in section 3.2, a GBF reference study is introduced as a basis of the hydrodynamic load model used in this chapter. After the hydrodynamic load model is described, it will be validated using CFD data in chapter 4.

3.1. Additional research regarding hydrodynamic load models

3.1.1. Total overturning moment based on a linear potential flow solution

As an extension to the literature study [24], the overturning moment was calculated using the LPF solution. If a horizontal beam model theory (e.g. Morison/MCF) is used, the structure is assumed to be made of vertical cylinders stacked on each other. An example of how these theories perceive the structure is shown in Figure 3.1. For each beam element, the horizontal hydrodynamic loads are independently calculated and integrated over the height to get the total loads. Contrarily, a diffraction solver will examine a structure as one model consisting of thousands of panels, where the interactions between neighbouring panels are considered. Although MCF's method works for non-slender structures and includes diffraction effects, the theory is not valid for modelling a structure with a variable diameter (e.g. GBFs).

For cylindrical structures (e.g. monopiles), the hydrodynamic loads are entirely characterized by the horizontal loads. Meanwhile, the conical shape of a GBF would also lead to a vertical contribution of the pressure. Therefore, further investigating this matter was highly interesting before concluding. Furthermore, this vertical contribution could reduce the net overturning moment due to opposing sign conventions of the resulting loads. This is visually portrayed in Figure 3.2, where the left drawing shows a GBF model using only horizontal beam elements and the right graphic shows a GBF panel model.

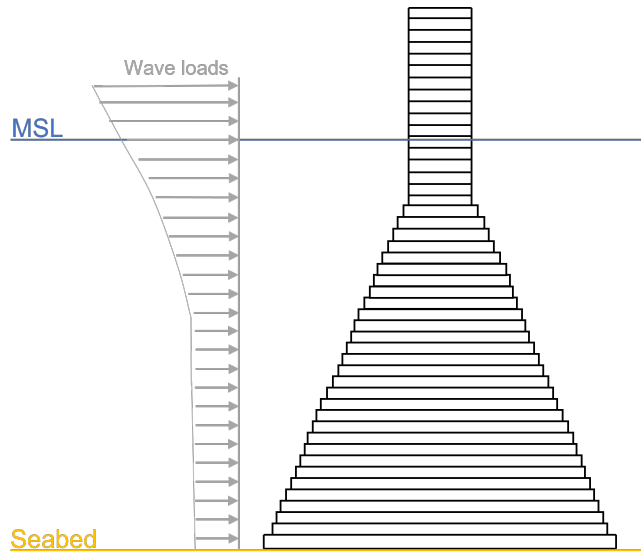


Figure 3.1: Representation of a horizontal beam model for a gravity-based foundation subjected to wave loads.

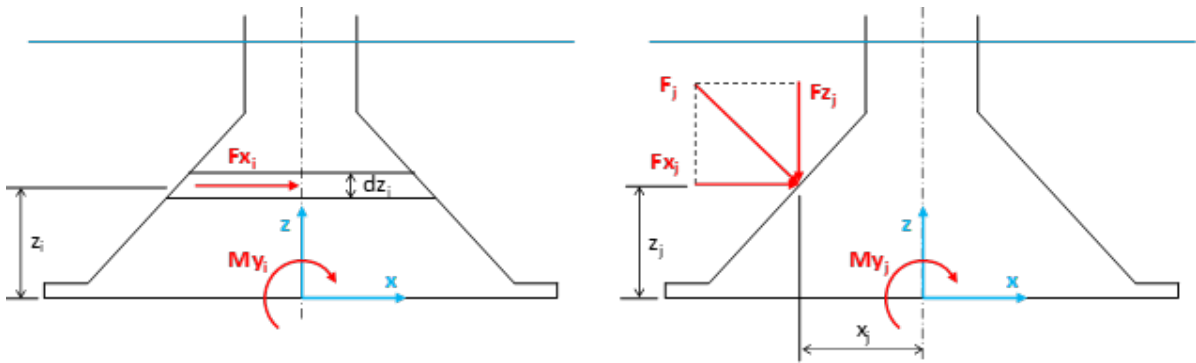


Figure 3.2: Sign convention of GBF model using horizontal beam elements on the left figure, and quadrilateral panels on the right figure (by courtesy of M. Karch). In the left figure, Fx_i is the horizontal hydrodynamic load on a section with thickness dz_i at height z_i , whereas My_i is the resulting overturning moment due to this load. In the right figure, Fx_j and Fy_j are the horizontal and vertical hydrodynamic loads on a panel j , which results in an overturning moment M_j .

As shown in subsection 2.1.1 and subsection 2.1.3, the hydrodynamic force on a beam element is calculated by integrating the sectional force Fx_i over its height dz_i . Since the vertical contribution of the pressure is neglected, the overturning moment produced by this section My_i is obtained by multiplying Fx_i with its relative distance to the seabed z_i :

$$My_i = Fx_i dz_i z_i. \quad (3.1)$$

To calculate the total overturning moment My for this beam model, the sum is taken of all the sectional overturning moments My_i .

For a panel model, where the vertical contribution of the pressure is not neglected, it can be seen that the hydrodynamic force on a specific panel F_j is normal to the surface of the cone. Hence, it can be calculated by multiplying the pressure p_j with the normal vector n_j and panel surface area A_j :

$$F_j = p_j n_j A_j. \quad (3.2)$$

To obtain the horizontal force Fx_j and the vertical force Fy_j , n_j needs to be replaced by either its scalar x-component n_x or y-component n_y . Subsequently, the overturning moment caused by this panel My_j can be determined using the moment arms z_j and x_j :

$$My_j = z_j Fx_j - x_j Fz_j \quad (3.3)$$

In order to determine the total base shear Fx or total overturning moment My using the panel model, all panel loads (Fx_j and My_j) around and along the height of the structure need to be summed up. Simplified wave models (e.g. Morison and MacCamy-Fuchs) assume that the structure is modelled as a beam model, which is acceptable for vertical cylindrical structures. However, this assumption cannot be made for GBFs as the conical section will also experience a vertical contribution of the hydrodynamic pressure. Due to the opposing sign conventions in Equation 3.3, there is a noticeable phase-shift between My_i and My_j .

To finalize the previous research [24], the total overturning moment remained to be calculated using the LPF solution. This was computed using the diffraction solver OrcaWave [33], where the overturning moment was found using a shear section located at the seabed. In Figure 3.3 the results are shown, where the following simulations were executed:

- Linear wave kinematics + Morison equation (L + M)
- Nonlinear wave kinematics + Morison equation (NL + M)
- Linear wave kinematics + MacCamy-Fuchs correction (L + MCF)
- Nonlinear wave kinematics + MacCamy-Fuchs correction (NL + MCF)
- Linear wave kinematics + Potential flow (L + PF)

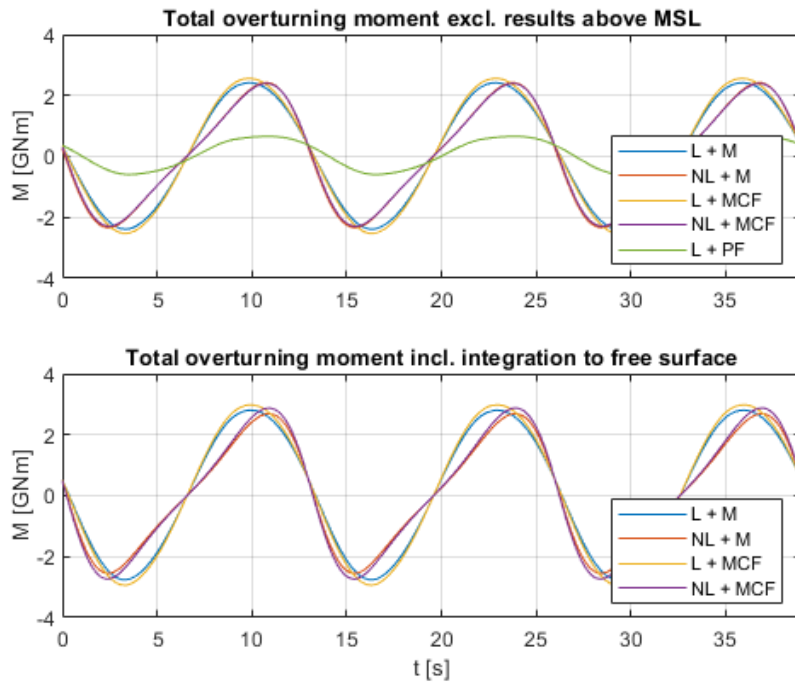


Figure 3.3: Total overturning moment M on a reference GBF [24]. The top figure represents the loads until the mean sea level, whereas the bottom figure includes the integrated loads until the instantaneous linear free surface. Each simulation is based on a combination of either linear (L) or nonlinear (NL) wave kinematics with Morison (M), MacCamy-Fuchs (MCF) or linear potential flow (PF).

The dimensions of the used reference GBF design and the environmental conditions are specified in Appendix A. In the top figure, the total overturning moment was only calculated until the SWL, whereas the bottom figure shows the total overturning moment, including integration to the free surface (extrapolation). It must be noted that the LPF solution was only used to obtain the overturning moment until the SWL, since this result sufficiently displays the effects of including the vertical contribution of the pressure. The loads until the instantaneous linear free surface will be investigated in subsection 4.4.1.

As expected, the opposing sign convention causes the vertical loads to reduce the total overturning moment. This reduction is induced by the phase difference between the loads on the front and on the rear of the structure. Since the magnitude and direction of the loads are determined by the location of the orbital wave particles near the structure, this phase difference is dependent on the ratio between the wavelength and structure's diameter. Therefore, owing to the fact that GBFs have conical sections with a large diameter relatively to the wavelength, this phase difference becomes very apparent.

Lastly, in hindsight, it can be already concluded that if Morison's or MCF's theory is used, it will likely overestimate the hydrodynamic loads compared to LPF. To validate if this LPF solution is more realistic, it needs to be compared with the results from more sophisticated models (e.g. CFD). Thus, this chapter aims to analyze the differences between LPF and CFD.

3.1.2. Influence of conical shape on wave loads

In 2018 a comparison study between LPF(WAMIT) and MCF was executed by M. Karch for a vertical cylinder and cones of varying shapes (see Figure 3.4). The vertical cylinder's diameter and the top diameter of all the cones were equal to 7 m, whereas the bottom diameter of the cones varied from 8 m to 60 m. Based on his research, the following conclusions were made:

- By adding a cone to a structure, the total hydrodynamic loads increase, and a phase lag between the base shear and the overturning moment is introduced.
- For structures that were vertical cylinders or closely identical to vertical cylinders, MCF's method produced similar results compared to LPF.
- For large conical structures, MCF's method became invalid since the results significantly deviated from the LPF solution.

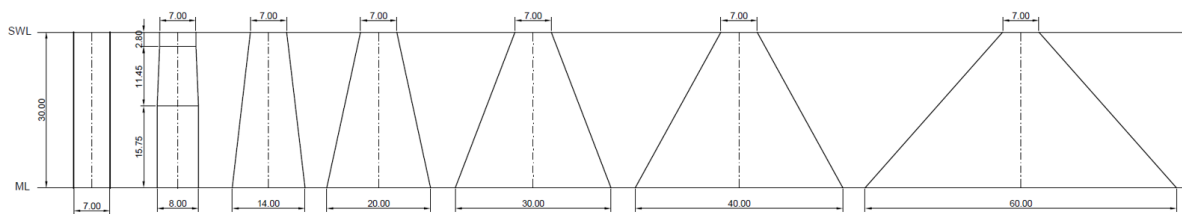


Figure 3.4: Examined structures in the cone study (by courtesy of M. Karch). All the seven configurations have the same top diameter (7.00 m) and length(30.00 m,) however the bottom diameter varies (7.00 - 60.00 m).

In this section, the cone study is slightly extended to validate the LPF results from OrcaWave and to display the influence of the conical shape on the overturning moment. As mentioned in subsection 3.1.1, the conical parts have both a horizontal and vertical pressure contribution, whereas vertical cylinders only have a horizontal pressure contribution. Therefore, the difference between Morison/MCF and LPF will likely be caused by this vertical pressure component.

Seven cylindrical/conical structures were examined using the same environmental conditions and the following conditions:

Table 3.1: Environmental conditions and parameters for the cone study.

Parameter	Value	Unit
Water depth d	30.0	m
Wave height H	2.0	m
Wave period T	1.0-20.0	s
Upper diameter D_{top}	7.0	m

The resulting overturning moment $M_{y,tot}$ (with and without the vertical contribution of the pressure) for each structure is given in Figure 3.5-3.11. It must be noted that there is no current, and the loads are

calculated only up until the SWL. Additionally, the diffraction limit $\lambda/D = 5$ is displayed as a red vertical line, which is obtained by first calculating the wavelengths for all periods using the linear wave dispersion relation (Equation 3.4) and the wavelength formula (Equation 3.5). Subsequently, the wavelength-diameter ratios λ/D_{avg} are calculated and the wave period corresponding to the diffraction limit is found. The average diameter D_{avg} is determined using $D_{avg} = (D_{top} + D_{bottom})/2$.

$$\omega^2 = gk \tanh kd \quad (3.4)$$

$$\lambda = \frac{2\pi}{k} \quad (3.5)$$

It can be seen that the cone's shape influences the vertical contribution of the pressure. If the structure retains its cylindrical shape, there is barely any effect. However, as soon as the bottom diameter becomes larger than twice the top diameter, the vertical forces become more significant at the overturning moment. This effect is even more noticeable when the diffraction limit is exceeded. With this knowledge, it can be concluded that the vertical contribution of the pressure is crucial for large conical structures. Thus for these structures, simple hydrodynamic horizontal beam models (Morison/MCF) will produce insufficiently accurate load estimations.

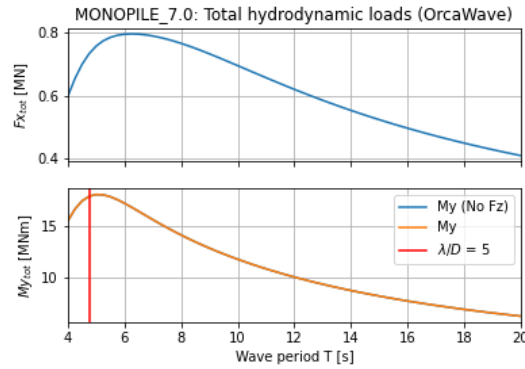


Figure 3.5: Hydrodynamic loads (base shear $F_{x_{tot}}$ and overturning moment $M_{y_{tot}}$) on a monopile with diameter $D = 7.0$ m for varying wave periods T .

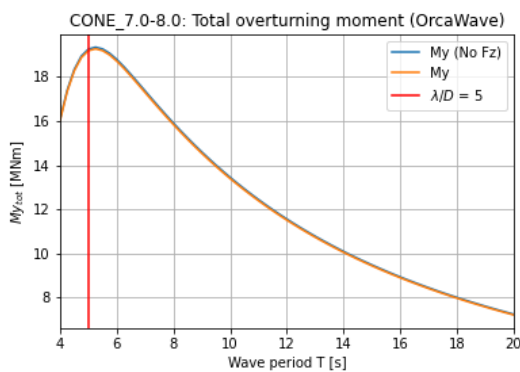


Figure 3.6: Hydrodynamic loads (base shear $F_{x_{tot}}$ and overturning moment $M_{y_{tot}}$) on a cone (top diameter $D_{top} = 7.0$ m and bottom diameter $D_{bot} = 8.0$ m) for varying wave periods T .

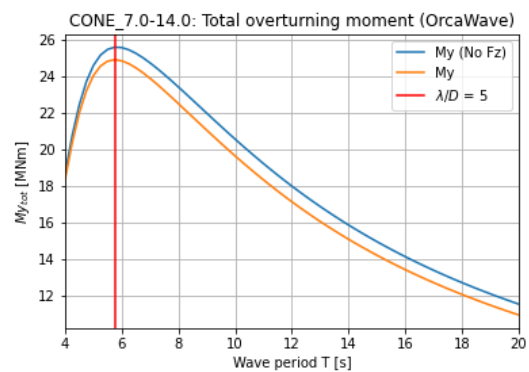


Figure 3.7: Hydrodynamic loads (base shear $F_{x_{tot}}$ and overturning moment $M_{y_{tot}}$) on a cone (top diameter $D_{top} = 7.0$ m and bottom diameter $D_{bot} = 14.0$ m) for varying wave periods T .

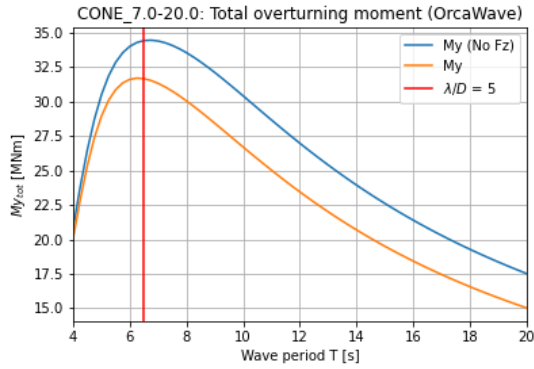


Figure 3.8: Hydrodynamic loads (base shear $F_{x_{tot}}$ and overturning moment $M_{y_{tot}}$) on a cone (top diameter $D_{top} = 7.0$ m and bottom diameter $D_{bot} = 20.0$ m) for varying wave periods T .

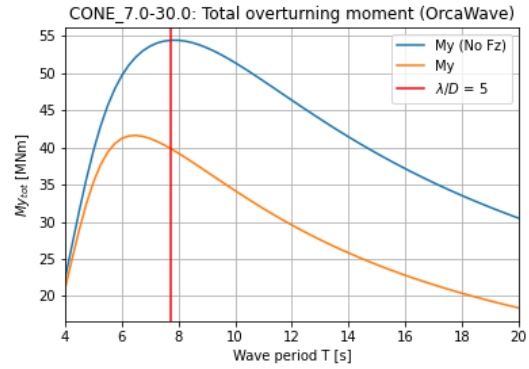


Figure 3.9: Hydrodynamic loads (base shear $F_{x_{tot}}$ and overturning moment $M_{y_{tot}}$) on a cone (top diameter $D_{top} = 7.0$ m and bottom diameter $D_{bot} = 30.0$ m) for varying wave periods T .

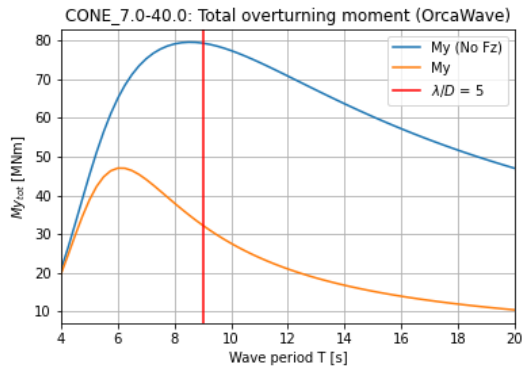


Figure 3.10: Hydrodynamic loads (base shear $F_{x_{tot}}$ and overturning moment $M_{y_{tot}}$) on a cone (top diameter $D_{top} = 7.0$ m and bottom diameter $D_{bot} = 40.0$ m) for varying wave periods T .

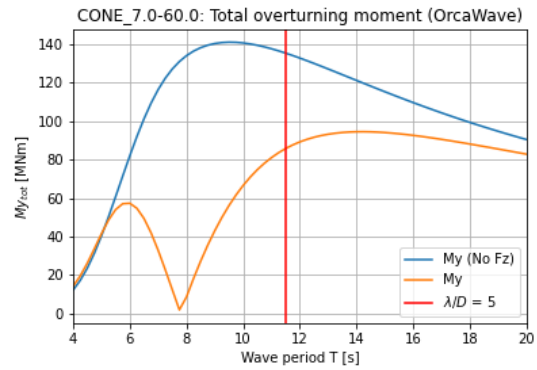


Figure 3.11: Hydrodynamic loads (base shear $F_{x_{tot}}$ and overturning moment $M_{y_{tot}}$) on a cone (top diameter $D_{top} = 7.0$ m and bottom diameter $D_{bot} = 60.0$ m) for varying wave periods T .

Lastly, in Figure 3.11 the total overturning moment on the largest cone ($D_{bot} = 60.0$ m) is shown, where a strange drop in loads can be found between $T = 6-9$ s. This can be clarified due to different contributions (e.g. horizontal and vertical components of the pressure on the conical section) cancelling each other out. By comparing these results with the second-largest cone ($D_{bot} = 40.0$ m), which is provided in Figure 3.10, it can be observed that this significant cancellation only occurs when the conical section becomes extremely large. In the case of the largest cone, the ratio between the D_{top} and D_{bot} is $1/6$, i.e. the cone's bottom is six times as large as the cone's top.

3.2. Introduction to reference study for the validation of the hydrodynamic load model

As concluded in the previous sections, simple beam model theories can fundamentally never produce accurate wave load estimations for large conical structures such as GBFs. Contrarily, diffraction solvers based on linear potential flow theory (e.g. WAMIT/HydroD/OrcaWave) might deliver more accurate results. Therefore, this section uses a GBF reference study to analyze the hydrodynamic loads computed using linear potential flow (OrcaWave). This study is performed for seven different wave conditions, and to validate the results, they are compared to actual CFD data, which Rambøll provided. The dimensions of the reference GBF are provided in Figure 3.12, whereas the environmental conditions for all seven examined wave simulations are given in Table 3.2.

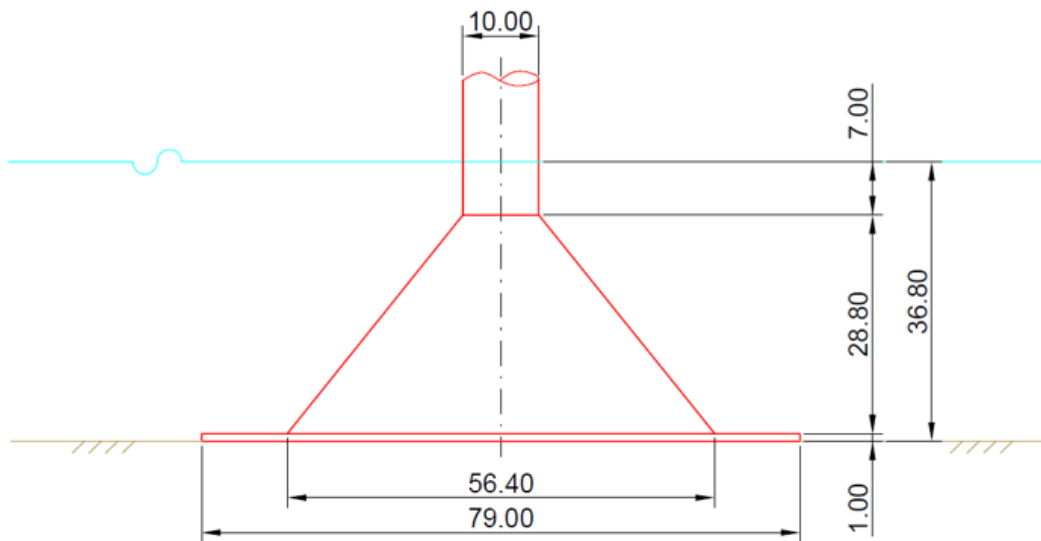


Figure 3.12: Dimensions of the reference gravity-based foundation with a water depth d of 36.8 m (by courtesy of M. Karch). All the dimensions are displayed in meters, the blue line represents the still waterline, and the mudline is shown as a brown line.

Table 3.2: Environmental conditions for all seven examined wave simulations in GBF reference study.

Wave	H [m]	T [s]	λ [m]
1	13.2	9.0	121.0
2	19.7	11.5	177.9
3	19.7	14.0	232.4
4	4.0	7.0	76.2
5	4.0	9.0	121.0
6	4.0	11.5	179.9
7	4.0	14.0	232.4

For each simulation, a single linear regular wave was modelled with a given wave height H and a corresponding period T . The wavelength λ was calculated by solving the linear wave dispersion relationship (Equation 3.4) and the wavelength formula (Equation 3.5), where ω is the angular wave frequency, g is the gravitational acceleration, k is the wave number, and d is the water depth. Furthermore, the tidal current was neglected for all wave simulations since it was found negligible for GBFs in section 2.4.

It can be seen that waves 1-3 are relatively steep and, therefore, could represent extreme waves, which can be used for ULS (Ultimate Limit State) investigations. On the other hand, waves 4-7 are quite small, which could be seen as more common waves, and therefore be interesting for SLS (Serviceability Limit State) or FLS (Fatigue Limit State) studies. Lastly, a range of wave heights H (4.0/13.2/19.7 m) and wave periods T (7.0/9.0/11.5/14.0) have been simulated to investigate the effects of both H and T .

Wave loads regime and breaking waves

This section briefly investigates the wave loads regime (inertia and drag) and breaking waves using the reference GBF and the seven wave conditions. However, it must be kept in mind that the results are based on regular linear waves and only give a slight impression of real waves (nonlinear and irregular). Also, a general description regarding breaking waves was given in subsection 2.3.3.

As explained in the summary of the literature study (section 2.4), the drag loads are expected to have a negligible influence on the total hydrodynamic loads relative to the inertial loads. This assumption is supported by the renowned wave loads regime chart from Chakrabarti [58] in Figure 3.13.

On the left side of the figure, the reference GBF is shown and is split up into three sections: the top cylinder (green), cone (red), and bottom base (yellow). Since the cone has a varying diameter, a range is given as a red rectangle on the right chart. On the right chart, all three sections are arranged for all seven wave simulations, which correspond to the numbers in the markers. Since the cone has a varying diameter (10 - 56.4 m), there are ranges of results indicated as red rectangles.

Based on these results, the following observations have been made:

- The cylinder is slightly affected by drag loads (increases for larger wave heights); however, for GBFs, the total hydrodynamic loads are predominantly determined by the loads on the conical section. Hence, this drag contribution remains negligible. Similarly, the diffraction on the cylinder is negligible since this section is considered a slender body.
- For large wave heights, it can be generally observed that there is a slight drag contribution, and the diffraction effects are only limited to the lower sections of the cone.
- For small wave heights, the entire cone has negligible drag loads but significant diffraction effects.
- The same observation can be made for the base section, regardless of the examined wave conditions.

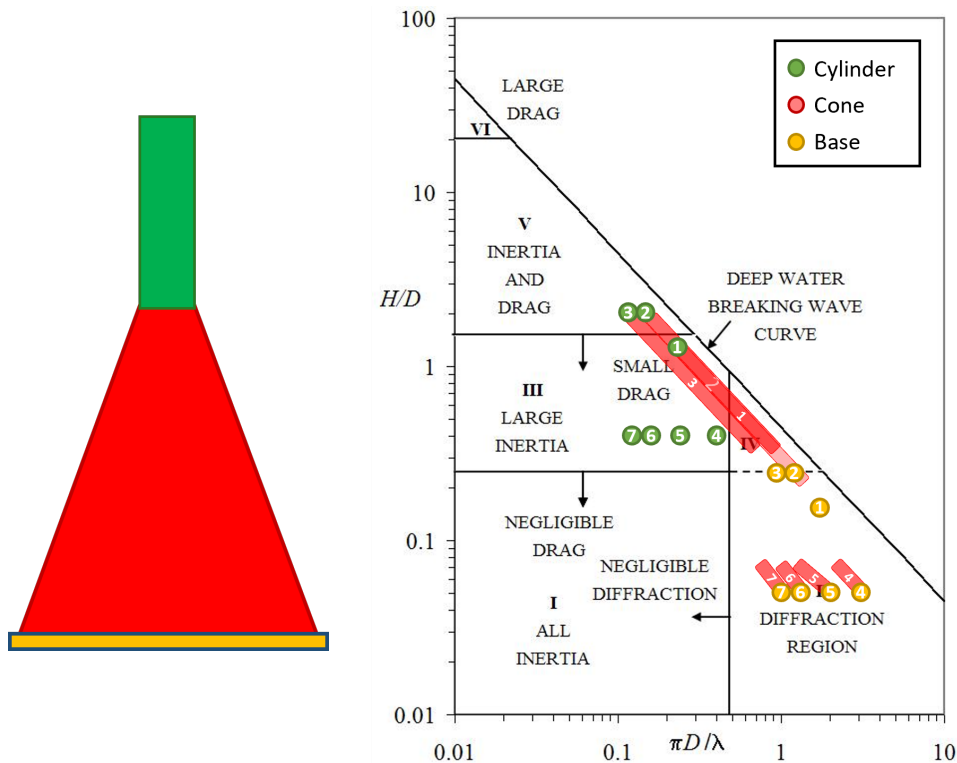


Figure 3.13: Wave loads regime for all seven waves with the reference gravity-based foundation, split into top cylinder (green), cone (red) and bottom base (yellow). It is determined by the wave height-diameter ratio H/D and the diameter-wavelength ratio $\pi D/\lambda$. Adapted from Chakrabarti [58].

Additionally, in Figure 3.14, the results for each wave are shown on a modified wave theory suitability chart, which is based on DNV-RP-C205 [21]. In this figure, it is not the wave theory suitability that is of interest but rather the breaking wave limit for each wave condition. This limit has been implemented in the figure as a red line and is a combination of the shallow water breaking limit ($H/d = 0.55$) and the deep water breaking limit ($H/L = 0.10$). The shallow water breaking limit is based on the findings of Nelson in 1994 for oscillatory waves propagating in shallow water with flat seabeds [59]. Contrarily, the deep water breaking limit was established by Kristiansen [60], using model tests from a wave tank. Since both these limits are based on empirical data, it introduces uncertainty regarding the correctness.

Figure 3.14 displays that the smaller waves (4-7) are not disturbed by any breaking wave limit, whereas all the larger waves (1-3) are around the deep water breaking limit. However, as mentioned before, these results only represent regular linear waves; therefore, in reality, there is more variance in the results. In conclusion, these giant waves likely do not exist in a natural ocean environment due to breaking waves.

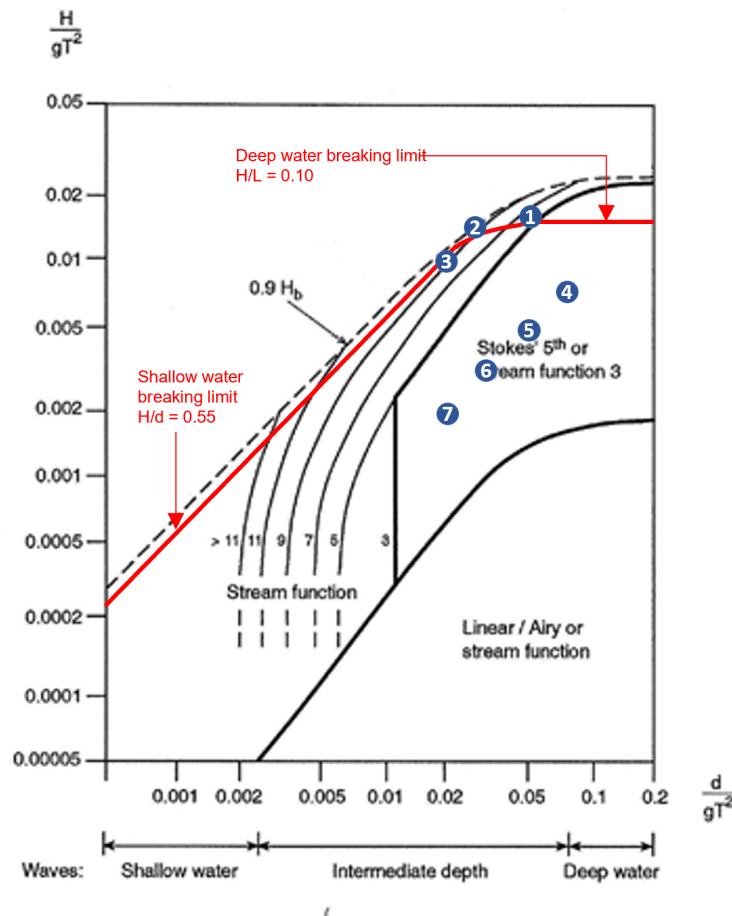


Figure 3.14: Wave theory suitability and wave breaking check for all seven wave simulations. It depends on the nondimensional wave height H and depth D . The shallow water breaking limit of 0.55 is obtained from Nelson [59], whereas the deep water breaking limit of 0.10 was established by Kristiansen [60]. Adapted from DNV-RP-C205 [21].

Computational Fluid Dynamics

As mentioned earlier, Rambøll has provided CFD data using Simcenter STAR-CCM+ [61], which is one of the most established multi-physics CFD modelling software in the industry. For each of the seven wave simulations, the reference GBF was modelled for the entire duration of one wave period using a time step of 0.10 seconds. The waves were modelled as nonlinear regular waves, and a $k - \omega$ turbulence model was applied. A numerical wave tank, where the GBF was placed in the centre, was simulated and used as the computational domain. Additionally, the reflected waves at the end of the wave tank were removed using a damping zone.

The resulting minimum, maximum, and difference for both the base shear F_x and the overturning moment M_y are provided in Table 3.3. These results include the drag and total hydrodynamic loads until the free surface. Therefore, the absolute maximum values are used as the reference CFD data for the remainder of this validation study. Once again, it must be kept in mind that the CFD results are not equivalent to the actual wave loads since there are still uncertainties within the used turbulence models. However, they present the best possible approximation based on the current developments within the field of marine/ocean engineering; thus, they will be used as reference values for this thesis.

Table 3.3: Hydrodynamic loads calculated using Computational Fluid Dynamics, for each wave simulation. $F_{x,max}$, $F_{x,min}$ and ΔF_x are the maximum base shear, minimum base shear and the absolute difference. Likewise, $M_{y,max}$, $M_{y,min}$ and ΔM_y are the maximum overturning moment, minimum overturning moment and the absolute difference.

Wave	$F_{x,max}$ [MN]	$F_{x,min}$ [MN]	ΔF_x [MN]	$M_{y,max}$ [MNm]	$M_{y,min}$ [MNm]	ΔM_y [MNm]
1	57.0	-46.5	103.6	1210	-1258	2468
2	91.3	-66.0	157.3	2302	-2515	4816
3	99.2	-63.9	163.1	2441	-2732	5172
4	10.4	-9.9	20.3	42.0	-37.3	79.4
5	16.9	-15.1	31.9	353	-316	668
6	20.4	-17.4	37.8	551	-537	1088
7	19.0	-19.5	38.5	606	-595	1201

3.3. Hydrodynamic load model based on linear potential flow

In this section, information can be found regarding the process of obtaining a hydrodynamic load model based on a linear potential flow solution (OrcaWave) for this GBF reference study. The theory behind this solution has been previously described in subsection 2.1.4. However, although CFD models can produce sufficiently accurate results, they require enormous amounts of computational power and therefore are not feasible during the preliminary design phase. Thus, an alternative hydrodynamic load model is needed, and a diffraction solver based on linear potential flow theory (e.g. OrcaWave) could be a suitable alternative.

First, to be able to calculate the loads on the surface area of the structure, a mesh panel model had to be created. Next, the optimal number of panels was found by performing a mesh sensitivity analysis. Subsequently, the hydrodynamic loads were obtained by importing this mesh panel model into OrcaWave and running a diffraction analysis. In this analysis, the GBF is assumed to be a rigid body with six fixed degrees of freedom (surge, sway, heave, roll, pitch, and yaw).

Mesh panel model

To create an LPF solution, the structure's mesh panel model must be created. This can quickly be done by various 3D modelling software. However, a parametric design tool would reduce the time needed for a sensitivity analysis (chapter 6) consisting of dozens of different designs. Therefore, with the assistance of Rambøll, a custom GBF design tool in MATLAB was created. This tool can produce a GBF mesh panel model as an .GDF file within a few seconds, merely using a few input parameters (environmental conditions, structure dimensions, and mesh parameters). Furthermore, to reduce computational time, it can symmetrically model only half or a quarter of the structure, essentially reducing the number of elements by two or four. Furthermore, it can also produce the required free surface mesh to include the second-order nonlinear wave effects, which will be investigated in subsection 4.4.2.

As mentioned before in subsection 2.1.4, a sufficient number of quadrilateral panels is required for an accurate result. However, this will also increase the computational time. Therefore, a convergence study has been executed to find the optimal number of panels. It can be found by consecutively expanding the number of panels until the solution converges within an allowed tolerance.

For the given reference GBF, a mesh sensitivity analysis was performed by using models with varying numbers of panels (778/1587/2785/6263). To compare the various mesh models, wave four ($H = 13.2$ m & $T = 9.0$ s) was selected for each calculation because it had the most significant differences. In Table 3.4, the maximum overturning moment for each mesh model is provided. The relative difference is also shown compared to each previous mesh model (with fewer panels).

Table 3.4: Mesh sensitivity study results for wave 4, where $F_{x,max}$ and $M_{y,max}$ are the maximum base shear and overturning moment. The relative difference displays the convergence of the solution for increasing number of panels.

Number of panels	$F_{x,max}$ [MN]	Difference [%]	$M_{y,max}$ [MNm]	Difference [%]
778	9.91	-	32.7	-
1587	9.92	0.10%	33.2	1.68%
2785	9.92	0.05%	33.5	0.76%
6263	9.93	0.04%	33.7	0.56%

The results show that the maximum base shear $F_{x,max}$ is already converged for the panel model with 778 elements since there is only a 0.10% difference with the more refined model (1587 panels). On the other hand, the maximum overturning moment $M_{y,max}$ converged for a model with 2785 panels with a negligible 0.76% difference compared to the model with 1587 panels.

Therefore, the mesh model with 2785 panels was selected for this GBF reference study due to its optimal balance between accuracy and computational speed, which is shown in Figure 3.15.

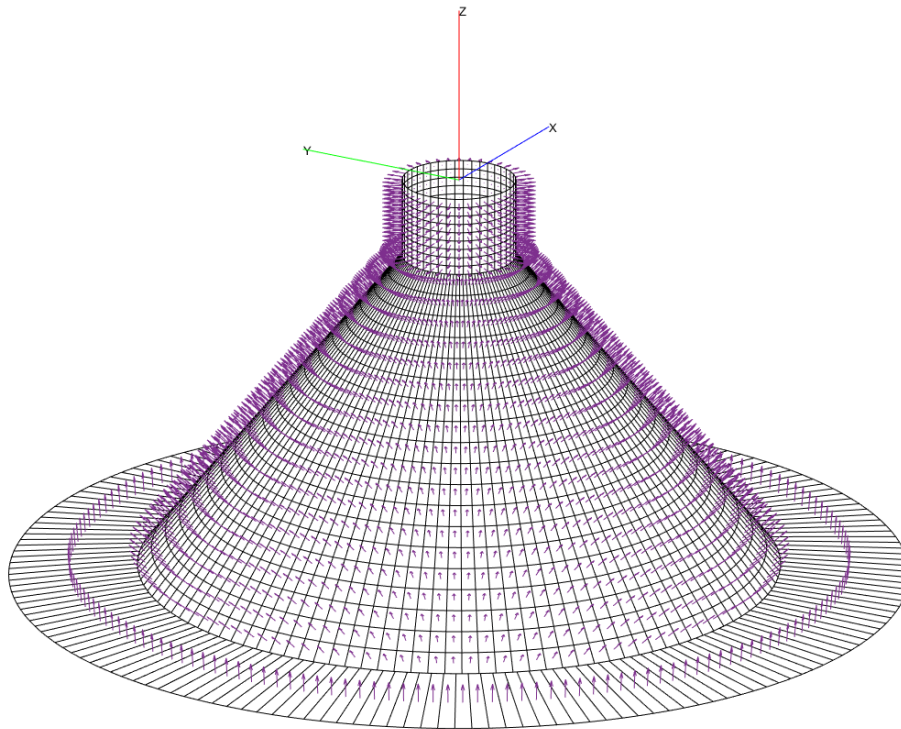


Figure 3.15: Mesh panel model with 1918 elements for a gravity-based foundation, where the panel normals (wetted surface) are indicated with purple arrows. It is modeled until the still waterline and the bottom surface is in contact with the seabed.

OrcaFlex model

After a successful diffraction analysis of the GBF in OrcaWave, the results can be imported into OrcaFlex [33], which is "the world's leading package for the dynamic analysis of offshore marine systems". Concerning the extreme loads, only the steady-state solution is considered relevant. This is the time-independent result where the transients have died out due to damping. Therefore, hydrodynamic load time series could be extracted using a Python application programming interface for OrcaFlex. Additionally, within OrcaFlex, various options could be beneficial to investigate more in detail, which will be clarified in section 4.4. An example of the reference GBF model in OrcaFlex is shown as a drawing and a graphical visualization in Figure 3.16.

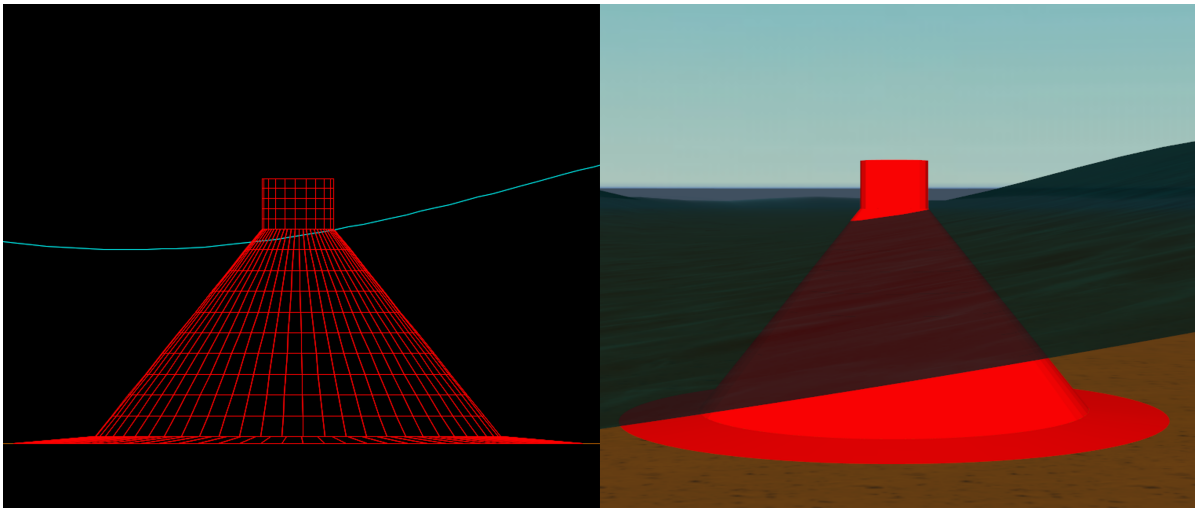


Figure 3.16: Reference gravity-based foundation modelled as a drawing (left figure) and a three-dimensional model (right figure) in OrcaFlex.

Therefore, this is the basis of the hydrodynamic load model for GBFs, which will be validated in chapter 4. Additionally, various hydrodynamic effects implemented into the OrcaFlex model will be investigated. It is important to note that this model assumes that the structure is a rigid body; therefore, the hydrodynamic loads are uncoupled with the structural dynamics of the GBF.

4

Validation of hydrodynamic load model for Gravity-Based Foundations

In chapter 3, a GBF hydrodynamic load model based on a reference study was described, which will be validated in this chapter. This model is based on an LPF solution, which was calculated using a diffraction solver (OrcaWave). The resulting hydrodynamic loads will be validated using CFD data provided by Rambøll. Initially, the base results from OrcaWave, excluding any additional effects, have been validated in section 4.1. Subsequently, in section 4.2-4.3 these results were compared with a standard monopile and various cones from the cone study performed in subsection 3.1.2. Lastly, a few potentially critical hydrodynamic effects (drag contribution, loads above SWL, and nonlinearities in waves) were investigated in section 4.4.

4.1. Validation of results using Computational Fluid Dynamics

As mentioned earlier, the resulting hydrodynamic loads were validated by comparing them with detailed CFD data. Furthermore, these loads were calculated linearly in OrcaWave, i.e. loads above the SWL and wave nonlinearities were not considered.

For the viscous effects on a blunt structure (e.g. GBFs), there is only a tiny contribution of tangential stress but a significant effect of flow separation. The vortices created due to flow separation interact with the free surface since it is not an infinite fluid, which subsequently affects the resulting hydrodynamic loads. Unlike CFD, the LPF solution does not provide any information regarding viscous effects; therefore, the drag contribution is neglected. As mentioned in section 2.4, this contribution would likely be negligible; however, to confirm this assumption, it was investigated later in subsection 4.4.3.

CFD also includes wave loads above the SWL and nonlinear wave kinematics in the incident wave field. Nonetheless, it is crucial to restate that CFD cannot reproduce the actual hydrodynamic loads in an ocean environment since there is currently no good turbulence model for oscillatory flow due to the complex turbulent layers. In other words, the exact location where flow separation occurs on a large structure (e.g. GBFs) is unpredictable. Even for an expert CFD user, accuracy remains an immense problem; therefore, it should only be considered another tool that adds value to the complete model. Nonetheless, with the currently available tools, it gives the best possible approximation of the hydrodynamic loads. Therefore, to provide a baseline for comparison with LPF in this validation study, the CFD results are assumed to represent reality.

The results for all wave simulations are shown in Table 4.1, where the relative difference is the percentage difference when the results from OrcaWave (LPF) are compared to the CFD results. It must be mentioned that maximum base shear $F_{x,max}$ and maximum overturning moment $M_{y,max}$ determined using CFD are the absolute maximums (i.e. the largest absolute values). For the LPF solution, the

maximums and the absolute maximums are essentially the same, considering that a linear wave always has a constant amplitude. Additionally, a visual representation of wave simulation three is shown in Figure 4.1 because it is the wave simulation with the largest total overturning moment. Finally, the results are phase-shifted for a more practical comparison to ensure that the maximum shear forces from the LPF and CFD solution occur in the same instance. In the interest of brevity, the figures of the remaining six wave simulations are given in section B.1.

Table 4.1: Comparison between hydrodynamic load results using Computational Fluid Dynamics and linear potential flow (OrcaWave). All seven wave cases with wave height H , wave period T and wavelength λ , were simulated to obtain the absolute maximum base shear $F_{x,max}$ and overturning moment $M_{y,max}$.

Wave	H [m]	T [s]	λ [m]	CFD		LPF		Relative difference	
				$F_{x,max}$ [MN]	$M_{y,max}$ [MNm]	$F_{x,max}$ [MN]	$M_{y,max}$ [MNm]	$F_{x,max}$ [%]	$M_{y,max}$ [%]
1	13.2	9.0	121.0	57.0	1258	56.2	1007	-1.50%	-19.96%
2	19.7	11.5	177.9	91.3	2515	100.0	2781	9.58%	10.61%
3	19.7	14.0	232.4	99.2	2732	98.2	3110	-1.00%	13.83%
4	4.0	7.0	76.2	10.4	42.1	9.94	34.4	-3.98%	-18.40%
5	4.0	9.0	121.0	16.9	353	17.0	306	0.82%	-13.30%
6	4.0	11.5	177.9	20.4	551	20.3	565	-0.48%	2.57%
7	4.0	14.0	232.4	19.5	606	19.9	632	2.01%	4.18%

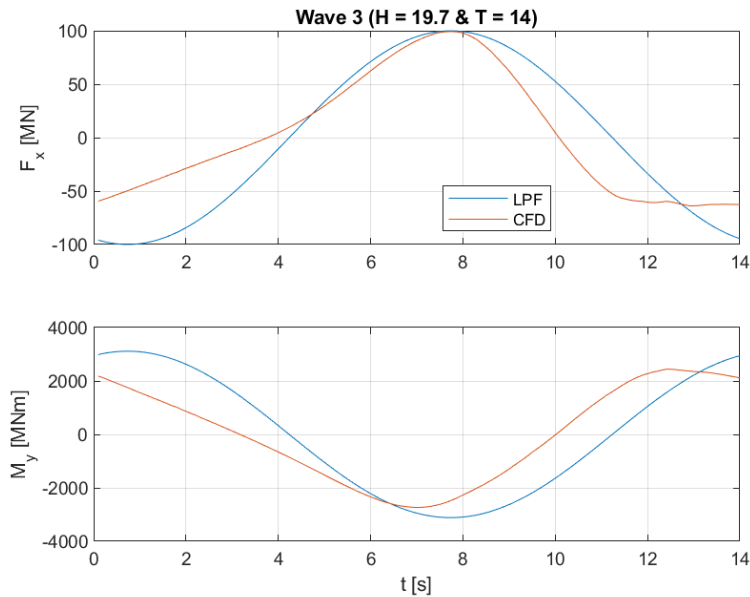


Figure 4.1: Hydrodynamic loads (base shear F_x and overturning moment M_y) comparison using linear potential flow and Computational Fluid Dynamics for wave case 3 (wave height $H = 19.7$ m and wave period $T = 14.0$ m).

By comparing the CFD and LPF results for all seven wave conditions for the reference GBF in Table 4.1, the following conclusions can be drawn:

- LPF is sufficiently accurate for small waves ($H = 4$ m), provided that both the wave period T and wave length λ are large enough ($T > 9.0$ s and $\lambda > 121.0$ m).
- Generally, large waves ($H = 19.2$ m) produce LPF solutions that are overly conservative (up to 13.83% larger), which increases even further for increasing wave period. In practice, conservative results are acceptable for extreme (ULS) waves because you want to be confident that the structural integrity does not fail.

- As seen from waves 1, 4, and 5, if the wave period or wavelength becomes too small ($T < 9.0$ s and $\lambda < 121.0$ m), it will result in an underestimation of the overturning moment (up to 19.96% smaller).
- For increasing wave heights H , the deviations in hydrodynamic loads between CFD and LPF also increase.

Additionally, to identify patterns in the hydrodynamic loads, scatter plots have been provided in Figure 4.2-4.5. These plots slightly investigate the relationship between the base shear and overturning moment with the wave height and wave period.

It must be noted that seven simulations cannot provide sufficient data to display the relationships accurately; therefore, based on these scatter plots, only a few general trends can be described:

- For most wave conditions, the base shear seems sufficiently accurate. There is only one exception, which is wave 3 ($H = 19.7$ m & $T = 11.5$ s).
- For increasing wave heights, the difference in the overturning moment also increases.
- No correlation can be found between overturning moment and wave period.

An alternative value that could have been a better measure in comparison with the maximum magnitudes ($F_{x,max}$ and $M_{y,max}$) is the integrated impulse (force over time). This is physically more correct since it also takes the duration of the action into account. For example, it is possible that a structure tips over by a smaller load than the maximum load provided that the duration of the smaller load is high enough.

The positive time-integrated impulse can be obtained by isolating all the positive loads in a single wave period from the time series and subsequently integrating them. The negative time-integrated impulse can be obtained similarly; however, the negative loads are used. Nevertheless, this is not easy to incorporate in standard design checks, where maximum loads are often used, and therefore, the time-integrated impulse is discontinued in this thesis.

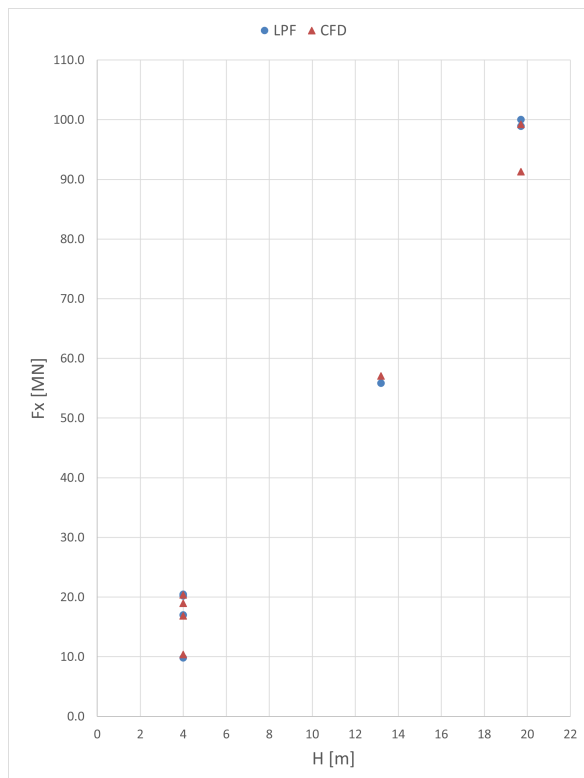


Figure 4.2: Base shear F_x w.r.t. wave height H for all seven wave cases.

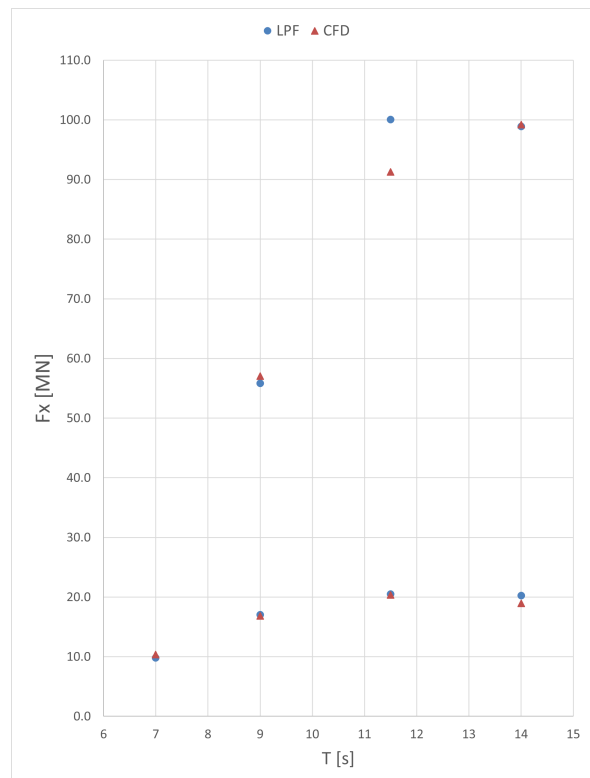


Figure 4.3: Base shear F_x w.r.t. wave period T for all seven wave cases.

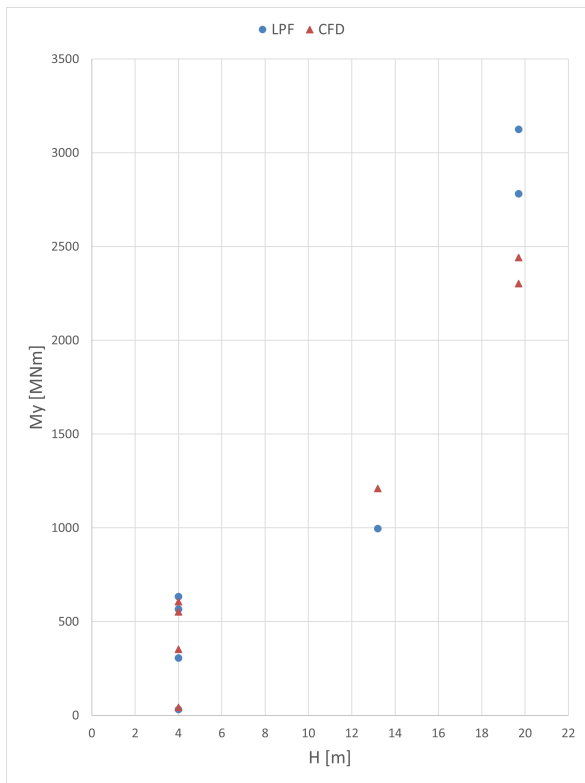


Figure 4.4: Overturning moment M_y w.r.t. wave height H for all seven wave cases.

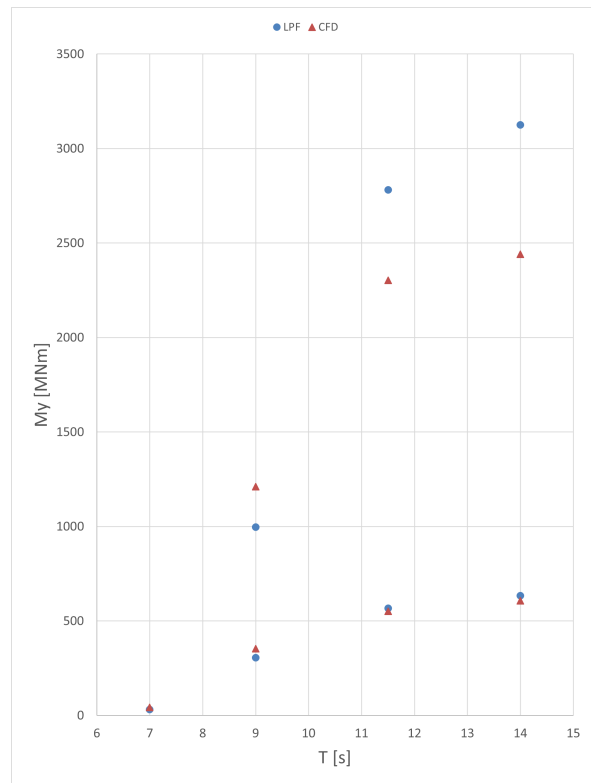


Figure 4.5: Overturning moment M_y w.r.t. wave period T for all seven wave cases.

4.2. Comparison with monopile

This section compares the hydrodynamic loads on the reference GBF with the hydrodynamic loads on a monopile. This monopile has a constant diameter equal to the GBF’s top diameter $D_{top} = 10$ m. The mesh model was created similarly to the GBF and consisted of 1184 panels. The reference GBF and the monopile models in OrcaWave are visualised in Figure 4.6.

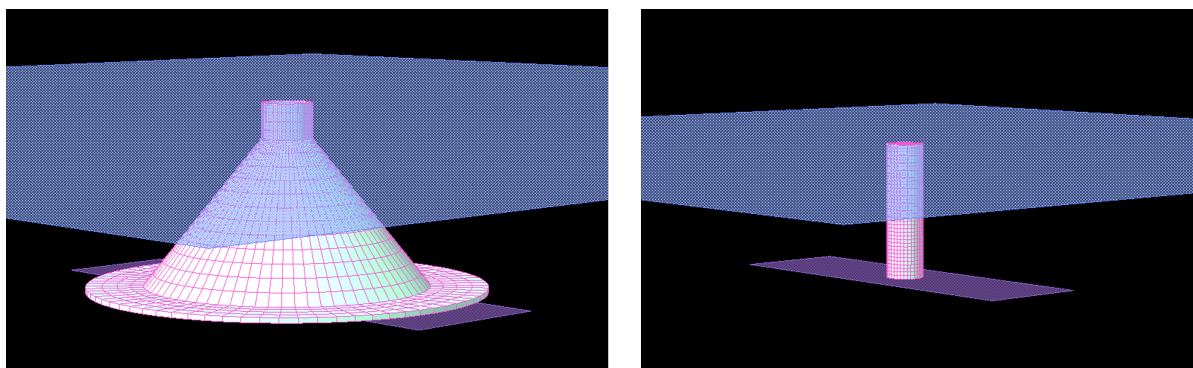


Figure 4.6: Reference gravity-based foundation (left figure) and monopile (right figure) modelled in OrcaWave. The still waterline and seabed are displayed as blue and purple planes respectively.

For this study, it was not necessary to import the OrcaWave result into OrcaFlex because additional hydrodynamic effects were not investigated. Instead, the hydrodynamic loads were calculated with the same diffraction solver program (OrcaWave) and environmental conditions (Table 3.2). The results for all seven wave cases are given in Table 4.2, whereas only the plot for wave 3 is shown in Figure 4.7. The resulting plots for the remaining wave simulations can be found in section B.2.

In general, the following conclusions can be drawn:

- The hydrodynamic loads on the monopile have a significantly lower magnitude than the loads on the GBF. This was expected since the GBF has a much larger surface area, so more panels are subjected to hydrodynamic pressure.
- The monopile does not cause any phase lag between the base shear F_x and the overturning moment M_y ; meanwhile, this phase lag is apparent for the reference GBF.
- At $T/2$, the loads are exactly zero for the monopile; however, there is a slight delay for the loads on the reference GBF.

Table 4.2: Comparison between hydrodynamic loads on the reference gravity-based foundation and monopile, for all seven wave cases (wave height H , wave period T and wavelength λ). Here, the absolute maximum base shear $F_{x,max}$, absolute maximum overturning moment $M_{y,max}$ and the relative difference between the results of the two structures are provided.

Wave	H [m]	T [s]	λ [m]	Monopile		GBF		Relative difference	
				$F_{x,max}$ [MN]	$M_{y,max}$ [MNm]	$F_{x,max}$ [MN]	$M_{y,max}$ [MNm]	$F_{x,max}$ [%]	$M_{y,max}$ [%]
1	13.2	9.0	121.0	10.3	232	56.2	1007	445%	334%
2	19.7	11.5	177.9	13.7	282	100.0	2781	630%	886%
3	19.7	14.0	232.4	12.0	238	98.2	3110	719%	1207%
4	4.0	7.0	76.2	3.2	83.2	9.9	34.4	211%	-59%
5	4.0	9.0	121.0	3.1	70.2	17.0	306	448%	336%
6	4.0	11.5	177.9	2.8	57.4	20.3	565	624%	885%
7	4.0	14.0	232.4	2.4	48.2	19.9	632	730%	1211%

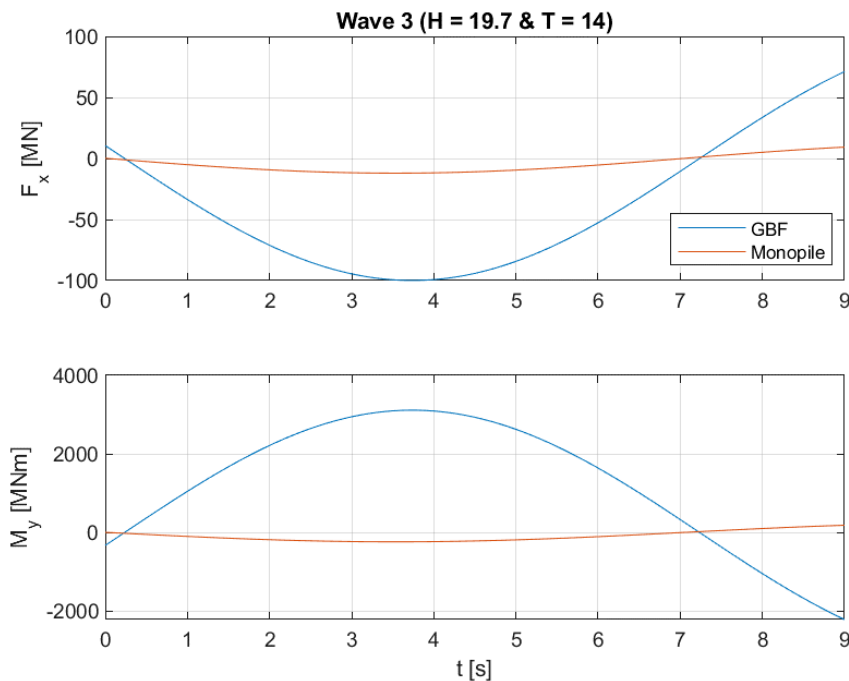


Figure 4.7: Hydrodynamic loads (base shear F_x & overturning moment M_y) comparison between the reference gravity-based foundation and a monopile (diameter $D = 10$ m) for wave 3 (wave height $H = 19.7$ m & wave period $T = 14.0$ m).

4.3. Comparison with cone study

In this section, the reference GBF is compared with the seven examined conical structures in the cone study (subsection 3.1.2). This comparison aims to examine the influence of the GBF's conical section on the hydrodynamic loads, which can be done by locating similarities or differences between the results. The hydrodynamic loads on the GBF are simulated using LPF in OrcaWave.

In Figure 4.8, the resulting overturning moment (with and without vertical force contribution) on the GBF is given for the largest wave height ($H = 19.7$ m) over the range of wave periods $T = [4;20]$. The plots for the other wave heights (4.0 and 13.2 m) have been disregarded, as they produced identical shapes with lower magnitudes. This is done similarly to the cone study's seven examined conical structures.

Based on the results, it is apparent that the pattern of the loads on the GBF follows the results from the largest examined conical structure (Figure 3.11). This is because the size of the conical sections of both structures is quite similar, i.e. for both structures, the bottom diameter is roughly six times the size of the top diameter. Therefore, it can be concluded that the conical shape of the reference GBF is responsible for most of the hydrodynamic loads.

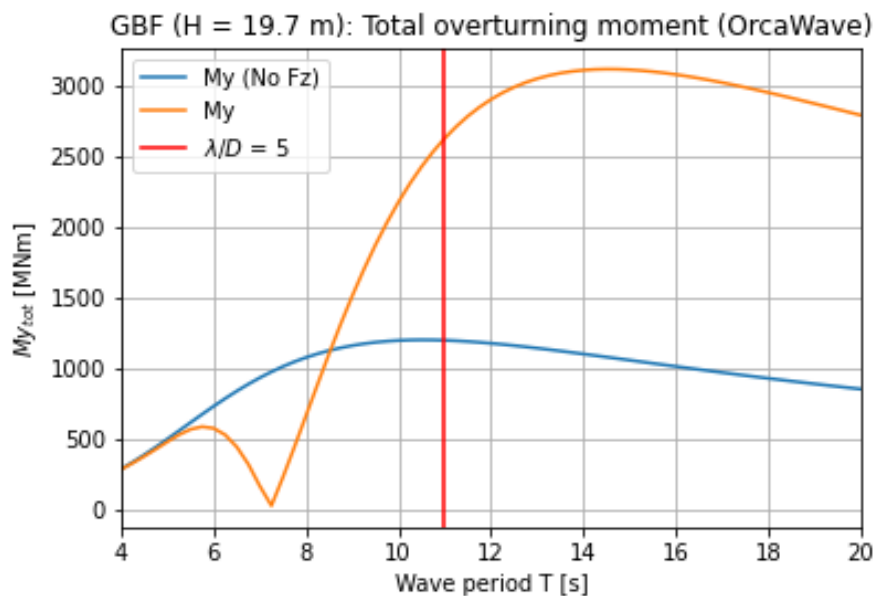


Figure 4.8: Comparison of the overturning moment M_y , including and excluding the vertical contribution of the pressure F_z , for the reference gravity-based foundation with wave height $H = 19.7$ m. The diffraction limit based on the wavelength λ and the average diameter D is represented as a red line.

4.4. Research regarding additional hydrodynamic effects

So far, the hydrodynamic models have been created in OrcaFlex using a simple linear potential flow solution while neglecting other phenomena that could potentially significantly affect the results. Therefore, in this section, the following effects were investigated to determine if they had to be implemented in the final hydrodynamic model:

- Wave loads up to the instantaneous linear free surface
- Nonlinear wave loads (up to second-order)
- Drag load contribution

4.4.1. Wave loads up to the instantaneous linear free surface

The standard LPF solution calculates the wave loads based on wave kinematics until the SWL. In reality, the wave loads extend to the free surface, which is determined by the wave height. These loads above the SWL can be significant for the total overturning moment because although they have a lower magnitude, the length of the moment arm is increased. More specifically, if the wave height is high, these loads will have an even more significant impact on the total overturning moment.

Within OrcaFlex, a spar buoy element could be added to the structure to extend the wave kinematics by extrapolation (Figure 4.9). Afterwards, the wave loads up to the instantaneous linear free surface were calculated. It has been concluded in section 3.2 that a GBF is highly likely to be inertia dominated. As mentioned in subsection 2.1.2, this would result in low KC numbers, and therefore a constant inertia coefficient $C_M = 2$ was used.

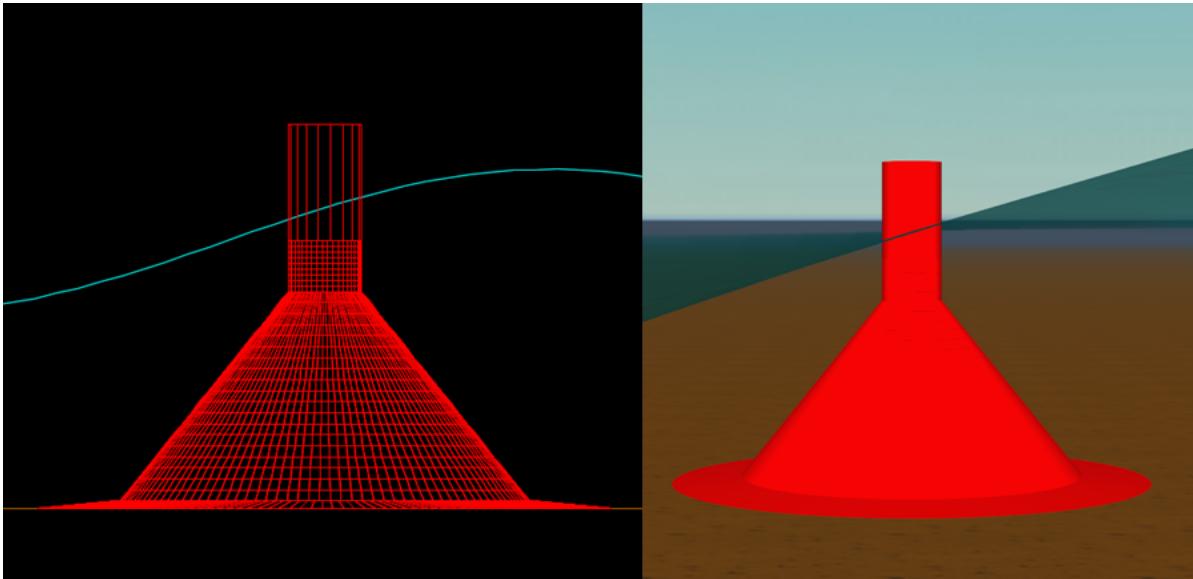


Figure 4.9: Reference gravity-based foundation, including a cylinder above the still waterline, modelled in OrcaFlex. The left figure shows the drawing, whereas the right figure displays the three-dimensional model.

It is good to know that there are some similarities between this effect and nonlinear (second-order) wave loads (subsection 4.4.2). However, only a part of the second-order potential flow solution is captured by extrapolating the linear wave kinematics up to the instantaneous linear free surface. It considers the free surface expansion to the second-order in the splash zone; however, it completely neglects the second-order potential and free-surface diffraction.

In Table 4.3, the resulting hydrodynamic loads, including and excluding wave loads above SWL, are given for each wave simulation. Here, it must be mentioned that $F_{x,max}$ and $M_{y,max}$ represent the absolute maximum values for the base shear and overturning moment.

Table 4.3: Comparison between hydrodynamic loads (absolute maximum base shear $F_{x,max}$ and absolute maximum overturning moment $M_{y,max}$), including and excluding loads up to the instantaneous linear free surface. The various simulations are based on the reference gravity-based foundation and seven wave cases (wave height H , wave period T and wavelength λ).

Wave	H [m]	T [s]	λ [m]	Until SWL		Until FS		Difference	
				$F_{x,max}$ [MN]	$M_{y,max}$ [MNm]	$F_{x,max}$ [MN]	$M_{y,max}$ [MNm]	$F_{x,max}$ [%]	$M_{y,max}$ [%]
1	13.2	9.0	121.0	56.0	1010	56.9	1010	1.49%	0.00%
2	19.7	11.5	177.9	99.8	2785	100.7	2785	0.96%	0.00%
3	19.7	14.0	232.4	98.1	3112	98.6	3112	0.53%	0.00%
4	4.0	7.0	76.2	9.92	33.5	10.1	41.7	1.43%	24.47%
5	4.0	9.0	121.0	17.0	306.2	17.0	306.2	0.42%	0.00%
6	4.0	11.5	177.9	20.3	565.5	20.3	565.5	0.15%	0.00%
7	4.0	14.0	232.4	19.9	631.8	19.9	631.8	0.10%	0.00%

Based on the results, it can be concluded that the differences in base shear are always negligible. Nonetheless, the differences in the overturning moment are also negligible, except for waves with low wave periods ($T < 9.0$ s). This can be seen from the resulting overturning moment in wave 4 ($T = 7.0$ s), whereby including the loads above SWL, there is a significant increase of 24.47%.

As seen in Table 4.4, the wave loads calculated up to the FS are more in line with the CFD data. There is only a negligible difference of 1.07% between the absolute maximum overturning moment for CFD and LPF (until FS), whereas the difference between CFD and LPF (until SWL) is quite significant (20.51%). Therefore, it is recommended to include loads until the instantaneous linear surface for waves with small wave periods.

Table 4.4: Comparison of hydrodynamic loads (absolute maximum base shear $F_{x,max}$ and absolute maximum overturning moment $M_{y,max}$) for wave 4 ($H = 4.0$ m & $T = 7.0$ s), using Computational Fluid Dynamics, linear potential flow until the still waterline, and linear potential flow until the instantaneous linear free surface.

CFD		LPF (until SWL)		LPF (until FS)	
$F_{x,max}$ [MN]	$M_{y,max}$ [MNm]	$F_{x,max}$ [MN]	$M_{y,max}$ [MNm]	$F_{x,max}$ [MN]	$M_{y,max}$ [MNm]
10.35	42.11	9.92	33.47	10.07	41.66
Difference w.r.t. CFD		-4.11%	-20.51%	-2.74%	-1.07%

As previously mentioned, the hydrodynamic loads on GBFs are predominantly determined by the inertial loads, which depend on wave-particle acceleration. Therefore, smaller wave periods result in more significant wave-particle accelerations (especially above the SWL) and, subsequently, larger loads. Additionally, there can be a phase difference that causes the loads above the SWL to counteract the hydrodynamic loads below the SWL. This phase difference will likely occur for waves with small wavelengths compared to the structure's average diameter, since the phasing of the loads vary considerably along the wave relatively to the size of the structure. I.e., for small wavelengths relative to the diameter, the frontal wave loads will be canceled out by the loads from behind the structure. Contrarily, for large wavelengths relative to the diameter, these loads will be intensified.

For a further clarification, a comparison between wave 4 ($H = 4.0$ m & $T = 7.0$ s) and wave 7 ($H = 4.0$ m & $T = 14.0$ s) was made in Figure 4.10-4.11. For both waves, a single wave period has been examined, where the blue lines represent the overturning moment M_y , the green lines represent the wave-particle acceleration at SWL a , and the purple dotted lines display the minimum overturning moment $M_{y,min}$, and the red dotted line displays the maximum overturning moment $M_{y,max}$.

First, it can be observed that the magnitude of a is much larger for wave 4 compared to wave 7 (approximately 3 times larger). Furthermore, for wave 4, a is negative at $M_{y,max}$, whereas it is positive and at

$M_{y,min}$. The loads above the SWL are counteracting the total loads, causing the magnitude of $M_{y,min}$ (41.7 MN) to be larger than $M_{y,max}$ (33.5 MN). Therefore, $M_{y,min}$ represents the absolute maximum overturning moment for wave 4.

Contrarily, in wave 7, a tracks the shape of M_y , i.e. the minimum and maximum values for a occur simultaneously for M_y . Furthermore, there are no counteracting loads due to phase differences and the magnitude of $M_{y,min}$ is similar to $M_{y,max}$.

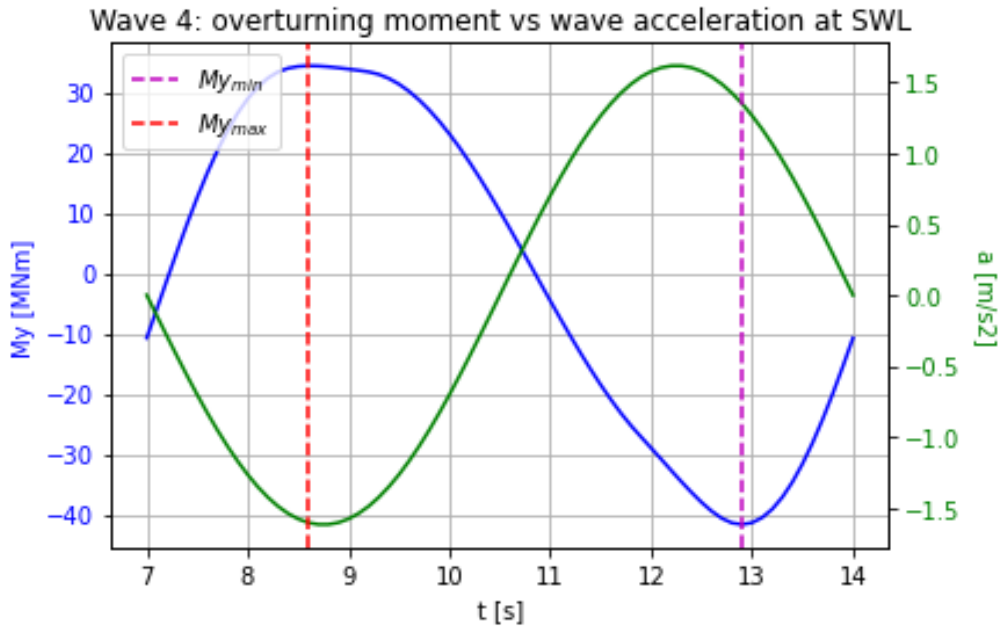


Figure 4.10: Overturning moment M_y and wave particle acceleration at the still waterline a for wave 4 ($H = 4$ m & $T = 7$ s). The purple dotted line displays the minimum overturning moment $M_{y,min}$, whereas the red dotted line represents the maximum overturning moment $M_{y,max}$.

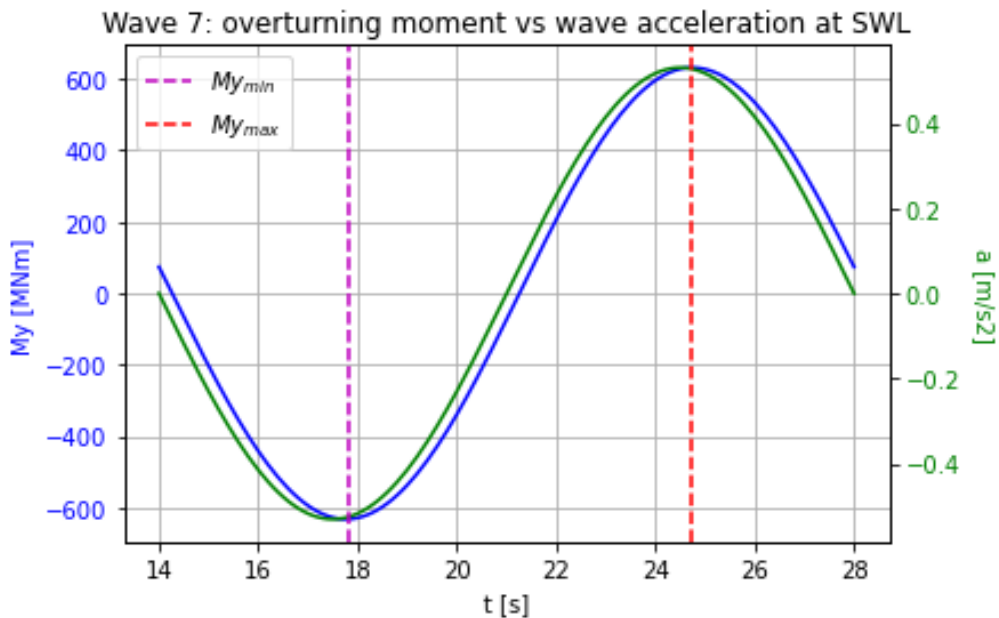


Figure 4.11: Overturning moment M_y and wave particle acceleration at the still water line a for wave 7 ($H = 4$ m & $T = 14.0$ s). The purple dotted line displays the minimum overturning moment $M_{y,min}$, whereas the red dotted line represents the maximum overturning moment $M_{y,max}$.

4.4.2. Nonlinear wave loads

This section has researched the nonlinear wave loads at the free surface. In reality, the structure can be excited at different frequencies than the period corresponding to the maximum wave height of an incident wave. The effect of these nonlinearities was isolated by examining the load difference compared to the linear potential flow solution from section 4.1. These nonlinearities' importance depends on the structure's natural frequency and environmental load frequencies, which in this case are the wave frequencies.

As mentioned by Kristiansen [34], second-order potential flow is essential for structures with low-frequency resonance (e.g. moored structures). This is because the low-frequency wave components within the wave drift loads could cause the structure to move and increase the moorings loads. Furthermore, if wave slamming and air gap motions are relevant, higher-order nonlinear potential flow solutions are required. The main challenge with second-order solutions is to achieve mesh convergence.

For GBFs, only high-frequency resonance is expected, resulting in load variations of small time durations. As the overturning moment is the most relevant for GBFs, the integral of these second-order loads will be nearly zero, and thus it is doubtful that it will be affected by it. Therefore, although the assumption is that the linear (first-order) potential flow solution would be sufficient, the second-order nonlinear potential flow solution was calculated for the reference GBF in OrcaFlex.

First, as the second-order problem requires the boundary conditions to be satisfied at the instantaneous position of the wetted body, a free surface panelled zone had to be created. This is a circular mesh model of the exterior area around the structure and is located at the SWL. A representation of this free surface panelled zone connected to the reference GBF mesh panel model is provided in Figure 4.12.

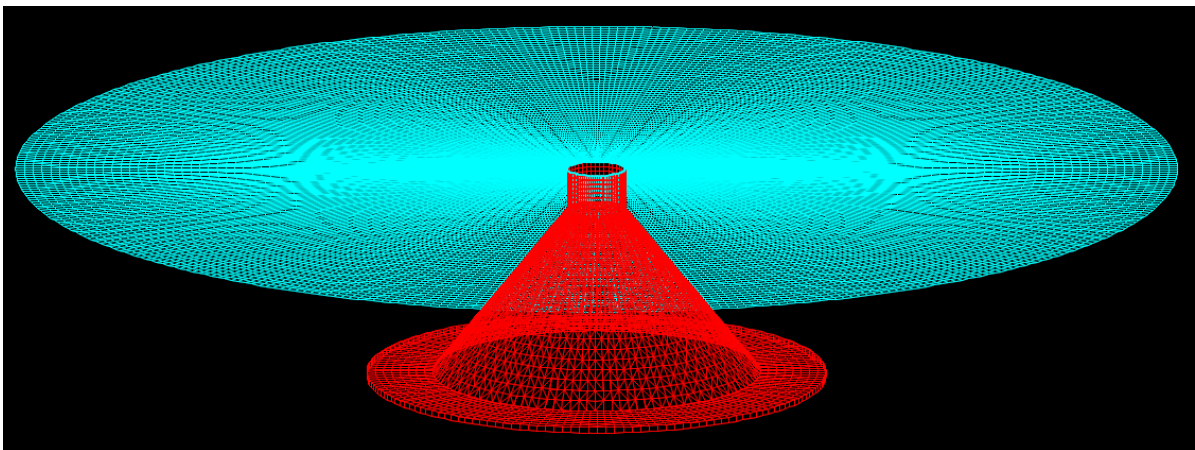


Figure 4.12: Free surface panelled zone with a radius of 100 m combined with the mesh panel model of the reference gravity-based foundation.

Subsequently, the quadratic transfer functions were calculated to examine the second-order solution while considering the free surface panelled, quadrature, outer circle, and asymptotic zone data. These options were described using the following parameters:

- Free surface panelled zone: inner radius and mesh size;
- Free surface quadrature zone: number of annuli, radius step, radial nodes, and azimuthal nodes;
- Free surface outer circle: outer radius, number of segments;
- Free surface asymptotic zone: expansion order.

To investigate the effect of each parameter, they were varied in dozens of simulations. Since these second-order solutions required a substantial amount of computational power, a detailed QTF study was out of the scope of this thesis. For each wave condition, six different configurations were simulated for the same reference GBF. This resulted in a significant variance of results, whereas convergence was never achieved. According to Kristiansen et al. [60], to achieve convergence, the number of nodes is far more critical than the size of the outer radius.

A brief example of the results is given in Table 4.5, which shows the CFD data and the first-order solution and second-order (inner radius of 100 m and no further options enabled) solutions for each wave condition. Here, the specified loads are the absolute maximum values. Furthermore, the results of all the nonlinear (second-order) potential flow simulations for each wave condition can be found in section B.3.

Table 4.5: Comparison between hydrodynamic loads (absolute maximum base shear $F_{x,max}$ and absolute maximum overturning moment $M_{y,max}$) calculated using Computational Fluid Dynamics, linear potential flow until the instantaneous linear free surface (Table 4.3), and nonlinear second-order potential flow (inner radius of 100 m).

Wave	H [m]	T [s]	λ [m]	CFD		Linear PF (until FS)		Nonlinear PF	
				$F_{x,max}$ [MN]	$M_{y,max}$ [MNm]	$F_{x,max}$ [MN]	$M_{y,max}$ [MNm]	$F_{x,max}$ [MN]	$M_{y,max}$ [MNm]
1	13.2	9.0	133.3	57.0	1258	56.9	1010	56.9	1116
2	19.7	11.5	200.0	91.3	2515	100.7	2785	112.0	3052
3	19.7	14.0	258.1	99.2	2732	98.6	3112	119.3	3183
4	4.0	7.0	78.3	10.4	42.1	10.1	41.7	10.2	58.1
5	4.0	9.0	122.5	16.9	352.7	17.0	306.2	17.1	314.5
6	4.0	11.5	179.0	20.4	551.2	20.3	565.5	21.0	578.2
7	4.0	14.0	234.2	19.5	606.4	19.9	631.8	20.9	635.4

Based on the results, the following conclusions were drawn:

- The nonlinear second-order potential flow solution generally produces more conservative solutions than the linear potential flow solution.
- By varying the various parameters in the nonlinear second-order potential flow solution, there was a large variance in the resulting hydrodynamic loads. As a result, there are many uncertainties w.r.t. the correct modelling of this solution. Thus for a better understanding, in-depth research using a considerable amount of computational power has to be executed (out of scope for this thesis).
- There is an insignificant difference in resulting hydrodynamic loads when nonlinear waves (Dean's stream function) are used instead of linear (Airy) waves for calculating the wave loads above SWL.

4.4.3. Contribution of drag load

As mentioned before, the drag load was expected to be negligible since GBFs are affected mainly by inertial loads. Nonetheless, this hypothesis had to be confirmed by performing a study. This was achieved by using the Morison element feature in OrcaFlex, which allows the implementation of a parallel drag load model based on Morison's equation. To avoid unnecessarily complicating this study, the structure was represented in only four Morison elements, and a fixed hydrodynamic drag coefficient C_D of 1.2 was used for all elements. A visualization of this Morison elements model is provided in Figure 4.13, which is based on the same reference GBF as shown in Figure 3.12. Lastly, the dimensions and colour of each Morison element are described in Table 4.6.

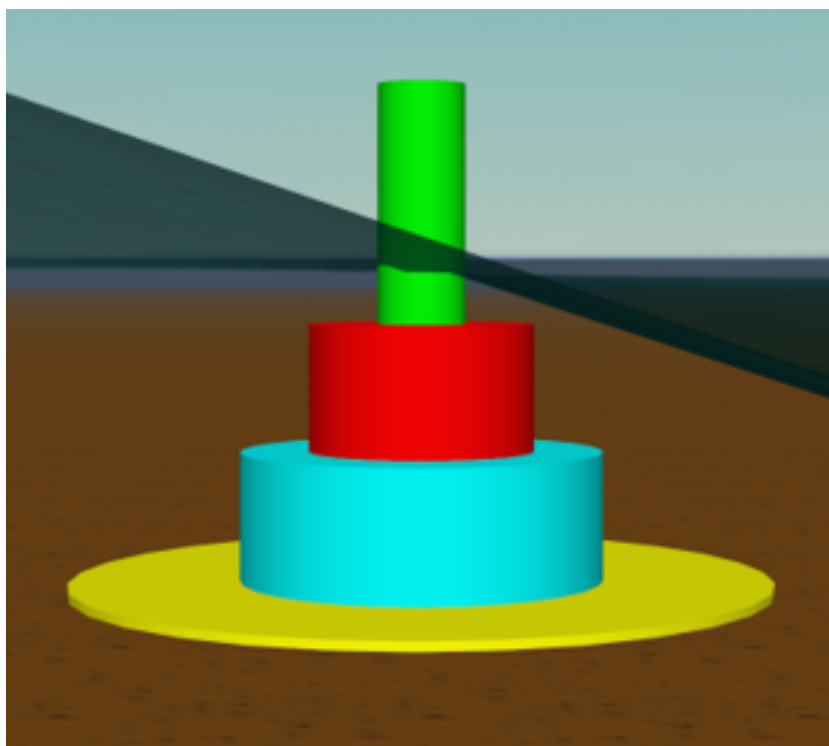


Figure 4.13: Reference gravity-based foundation modeled in four Morison elements of varying diameters (top cylinder, upper half of cone, lower half of cone, and bottom base) in OrcaFlex, while using a constant drag coefficient $C_D = 1.2$ for all elements.

Table 4.6: Dimensions and colors of each Morison element from Figure 4.13.

Morison element	Color	Diameter [m]
Top cylinder	Green	10.0
Upper half of the cone	Red	25.5
Lower half of the cone	Blue	40.9
Bottom base	Yellow	79.0

Using this Morison element model, the horizontal drag loads could be calculated. However, unlike the inertial loads calculated using LPF(OrcaWave), this model did not consider the vertical drag loads and diffraction effects caused by the drag. Therefore, a CFD model is required if these additional effects are of interest. Nevertheless, this simple investigation would not add additional value to the results.

In Table 4.7, the absolute maximum base shear $F_{x,max}$ and absolute maximum overturning moment $M_{y,max}$ for both the hydrodynamic models with and without drag loads (Morison element) are provided. The minimum and maximum loads had different magnitudes due to the phase differences between drag and inertia; therefore, the absolute maximum value was introduced. The relative difference between the results, including drag and excluding drag, is also shown. For this comparison, the loads above the SWL were not considered.

Additionally, to ensure that the drag loads above the SWL were insignificant, a similar comparison was made in Table 4.8. Here, the difference is that the models included the loads until the instantaneous linear free surface, as described in subsection 4.4.1.

Based on the results, the following conclusions were drawn:

- By adding the drag influence (Morison) to the linear potential flow solution (inertial loads), it generally results in a slightly higher $F_{x,max}$ and a slightly smaller $M_{y,max}$.
- For all wave conditions, the contribution of the drag loads until SWL is negligible for this GBF.
- For all wave conditions, except waves with small wave periods (e.g. wave 4), the contribution of the drag loads until the instantaneous linear free surface is also negligible. Similarly to the inertial loads (subsection 4.4.1), lower wave periods may result in phase differences and increased wave-particle velocities. However, the relative increase in velocity is smaller than the relative increase in acceleration.
- Even for waves with short wave periods ($T < 9.0$ s), the contribution of the drag loads above SWL is still relatively low compared to the inertial loads above SWL. Nevertheless, the drag loads above SWL can significantly affect larger waves with short wave periods.
- By implementing the tidal current, the wave-particle velocity will increase and, therefore, the drag loads. This effect was, however, not validated since, in this master thesis, there is no CFD data available, which also includes the current.

Table 4.7: Comparison between hydrodynamic loads (absolute maximum base shear $F_{x,max}$ and absolute maximum overturning moment $M_{y,max}$), including and excluding drag loads up to the still water line. The various simulations are based on the reference gravity-based foundation and seven wave cases (wave height H , wave period T and wavelength λ).

Wave	H [m]	T [s]	λ [m]	Excluding drag		Including drag		Difference	
				$F_{x,max}$	$M_{y,max}$	$F_{x,max}$	$M_{y,max}$	$F_{x,max}$	$M_{y,max}$
				[MN]	[MNm]	[MN]	[MNm]	[%]	[%]
1	13.2	9.0	121.0	56.0	1010	56.2	1008	0.25%	-0.28%
2	19.7	11.5	177.9	99.8	2785	100.0	2782	0.25%	-0.11%
3	19.7	14.0	232.4	98.1	3112	98.2	3110	0.18%	-0.06%
4	4.0	7.0	76.2	9.92	33.5	9.94	33.9	0.13%	1.26%
5	4.0	9.0	121.0	17.0	306.2	17.0	305.9	0.08%	-0.09%
6	4.0	11.5	177.9	20.3	565.5	20.3	565.4	0.05%	-0.02%
7	4.0	14.0	232.4	19.9	631.8	19.9	631.7	0.04%	-0.02%

Table 4.8: Comparison between hydrodynamic loads (absolute maximum base shear $F_{x,max}$ and absolute maximum overturning moment $M_{y,max}$), including and excluding drag loads up to the instantaneous linear free surface. The various simulations are based on the reference gravity-based foundation and seven wave cases (wave height H , wave period T and wavelength λ).

Wave	H [m]	T [s]	λ [m]	Excluding drag		Including drag		Difference	
				$F_{x,max}$	$M_{y,max}$	$F_{x,max}$	$M_{y,max}$	$F_{x,max}$	$M_{y,max}$
				[MN]	[MNm]	[MN]	[MNm]	[%]	[%]
1	13.2	9.0	121.0	56.9	1010	57.1	1007	0.44%	-0.36%
2	19.7	11.5	177.9	100.7	2785	101.2	2780	0.49%	-0.17%
3	19.7	14.0	232.4	98.6	3112	98.9	3109	0.35%	-0.08%
4	4.0	7.0	76.2	10.1	41.7	10.1	44.2	0.19%	6.16%
5	4.0	9.0	121.0	17.0	306.2	17.1	305.8	0.08%	-0.12%
6	4.0	11.5	177.9	20.3	565.5	20.3	565.3	0.05%	-0.04%
7	4.0	14.0	232.4	19.9	631.8	19.9	631.7	0.04%	-0.02%

4.5. Conclusion of hydrodynamic load model for GBFs

The linear potential flow solution provides a better approximation of wave loads for GBFs than Morison/MCF since it includes the vertical contribution of the pressure and diffraction effects. This is crucial for this type of structure because the large conical section predominantly determines the hydrodynamic loads.

Although LPF can be sufficiently accurate for preliminary designs, CFD remains irreplaceable for detailed designs. GBFs are complex structures and could benefit from the additional modelling features CFD offers: flow separation, detailed splash zones, and fully nonlinear wave kinematics as incident wave fields. Nonetheless, it must be kept in mind that CFD should be considered one of many tools that add value to the complete model. There are uncertainties regarding the accuracy of complex turbulence models, and the results are always highly dependent on the designer's knowledge.

This chapter established a hydrodynamic load model for GBFs based on linear potential flow in OrcaFlex. The model was validated using CFD data, and additionally, several hydrodynamic effects were examined to see their influence on the resulting loads.

First, it was found that the wave loads up to the instantaneous linear free surface were only relevant for waves with low wave periods ($T < 9.0$ s). This is because low wave periods are associated with high wave-particle kinematics and phase differences that cause counteracting loads. This effect was more prominent for the inertial loads than the drag loads above the SWL.

Secondly, GBFs are highly inertial dominated, so the drag loads proved negligible. If the inertial loads above SWL were included for waves with short wave periods, the drag load still did not have much significance.

Thirdly, the nonlinear second-order potential flow solution resulted in slightly larger hydrodynamic loads than the linear potential flow solution. This difference was even more prominent for waves with short wave periods but did not result in a more accurate result than CFD. There is a high degree of uncertainty in the results due to the complexity and required computational time of this solution. Therefore it was deemed irrelevant for the final hydrodynamic model within this master thesis.

To summarize, the contribution of the drag loads and the nonlinear second-order potential flow solution can be neglected during the preliminary design of GBFs. Additionally, the loads above the SWL up to the instantaneous linear free surface should be implemented into the standard linear potential flow solution for wave conditions with short wave periods. In this thesis, the emphasis is on extreme waves, which are associated with higher wave periods. Therefore, the final hydrodynamic model will be the same as the original linear potential flow solution without additional adjustments.

5

Design basis for Gravity-Based Foundations

In this chapter, a design basis for the GBF case study was introduced to demonstrate the design process for a GBF. The design basis is considered the primary document that describes all the essential information for a foundation designer. This design basis was created only for the conceptual design since a detailed design requires much more time and therefore seemed to be out of the scope for this master thesis.

An initial design was created based on the provided environmental conditions and WT data. The hydrodynamic loads could be calculated using the established hydrodynamic model from chapter 4. Furthermore, it was possible to check the design for two main load cases to ensure structural integrity and manufacturability. These limit state checks were based on various calculation tools, which will be further explained in section 5.3. It must be mentioned that this chapter provides merely a description of the used methods, whereas the results are found in the sensitivity analyses (chapter 6). Lastly, an optimal preliminary design can be created based on the findings.

5.1. Introduction to case study for the design basis

5.1.1. Environmental conditions

Every design basis starts with the project's location, since this determines the environmental conditions. The environmental conditions are essential for obtaining information related to the hydrodynamic loads, design dimensions, soil-structure interaction, and other design parameters.

A metocean report specifies the relevant information regarding the waves, wind, and climate. It is based on hind-cast measurements collected at specific locations. Moreover, the soil-structure interaction is investigated using site-specific geotechnical data. Generally, the WT manufacturer provides wind turbine data and maintains close contact with the foundation designer.

The used environmental conditions for this case study can be found in Table 5.2. To prevent unnecessary complications, the tidal current, extreme water levels, ice, seismic activity and marine growth are neglected within this conceptual design basis.

According to IEC61400-3-1 [17], if the metocean conditions are insufficient to assess the extreme wave height, the maximum wave height H can be estimated using Equation 5.1. A range for the corresponding extreme wave period T , based on a Rayleigh distribution, can be found using Equation 5.2.

$$H = 1.86H_s \quad (5.1)$$

$$11.1\sqrt{H_s/g} \leq T \leq 14.3\sqrt{H_s/g} \quad (5.2)$$

Based on these formulas and a given significant wave height $H_s = 13$ m, it was found that $H = 24.18$ m and $13 \leq T \leq 16$ s. The diffraction analysis was performed using both the bottom and upper limits to find the wave period corresponding to the worst loading conditions (i.e. most significant wave loads). The resulting maximum hydrodynamic loads at the mudline are provided in Table 5.1. These results concluded that $T = 13$ s produced larger hydrodynamic loads than $T = 16$ s. Hence, it can be justified that solely $T = 13$ s was used in this design basis.

Table 5.1: Comparison between the hydrodynamic loads (absolute maximum base shear $F_{x,max}$ and absolute maximum overturning moment $M_{y,max}$) for the minimum and maximum wave period T (Equation 5.2).

T	$F_{x,max}$	$M_{y,max}$
[s]	[MN]	[MNm]
13	70.4	600
16	65.04	510

Table 5.2: Environmental conditions for the gravity-based foundation case study.

Parameter	Value	Unit
Water depth d	48.00	m
Significant wave height (50 y) H_s	13.00	m
Extreme wave height H	24.18	m
Extreme wave period T	13.00	s
Sea water density ρ_w	1030	kg/m^3
Air density ρ_a	1.24	kg/m^3
Extreme 10-min average wind speed at hub height (50 y) v_{hub}	46.86	m/s
Gravitational acceleration g	9.81	m/s^2
Effective soil density γ'	9.00	kN/m^3
Characteristic friction angle ϕ_c	32.00	deg
Characteristic shear strength c_u	1.00	kN/m^3

5.1.2. Initial design dimensions for the GBF

The initial design dimensions for the preliminary GBF design are obtained by combining the environmental conditions, WT data, and guidelines based on the practical experience of Rambøll's experts. It must be taken into account that the dimensions can still vary significantly for the detailed design. The initial design configuration is provided in Table 5.3 and shown in Figure 5.1. The various dimensions have been derived based on the following guidelines:

- The top cylinder diameter D_{top} can be assumed to be equal to the bottom diameter of the tower, which for the reference WT is 8 m.
- The base diameter D_{base} needs to be smaller than the water depth (48 m).
- There is 4 m clearance on each side between the base plate and the cone bottom, i.e. the cone bottom diameter D_{bot} is 8 m smaller than D_{base} .
- The cylinder-cone transition point should be deeper w.r.t. the SWL than the extreme wave amplitude (12.09 m).

- The interface height is dependent on the required clearances for the secondary structure and the extreme wave amplitude (12.09 m).
- Both the cylindrical and conical components of the GBF are hollow from the inside to reserve space for the ballast, whereas the base plate consists of solid concrete.
- It is assumed that the structure will be filled with ballast until 3 m below the interface height.
- As a starting point, a constant base plate thickness t_{base} of 1.0 m is used, whereas the rest of the structure has a wall thickness t of 0.5 m.
- Scour protection is not considered in this master thesis. It is, however common practice to create an initial scour protection around the structure with a diameter of at least 3 time D_{base} .

Table 5.3: Initial design parameters for the reference gravity-based foundation, based on the environmental conditions and common practice.

Parameter	Value	Unit
Top cylinder diameter D_{top}	8.0	m
Cone bottom diameter D_{bot}	37.0	m
Base diameter D_{base}	45.0	m
Cylinder height $h_{cylinder}$	31.0	m
Cone height h_{cone}	32.0	m
Base plate thickness t_{base}	1.0	m
Cylinder/cone thickness t	0.5	m
Transition height z_{trans}	16.0	m
Ballast level $z_{ballast}$	13.0	m
Cylinder-cone transition point z_{trans}	-15.0	m
Cone slope angle α	24.9	deg
Concrete density ρ_{con}	2500	kg/m^3
Ballast density ρ_{bal}	2000	kg/m^3

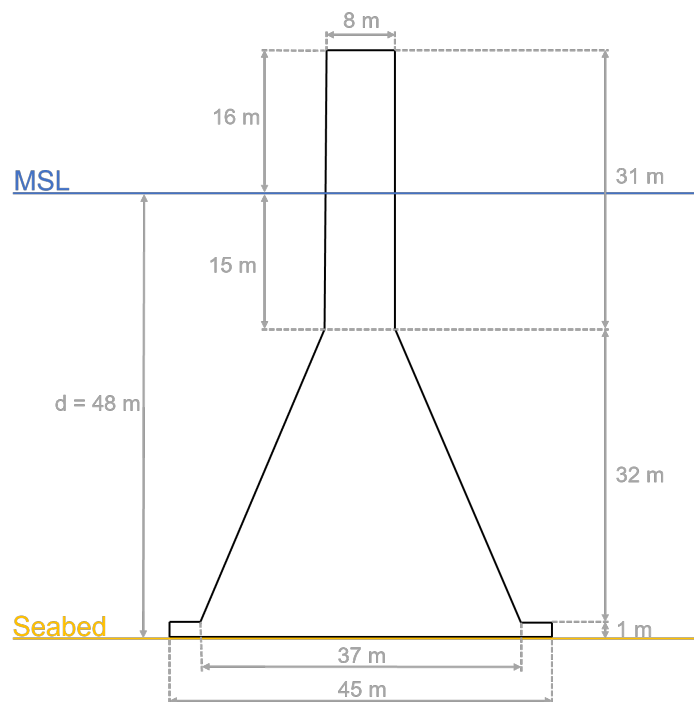


Figure 5.1: Initial design configuration of the reference gravity-based foundation.

The initial configuration should only be regarded as a rough estimation of the design and will be optimized in section 6.3 to obtain the preliminary design. Additional aspects with higher complexity have to be considered for the detailed design. An example would be the secondary structures (e.g. boat landings, platforms, and J-tubes), extensive scour protection design, and solutions to project-specific problems (e.g. connection between crane hook and GBF).

5.2. Environmental loads

5.2.1. Hydrodynamic loading

Using the relevant environmental conditions from Table 5.2 and the hydrodynamic load model described in chapter 4, the extreme characteristic hydrodynamic loads were calculated for this case study. The environmental loads for the Ultimate Limit State (ULS) (subsection 5.3.3) are obtained by multiplying the extreme characteristic loads with a partial safety factor of 1.35 [20].

Based on the experience of Rambøll's concrete experts, the hydrodynamic loads for the Serviceability Limit State (SLS) were derived by multiplying the characteristic extreme wave loads by a partial safety factor of 0.65. Therefore, it is based on a load duration distribution (LDD) of 10^{-2} , representing the load level that is exceeded 1% of the time during the entire design life. This was a sufficient estimation for the preliminary design phase since it is often correct with an error of only 0-10%.

Further investigations were initiated to find more clarity regarding the derivation of this partial safety factor. The SLS loads were computed using an irregular sea state based on two methods: time-domain and frequency-domain. These two methods follow the same procedure and only differ in which domain (time or frequency) the hydrodynamic model was simulated.

First, an omnidirectional scatter bin diagram was obtained using hindcast data from MetOceanView [62], which can be found in Appendix C. This data has the same extreme significant wave height for a return period of 50 years ($H_{s,50} = 13$ m) as the case study in this design basis. Then, to reduce the required computational resources, a reduced scatter table was created by grouping results and using a range of average significant wave heights H_s and average peak periods T_p . This reduced scatter diagram is shown in Figure 5.2. Subsequently, the directional probabilities were obtained by assuming that each of the eight directions had the same total probability of (12.5%).

		Tp [s]										
		0-2	2-4	4-6	6-8	8-10	10-12	12-14	14-16	16-18	18-20	
Hs [m]	Range	AVG	1.0	3.0	5.0	7.0	9.0	11.0	13.0	15.0	17.0	19.0
	0-2	1.0	0.0000	0.0076	0.1442	0.1910	0.0910	0.0530	0.0322	0.0134	0.0032	0.0016
	2-4	3.0	0.0000	0.0000	0.0022	0.1664	0.1360	0.0430	0.0190	0.0024	0.0016	0.0012
	4-6	5.0	0.0000	0.0000	0.0000	0.0004	0.0418	0.0260	0.0024	0.0016	0.0014	0.0002
	6-8	7.0	0.0000	0.0000	0.0000	0.0000	0.0002	0.0060	0.0020	0.0018	0.0004	0.0000
	8-10	9.0	0.0000	0.0000	0.0000	0.0000	0.0000	0.0000	0.0010	0.0010	0.0002	0.0000
	10-12	11.0	0.0000	0.0000	0.0000	0.0000	0.0000	0.0000	0.0000	0.0008	0.0004	0.0000

Figure 5.2: Reduced omnidirectional scatter diagram for a sea with a significant 50-year wave height H_{s50} of 13.0 m, which was obtained from MetoceanView hindcast data [62]. For each range of significant wave heights H_s and peak periods T_p , the average value is considered to reduce the size of the scatter table. The probabilities vary from nonexistent (green), low (yellow), medium (orange), and high (red).

By importing the data from Figure 5.2 into the diffraction solver OrcaFlex, both the time-domain and frequency-domain simulations were executed for each individual sea state. Each irregular sea state was simulated for three hours using a JONSWAP spectrum [63], defined in Equation 5.3. Here, f and f_m are the frequency and the peak frequency, which can be calculated with $1/t$ and $1/T_p$. The sea spectrum peakness factor γ is obtained using Equation 5.4 [56]. Lastly, the various spectral parameters were automatically calculated by OrcaFlex or typical values were used (Table 5.4).

$$S(f) = \frac{\alpha g^2}{16\pi^4} f^{-5} \exp \left[-\frac{5}{4} \left(\frac{f}{f_m} \right)^{-4} \right] \gamma^b$$

$$b = \exp \left[-\frac{1}{2\sigma^2} \left(\frac{f}{f_m} - 1 \right)^2 \right] \quad (5.3)$$

$$\sigma = \begin{cases} \sigma_1 & \text{for } f \leq f_m \\ \sigma_2 & \text{for } f > f_m \end{cases}$$

$$\gamma = \begin{cases} 5 & \text{for } \frac{T_p}{\sqrt{H_s}} \leq 3,6 \\ \exp \left(5,75 - 1,15 \frac{T_p}{\sqrt{H_s}} \right) & \text{for } 3,6 \leq \frac{T_p}{\sqrt{H_s}} \leq 5 \\ 1 & \text{for } \frac{T_p}{\sqrt{H_s}} > 5 \end{cases} \quad (5.4)$$

Table 5.4: Standard values for JONSWAP spectral parameters.

Parameter	Value	Unit
Gravitational acceleration g	9.81	m
Spectral width parameter σ_1	0.07	-
Spectral width parameter σ_2	0.09	-

After that, the 3-hour time series of the base shear and overturning moment were extracted from OrcaFlex into a MATLAB script for post-processing. In this script, the SLS load level was first estimated but eventually found with an iterative process. First, for the complete duration of the simulations, the number of exceedances of the SLS load was counted for each specific simulation. Then, these exceedance counts were multiplied by their corresponding probabilities and scaled to the design life. Subsequently, the exceedance percentage during design life was calculated by multiplying the sum with the duration of one time step. To achieve the desired SLS load with an LDD of 10^{-2} , this procedure was repeated by adjusting the SLS load level estimation until the desired 1% exceedance percentage criteria were met. Finally, the SLS partial safety factor was derived by dividing the final SLS load by the characteristic extreme load.

The results from the time-domain simulations are shown in Table 5.5, where it can be seen that the derived partial safety factor (0.05 for F_x and 0.04 for M_y) is significantly smaller than the conventional factor of 0.65. This seems highly unlikely since it would mean that the SLS loads are being severely overestimated in the current industry.

Contrarily, the frequency-domain simulations were executed by M. Karch, and the results are shown in Table 5.6. The obtained partial safety factors for F_x and M_y are equal to 0.61 and 0.95, which seems more promising than the time-domain results. If these factors are correct, it would mean that the standard factor of 0.65 slightly overestimates the base shear, while it significantly underestimates the overturning moment.

Table 5.5: Serviceability Limit State load results from the time-domain simulations.

Hydrodynamic load	F_x [MN]	M_y [MNm]
SLS load level	2.9	25.0
Characteristic extreme ULS load level	62.1	665.5
SLS partial safety factor [%]	0.05	0.04

Table 5.6: Serviceability Limit State load results from the frequency-domain simulations, which was executed by M. Karch.

Hydrodynamic load	F_x [MN]	M_y [MNm]
SLS load level	10.0	135.0
Characteristic extreme ULS load level	16.5	142.3
SLS partial safety factor [%]	0.61	0.95

Regardless of the validity of these findings, the base shear is not linearly dependent on the overturning moment. Therefore it does make sense to have varying safety factors for the different loads. Lastly, due to the deviation in results, the partial safety factor for the SLS loads based on common practice (0.65) was maintained in the design check calculations. However, it highlights the uncertainty of this conventional factor, and it could be interesting for future research.

5.2.2. Wind turbine data and wind loading

The WT data covers all the essential details regarding the wind turbine, which are required for a foundation design. It is provided by the WT manufacturer and depends on the project and the location. The document specifies the design parameters, wind properties, material properties, wind loads, and design requirements from the perspective of the WT manufacturer.

The design parameters consist of the dimensions and weight of the Rotor-Nacelle-Assembly (RNA) and steel tower, which has been provided for a 15MW reference WT in Table 5.7. The RNA consists of the blades, hub, and nacelle. Furthermore, the design requirements describe the recommended clearances (e.g. blade tip to water) and the frequency restrictions to avoid resonance due to the rotor frequency (1P) or the blade-passing frequency (3P). The allowed first natural frequency range for the fore-aft bending moment of the 15MW reference WT is 0.15-0.30 Hz, which is precisely in the desired soft-stiff region as seen in Figure 5.3.

Table 5.7: Design parameters for the reference wind turbine, which consists of the Rotor-Nacelle-Assembly (RNA) and the steel tower.

Parameter	Value	Unit
Rotor diameter	200	m
Number of blades	3	-
RNA mass	800	t
Tower mass	700	t
Tower length	110	m
Tower top diameter	6.0	m
Tower bottom diameter	8.0	m
Wall thickness	3-5	cm
Steel density	7850	kg/m^3

The WT manufacturer will provide the preliminary interface loads, which are the site-specific wind loads at the interface height. These loads are unidirectional and are independent of the foundation design. For the reference WT, the following wind loads (horizontal force F_v , torsional moment M_u , and bending moment M_w) at interface height are provided in Table 5.8. The normal force F_u is due to the combined weight of the RNA and tower, which is part of the permanent loads. Since this load prevents the structure from failing, it is subject to a favourable ULS partial safety factor of 0.9 and an SLS partial safety factor of 1.0 [20]. Lastly, the same environmental partial safety factors of 1.35 (ULS) and 0.65 (SLS), as discussed in subsection 5.2.1, was used for the calculation of the wind loads.

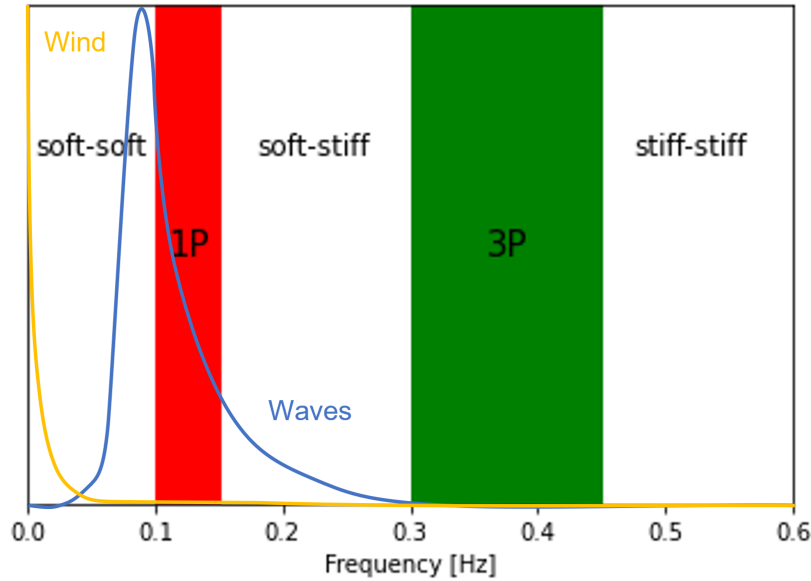


Figure 5.3: Overview of the 1P (rotational speed) & 3P (blade-passing) frequency ranges, wave spectrum, wind spectrum, and stiffness regions. A wind turbine should be designed to fall within the soft-stiff region for the optimal ratio between stiffness (to prevent resonance) and manufacturing cost.

Table 5.8: Loads at interface height for the reference wind turbine, where the horizontal force F_v , torsional moment M_u , and bending moment M_w are wind-only loads. The normal force F_u describes the total weight of the RNA and tower, and remains constant regardless of the limit state. The ULS load and SLS load are both obtained by multiplying the characteristic extreme wind loads with the corresponding load safety factor.

Interface load	Char. Extreme	ULS	SLS	Unit
Load safety factor	1.00	1.35	0.65	-
Normal force F_u	14.71	14.71	14.71	MN
Horizontal force F_v	2.59	3.50	1.69	MN
Torsional moment M_u	5.93	8.00	3.85	MNm
Bending moment M_w	259	350	168.52	MNm

5.3. Design checks of concrete Gravity-Based Foundations for offshore wind

As specified in DNVGL-ST-0437, a wind turbine's structural design depends on the verification of the structural integrity of the load-carrying components. First, the structural dynamics must not be excited due to resonance of the WT (Figure 5.3). This was checked with a natural frequency analysis using ROSAP (Rambøll Offshore Structural Analysis Programs) in subsection 5.3.1 and is crucial for the dynamic structural model of the GBF.

To ensure that the structural integrity stays within an acceptable safety range throughout the entire service life, limit state checks based on calculations that need to be performed. Generally, the foundation stability requirements drive the footprint re. In reality, the structural and soil properties change over the wind turbine's lifetime due to scour, corrosion, marine growth, soil settlement, and sand movement [20]. However, to remain aligned to create a simple preliminary design methodology, these phenomena will not be treated in-depth in this thesis.

The foundation stability checks are generally based on limiting equilibrium methods from DNV-RP-C212 [22]. The equilibrium is found when the driving forces (environmental loads) are balanced with the resisting forces (weight). In Figure 5.4, a few examples of possible failure modes for gravity-based foundations can be found.

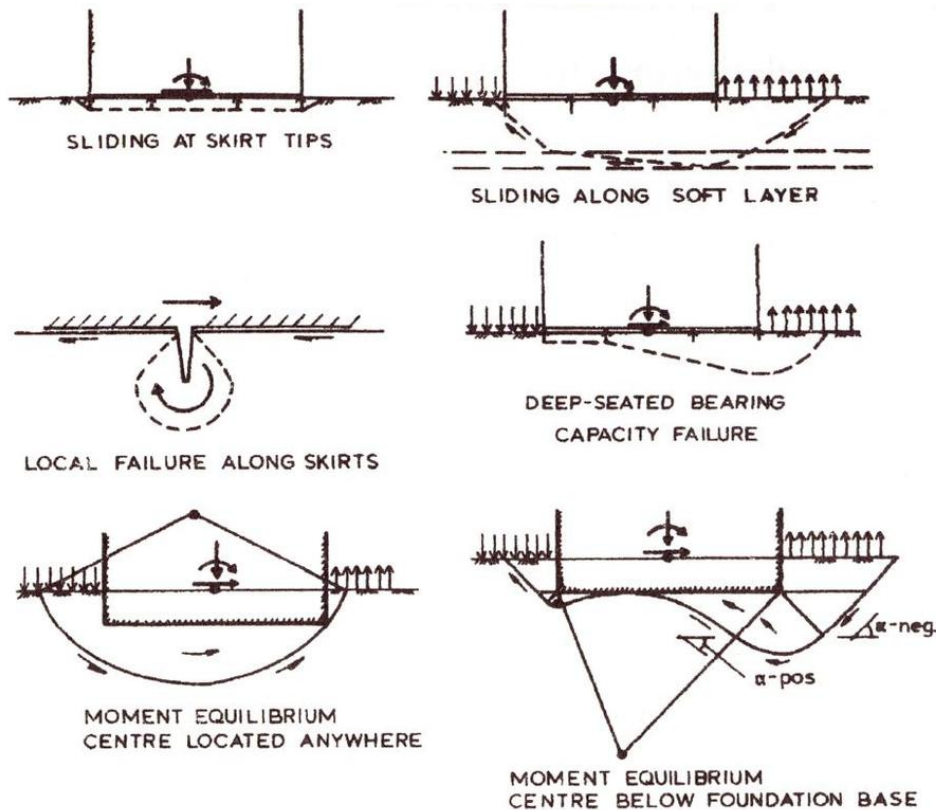


Figure 5.4: Possible failure modes for gravity-based foundations [22].

In the industry, many structural designs are based on the limit state design method. The limit state is defined as the structure's condition where it no longer meets the relevant design criteria. A few common limit states to consider are:

- **Ultimate Limit State (ULS)**
State corresponding to the ultimate capacity for carrying loads.
- **Serviceability Limit State (SLS)**
State corresponding to the ability for normal use.
- **Fatigue Limit State (FLS)**
State corresponding to failure due to cyclic loading.
- **Accidental Limit State (ALS)**
State corresponding to acceptable damage during an accident.

Based on practical experience, it was found that the ULS and SLS drive the structural design of GBFs. Therefore, for the preliminary design in this thesis, only these two limit states were analyzed using a simplified geotechnical analysis (subsection 5.3.3-5.3.4). Lastly, to ensure the manufacturability of this complex structure (reinforced concrete GBF), a simple geometrical check for the cone slope angle had to be executed in subsection 5.3.5.

5.3.1. Natural frequency analysis

As resonance can be critical for the structural dynamics of a structure, a natural frequency analysis was performed to ensure that the support structure (GBF including the WT tower) would not be excited by the WT (1P & 3P). Since the lowest eigenmodes contain the largest amounts of energy and would most likely result in the highest loads, only the first natural frequency of the support structure is examined. Therefore, this first natural frequency was calculated.

The first natural frequency of the GBF (including tower and WT mass) was calculated in ROSAP using a simplified structural model. First, the GBF was divided into a large number of conical beam elements to increase the detail of the structural model. For each element, the height, outer diameter, wall thickness, concrete mass, and ballast mass were calculated in Python. Next, the respective submerged density was used for both the concrete and ballast below the SWL. This is based on Archimedes' principle and is essentially the material's density deducted from the seawater density.

Subsequently, a natural frequency analysis based on the free vibration (i.e. no applied loads) of the structural model was performed in ROSAP. This analysis was based on the linear structural model and automatically calculated the stiffness and damping for each element. Eventually, the natural frequencies of each modal shape were computed in an iterative process.

An eigenmode displays the deformed shape when the structure is excited at the corresponding natural frequency f . In Figure 5.5, the first four eigenmodes for the fore-aft bending moments based on the initial design (including tower and RNA mass) are provided. It must be noted that these modal shapes have been scaled by a factor of 20 to increase the visibility of the actual small displacements.

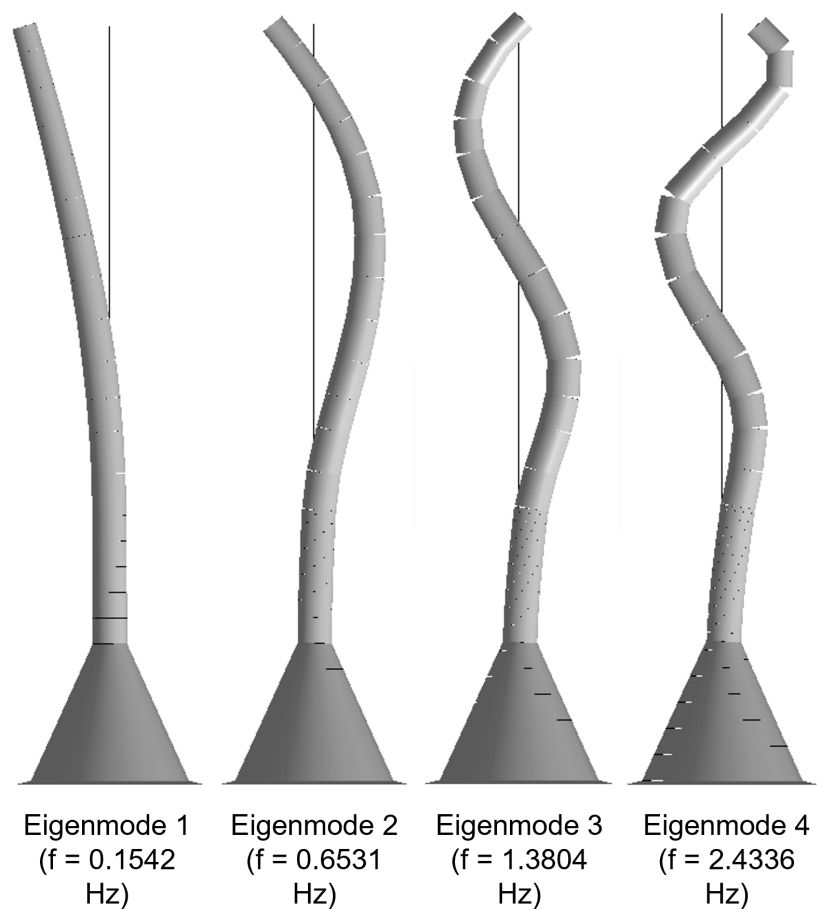


Figure 5.5: Scaled eigenmodes 1-4 for fore-aft bending moments of the initial GBF design, including the tower, where the RNA is considered a point mass at hub height. The eigenmodes are scaled by 10 to make the small displacements clearer, and the dashed lines display the initial positions.

Lastly, this analysis aims to check if the computed first fore-aft bending moment natural frequency f_1 of the structure will be excited by the WT harmonics. This can be resonance due to the rotational speed (1P) or the blade passing frequency (3P). For the initial design configuration, f_1 was equal to 0.154 Hz, which was inside the allowable frequency range of the WT. This is visually shown in Figure 5.6, where the GBF falls right in the desirable soft-stiff region.

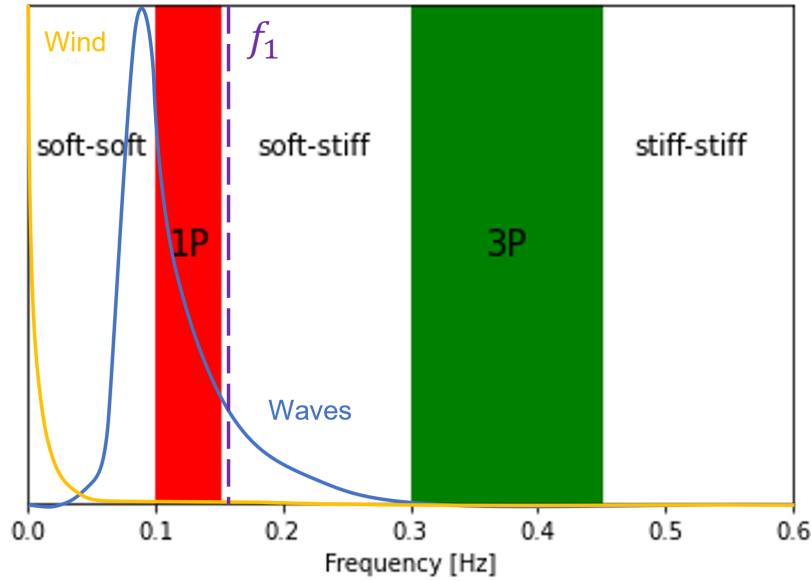


Figure 5.6: Natural frequency domain, where 1P is the rotor frequency, 3P is the blade passing frequency, and f_1 is the first natural frequency of 0.154 Hz of the initial gravity-based foundation design (including tower and RNA).

5.3.2. Design load cases

A design load case represents a loading condition that could occur during a structure's lifetime. It depends on the severity of the environment (e.g. extreme waves or wind) and design situation (e.g. power production, shutdown or parked). Furthermore, each design load case can be only relevant for specific limit states (e.g. ULS, SLS, FLS or ALS).

The multi-directionality of wind and waves may influence the magnitude of the total loads acting on the support structure. Therefore, a worst-case scenario may be assumed where wind and wave directions are aligned for extreme design load cases. Furthermore, it is somewhat unrealistic to assume that extreme waves and wind speeds would occur simultaneously because this would result in overly conservative solutions.

To achieve a complete design basis in the industry, the wind turbine is analyzed by simulating dozens of load cases. This ensures that the turbine can withstand these various loading conditions while considering a safety margin. Nevertheless, this does not fit within the scope of this thesis, and therefore based on practical experience from Rambøll's experts, the following two extreme design load cases were proposed in subsection 5.3.2. Here, it can be seen that LC1 is based on extreme wind load conditions and moderate sea conditions, whereas LC2 has extreme wave load conditions and moderate wind conditions. In both load cases, the WT would be in a parked mode due to the severity of the environmental conditions. Lastly, a potential preliminary GBF design is only obtained when the design configuration passes all the structural design checks for both load cases.

Table 5.9: Extreme design load cases.

Design load case	Wave loads	Wind loads
	[%]	[%]
LC1: Extreme wind	60	100
LC2: Extreme waves	100	50

5.3.3. Ultimate Limit State

The ULS is the condition that ensures safety (e.g. maintaining stability, static equilibrium, and avoiding fractures, deformations, and formation of mechanisms). For ULS, a preliminary design check for concrete offshore GBFs is based on the following parameters:

- Bearing capacity, which ensures that the soil does not collapse due to the structure's weight.
- Sliding capacity, which guarantees that the structure will not start sliding.
- Tipping capacity, which makes sure that the structure will not tip over.

The geotechnical calculations for all three capacity checks were based on a combination of DNV-RP-C212 [22] and DNV-Risø [64], while using the soil conditions from Table 5.2. Each capacity was checked with a utilization ratio, which displays how much of the available capacity is used by the structure. A ratio above 100% would mean that the available capacity is insufficient, and therefore the foundation stability cannot be ensured; i.e. to achieve stability, the ratio needs to be below 100%.

Lastly, as mentioned before, the ULS uses a different partial safety factor for the environmental loads (wave and wind loading) and the permanent loads (total weight of the WT). The factor for the environmental loads is equal to 1.35 and is used for normal extreme conditions. Nonetheless, the permanent loads have a favourable factor of 0.9 since this load positively affects the foundation stability [20].

Bearing capacity check

The bearing capacity is the capability of the soil to withstand the loads from the foundation. The environmental and permanent loads from the WT that act on the foundation are combined into a resultant horizontal and vertical design force: H and V . Both H and V are the sums of the characteristic loads multiplied by their corresponding partial safety factor. Subsequently, these resultant forces are transferred to the soil through vertical contact pressure at the foundation-soil interface (mudline).

Due to the resulting overturning moment, it could produce an eccentricity e , between V and the centre line of the foundation. This is visually shown using a load centre (LC) in Figure 5.7. Furthermore, the eccentricity can be calculated using Equation 5.5, where $M_{y,char}$ and V_{char} are the characteristic overturning moment and characteristic resultant vertical design load.

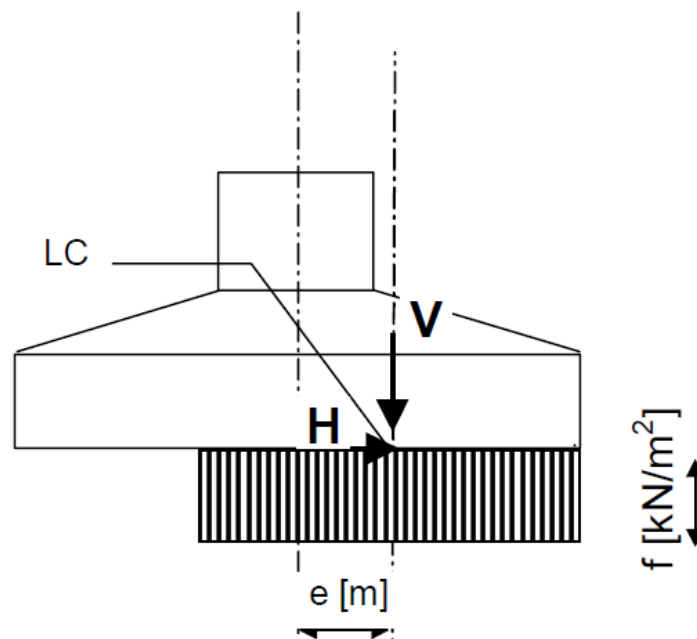


Figure 5.7: Representation of a gravity-based foundation at the foundation-soil interface under idealised conditions, where LC represents the load center, e is the eccentricity, H is the resultant horizontal design force, and V is the resultant vertical design force. Adapted from DNV-Risø [64].

$$e = \frac{M_{y,char}}{V_{char}} \quad (5.5)$$

To ensure that the geometrical centre and the load centre LC are aligned, it is essential to use the effective foundation area A_{eff} . Since a GBF has a circular foundation area, the effective foundation area will have a pointed oval shape with a length l_e and width b_e . The circular effective foundation area A_{eff} was calculated using Equation 5.6, where R is the base radius, and shown in Figure 5.8.

$$A_{eff} = 2 \cdot \left[R^2 \cdot \arccos\left(\frac{e}{R}\right) - e \cdot \sqrt{R^2 - e^2} \right] \quad (5.6)$$

$$l_{eff} = \sqrt{A_{eff} \frac{l_e}{b_e}} \quad b_{eff} = \frac{l_{eff} b_e}{l_e}$$

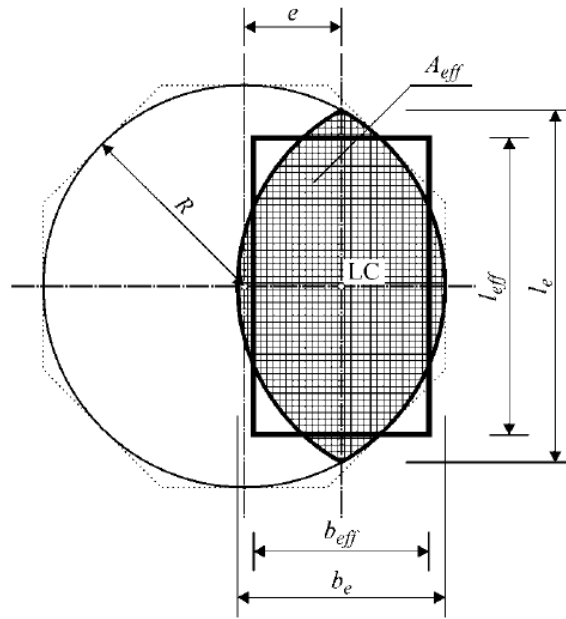


Figure 5.8: Effective foundation area for a circular gravity-based foundation with a radius R and an eccentricity e . The effective foundation area (pointed oval) with length l_e and width b_e can also be converted into a rectangle with length l_{eff} and width b_{eff} [64].

As seen in Figure 5.8, the effective foundation area can also be represented by a rectangle with an effective length l_{eff} and width b_{eff} . These values are calculated using:

$$l_{eff} = \sqrt{A_{eff} \frac{l_e}{b_e}} \quad \text{and} \quad b_{eff} = \frac{l_{eff} b_e}{l_e} \quad (5.7)$$

The wind loads on the WT generate a torque M_z , which was also transferred to the foundation. To take this into account, H was modified and a new resultant horizontal design force H' was obtained:

$$H' = \frac{2 \cdot M_z}{l_{eff}} + \sqrt{H^2 + \left(\frac{2 \cdot M_z}{l_{eff}} \right)^2} \quad (5.8)$$

As the soil was assumed to be nonconhesive, and therefore fully drained, the ultimate bearing capacity q_u for the GBF was calculated using:

$$q_u = \frac{1}{2} \gamma' b_{eff} N_\gamma s_\gamma i_\gamma + p'_0 N_q s_q i_q, \quad (5.9)$$

where:

- γ' = effective submerged unit weight of soil;
- b_{eff} = effective foundation width;
- p'_0 = effective overburden pressure at foundation-soil interface;
- N_γ, N_q = bearing capacity factors;
- s_γ, s_q = shape factors;
- i_γ, i_q = load inclination factors.

The various factors were calculated using the following equations:

$$\begin{aligned} N_\gamma &= \frac{3}{2} \cdot (N_q - 1) \cdot \tan \phi_d & N_q &= e^{\pi \tan \phi_d} \cdot \frac{1 + \sin \phi_d}{1 - \sin \phi_d} \\ s_\gamma &= 1 - 0.4 \cdot \frac{b_{eff}}{l_{eff}} & s_q &= 1 + 0.2 \cdot \frac{b_{eff}}{l_{eff}} \\ i_\gamma &= i_q^2 & i_q &= \left(1 - \frac{H_d}{V_d + A_{eff} \cdot c_d \cdot \cot \phi_d} \right)^2 \end{aligned} \quad (5.10)$$

It must be mentioned that the design friction angle ϕ_d is equal to the specified characteristic friction angle ϕ_c , multiplied by a safety factor of 1.15. Lastly, the utilization ratio for the bearing capacity check was determined as the ratio of the effective soil stress p_u over the ultimate bearing capacity q_u , where p_u is equal to V/A_{eff} :

$$\text{Bearing capacity utilization [\%]} = \frac{p_u}{q_u} \quad (5.11)$$

Sliding capacity check

The sliding capacity check guarantees that the GBF will not slide due to horizontal actions and is checked based on a simple condition:

$$H < V \tan \phi_d. \quad (5.12)$$

As previously mentioned, H and V are the resultant design loads, whereas ϕ_d is obtained by multiplying ϕ_c with a partial safety factor of 1.15. Hence, the utilization ratio for the sliding capacity check of a GBF on drained soil can be computed using:

$$\text{Sliding capacity utilization [\%]} = \frac{H}{V \tan \phi_d} \quad (5.13)$$

Tipping capacity check

The GBF transfers overturning moments about the seabed by a varying contact pressure over the foundation-soil interface. If the soil does not collapse due to the weight of the GBF (i.e. insufficient bearing capacity), it can be assumed that the tipping point would be on either edge of the base. By neglecting complex phenomena such as soil suction, the tipping capacity can be checked by a simple moment equilibrium around the edge of the base. The force diagram of the GBF on the seabed is displayed in Figure 5.9, where point A represents the tipping point, R_{base} is the base radius, M_{st} is the stabilizing moment caused by the vertical resultant design load V (total weight), and M_{dst} is the destabilizing moment due to the horizontal resultant design load H (environmental loads).

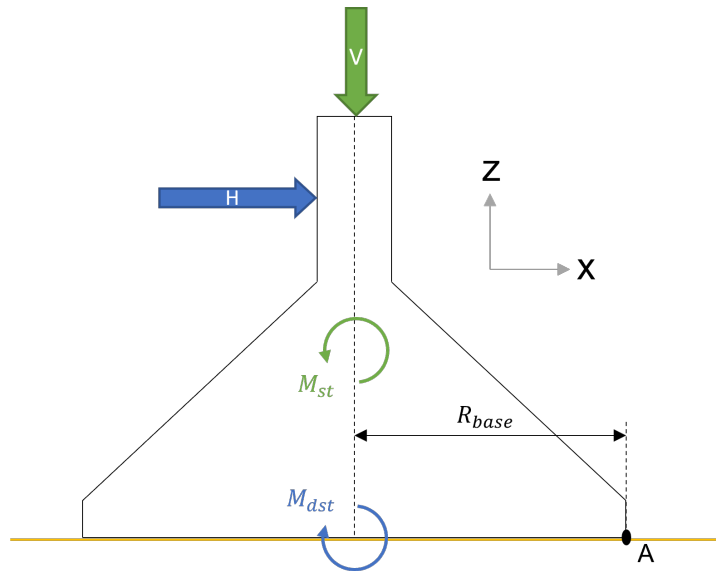


Figure 5.9: Force diagram of a gravity-based foundation on the seabed, where point A represents the tipping point, R_{base} is the base radius, M_{st} is the stabilizing moment caused by the horizontal resultant design load H , and M_{dst} is the destabilizing moment due to the vertical resultant design load V .

It can be seen that M_{st} can be calculated by multiplying V with the arm R_{base} . Contrarily, M_{dst} is obtained through the moment contribution of H , multiplied by another safety factor of 1.50. This overturning safety factor is based on common practice for concrete structures. Lastly, the tipping capacity utilization ratio can be calculated using:

$$\text{Tipping capacity utilization [\%]} = \frac{M_{dst}}{M_{st}} \quad (5.14)$$

5.3.4. Serviceability Limit State

Serviceability limit states (SLS) correspond to the criteria applicable to normal use or durability. As mentioned in subsection 5.2.1, the SLS loads are obtained by multiplying the environmental loads (waves and wind) with a partial safety factor of 0.65. The permanent loads (weight of RNA and tower) For the preliminary design of a GBF, the SLS only consist of a full-contact check. This check ensures that the bottom of the structure remains in full contact (with an allowed tolerance) with the soil. In other words, it prevents the occurrence of excessive gapping between the structure and the soil due to negative contact pressure. This excessive gapping can induce erosion of the soil under the foundation, which could result in a permanent critical inclination [65].

This full-contact check is based on the ratio of the actual eccentricity e and the allowable eccentricity e_{max} . The actual eccentricity e is the ratio between the total overturning moment M_{SLS} (the bending moment at mudline) and the normal force N_{SLS} (total weight of the support structure and RNA). On the other hand, the allowable eccentricity e_{max} is based on the core diameter of the structure, which is a sectional property of the circular geometry. For solid circular sections like the GBF's base plate, the core diameter equals 1/4 of the base diameter D_{base} . Therefore, to avoid the tension of the base but instead have only complete compressive stress, the eccentricity needs to be smaller or equal to $D_{base}/8$. Additionally, GBFs transfer overturning moments by varying the contact pressure over the foundation-soil interface. Therefore, this contact pressure may never become negative during extreme loading to avoid gapping. This is all based on fundamentals in the field of strength of materials as described in [66]. Therefore, to summarize, the full-contact check is executed using the following formula:

$$\text{Full-contact utilization [\%]} = \frac{e}{e_{max}}, \quad (5.15)$$

where

$$e = \frac{M_{SLS}}{N_{SLS}} \quad \text{and} \quad e_{max} = \frac{D_{base}}{8}. \quad (5.16)$$

There is an additional check for extreme eccentric loading. However, since the base diameter for GBFs is quite large, this type of structure is often not an issue. Therefore, this check was not executed as it was regarded as negligible.

5.3.5. Manufacturability of the structure

Another important aspect of the design is manufacturability. The complexity and size of a concrete structure determine the manufacturing costs. Within industry practice, it is common not to exceed a cone slope angle θ of 45 degrees for concrete structures. This is the angle between the diagonal and the vertical of the cone, which can be seen in Figure 5.10. As seen in Equation 5.17, θ is derived using trigonometry and the known dimensions of the top cylinder radius R_{top} , the cone bottom radius R_{bot} , and the cone height h_{cone} . If the limit of 45 degrees is exceeded, it will affect the reinforced concrete mechanics, as it will introduce a critical weak point located at the transition point. Although, in theory, it is possible to create a GBF with a cone slope angle close to the limit, it is not recommended due to its complexity. Lastly, as mentioned earlier, the complexity will increase manufacturing costs; therefore, a minimal cone slope is preferred.

$$\theta = \arctan \left(\frac{R_{bot} - R_{top}}{h_{cone}} \right) \quad (5.17)$$

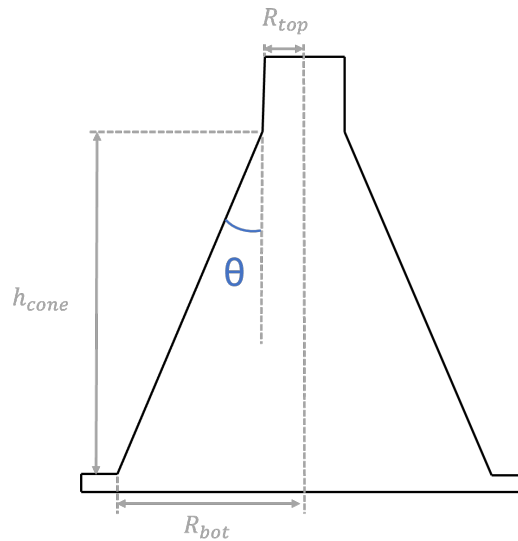


Figure 5.10: Representation of the cone slope angle θ for a gravity-based foundation, which is dependent on the cone top radius R_{top} , cone bottom radius R_{bot} , and the cone height h_{cone} .

5.4. Scour protection

The scour protection is not considered for the preliminary design of a GBF; therefore, it is not within the scope of this thesis. Nevertheless, it is a critical detail that is part of the secondary structure and is undoubtedly capable of influencing the final design. This is especially true for non-pile structures such as offshore GBFs. A possible protection measure against scour could be by placing sandbags or large rocks around the foundation on the seabed. In some cases, skirts are implemented in the GBF design to prevent scouring or erosion of the soil. When skirts are used, the base level (the foundation soil interface) is at the skirt tip level rather than the seabed.

5.5. Preliminary analysis of initial design

As seen in the results of the preliminary analysis in Table 5.10, the initial design with a ballast density of 2000 kg/m^3 , a base diameter of 45.0 m, and a cylinder-cone transition point at -15.0 m, meets all the design requirements. Additionally, the OrcaFlex model of this initial design is provided in Figure 5.11.

It is highly likely that there are superior designs, since only one design configuration has been examined. In chapter 6, the effect of various design parameters is investigated. Subsequently, depending on the optimization objectives, a few optimal preliminary designs are proposed.

Table 5.10: Results of the preliminary analysis for the initial configuration of the gravity-base foundation preliminary design. The green cells show if the design passed the specific check.

Load case	LC 1	LC 2
Ballast density [kg/m^3]	2000	2000
Base diameter [m]	45.0	45.0
Transition point [m]	-15.0	-15.0
Concrete volume [m ³]	3459	3459
Ballast volume [m ³]	14857	14857
Bearing cap. utiliz. [%]	40.6	80.4
Sliding cap. utiliz. [%]	43.2	67.8
Overturing cap. utiliz. [%]	25.5	20.1
Full contact utiliz. [%]	29.5	23.3
1st Nat. frequency [Hz]	0.154	0.154
Cone slope angle [deg]	24.9	24.9

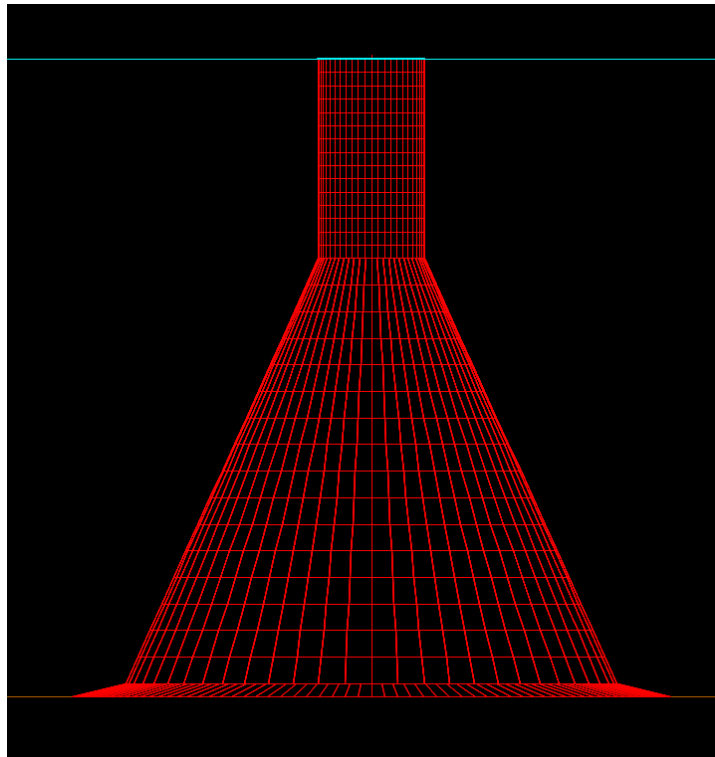


Figure 5.11: OrcaFlex model of the initial gravity-based foundation design.

6

Preliminary design based on sensitivity analysis

Any preliminary design is based on a few main parameters that influence the results. The values for these parameters are chosen carefully based on the design criteria and objectives to obtain an optimal design. For a concrete GBF, these parameters must be related to the weight and shape of the conical part. In this chapter, the effects of varying three essential design parameters are studied (ballast density, footprint, and cylinder-cone transition point).

The ballast density ρ_b influences the ballast weight, and therefore the post-installation foundation stability. On the other hand, the conical shape of the GBF is defined by the footprint (base diameter D_{base}) and the cone height (cylinder-cone transition height z_{trans}). Both parameters highly affect the structure's size and weight (pre-installation and post-installation), and hence are crucial for the costs associated with construction (e.g. required tools, materials and man hours), storage (e.g. yard capacity), transportation (e.g. towing to project location), and installation (e.g. heavy-lift vessels).

For each sensitivity analysis, the same reference GBF, reference WT, and environmental conditions as in chapter 5 have been used for all load cases (LC1 and LC2) mentioned in subsection 5.3.2. Additionally, in order to study the effect of the various design parameters, in each study all the other parameters are kept constant. Lastly, based on the results, a few suggestions for an optimal preliminary GBF design are provided in section 6.3.

Table 6.1: Design parameters for the sensitivity analyses and the corresponding reference values.

Parameter	Symbol	Value	Unit
Ballast density	ρ_b	2000	kg/m^3
Footprint	D_{base}	45	m
Cylinder-cone transition height	z_{trans}	-15	m

6.1. Sensitivity analysis of design parameters

6.1.1. Influence of ballast density

In this section the effect of varying the ballast density in 1500/2000/2500 kg/m^3 is analyzed. By adjusting the ballast density, the weight of the ballast inside the structure and, subsequently, the total weight of the structure is influenced. The ballast is added in the final steps of the installation procedure. Therefore it does not impact the required lifting capacity of the heavy-lift vessels. Nonetheless, it does affect the costs as an enormous amount of ballast is required to fill up the structure.

In Table 6.2, the results for the ballast density sensitivity analysis are given for the initial reference GBF (base diameter of 45.0 m and a cylinder-cone transition point located at 15.0 m below the SWL). Here, it can be seen that if a particular design check is passed for a given configuration, the cell has been given a green colour. Contrarily, if the particular design check is unmet, the cell is red. For the sensitivity analyses results of all preliminary design configurations, the reader is kindly referred to Appendix D.

Table 6.2: Ballast density sensitivity analysis results for the initial reference gravity-based foundation with a base diameter of 45.0 m and a cylinder-cone transition point located at -15.0 m.

Load case	LC 1			LC 2			Volume [m3]	
	1500	2000	2500	1500	2000	2500		
Ballast density [kg/m^3]	1500	2000	2500	1500	2000	2500		
Base diameter [m]	45.0	45.0	45.0	45.0	45.0	45.0		
Transition point [m]	-15.0	-15.0	-15.0	-15.0	-15.0	-15.0	Volume [m3]	
Bearing cap. utiliz. [%]	64.7	40.6	36.5	242.2	80.4	58.0	Concrete	3459
Sliding cap. utiliz. [%]	64.4	43.2	32.5	101.0	67.8	51.0	Ballast	14857
Overturning cap. utiliz. [%]	38.0	25.5	19.2	30.0	20.1	15.2		
Full contact utiliz. [%]	43.9	29.5	22.2	34.6	23.3	17.5	Cone slope	24.9
1st Nat. frequency [Hz]	0.184	0.154	0.134	0.184	0.154	0.134	[deg]	

From Table 6.2, it can be observed that this configuration is only valid when a ballast density of $2000 kg/m^3$ is applied. The design with a ballast density of $1500 kg/m^3$ will fail due to the insufficient bearing and sliding capacities, whereas the design with a ballast density of $2500 kg/m^3$ will have resonance induced by the rotor harmonics.

In Figure 6.1-6.3, the general influence of the ballast density on the bearing capacity utilization, sliding capacity utilization, and first natural frequency is described for the initial reference GBF design. The red lines define the limits for the utilization ratios (100%), and the minimum and maximum values for the first natural frequency (0.15 Hz and 0.35 Hz). Similar figures could be created for the overturning capacity and full contact utilizations; however, according to the results of all sensitivity analyses, they were found to be sufficient for any configuration.

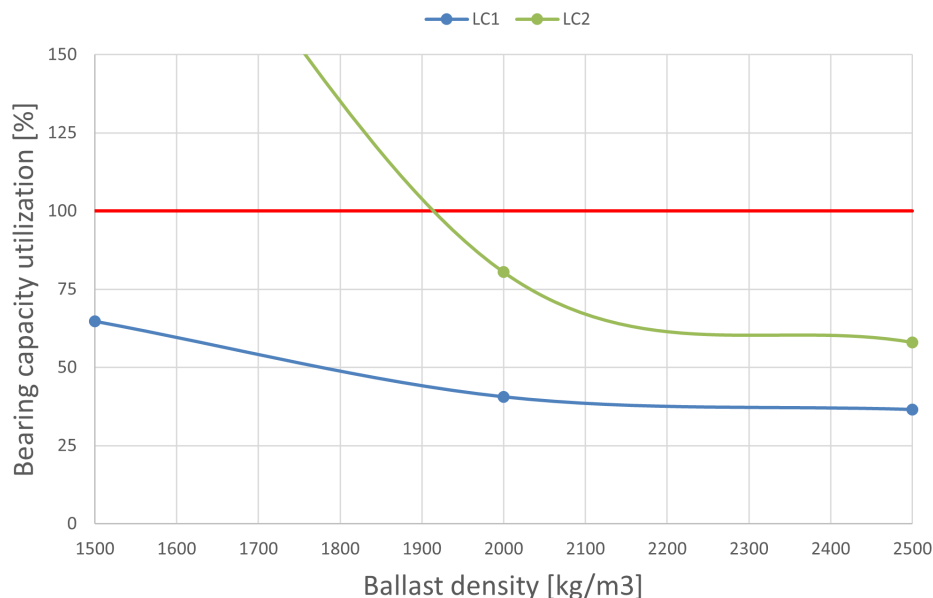


Figure 6.1: Dependency of the bearing capacity utilization ratio on the ballast density.

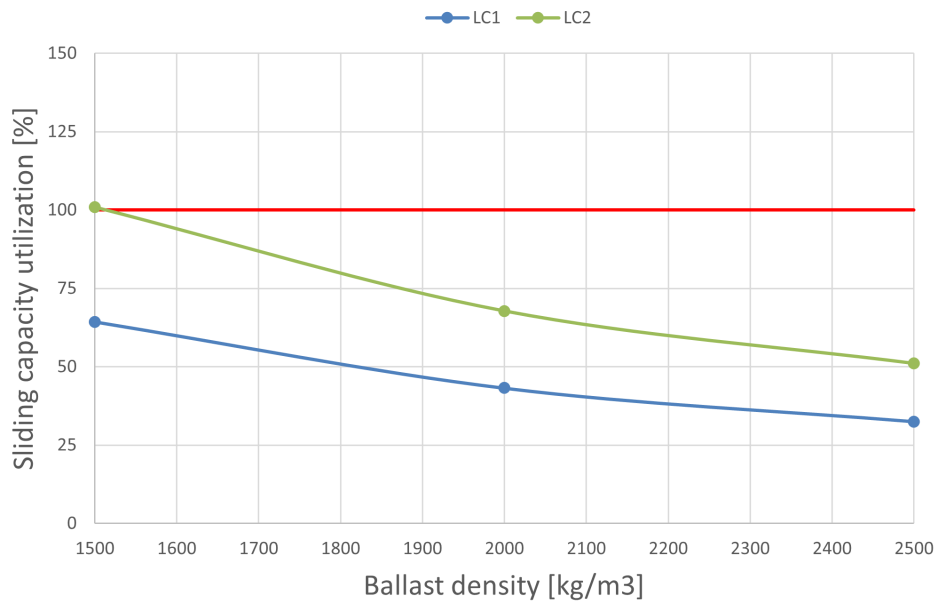


Figure 6.2: Dependency of the sliding capacity utilization ratio on the ballast density.

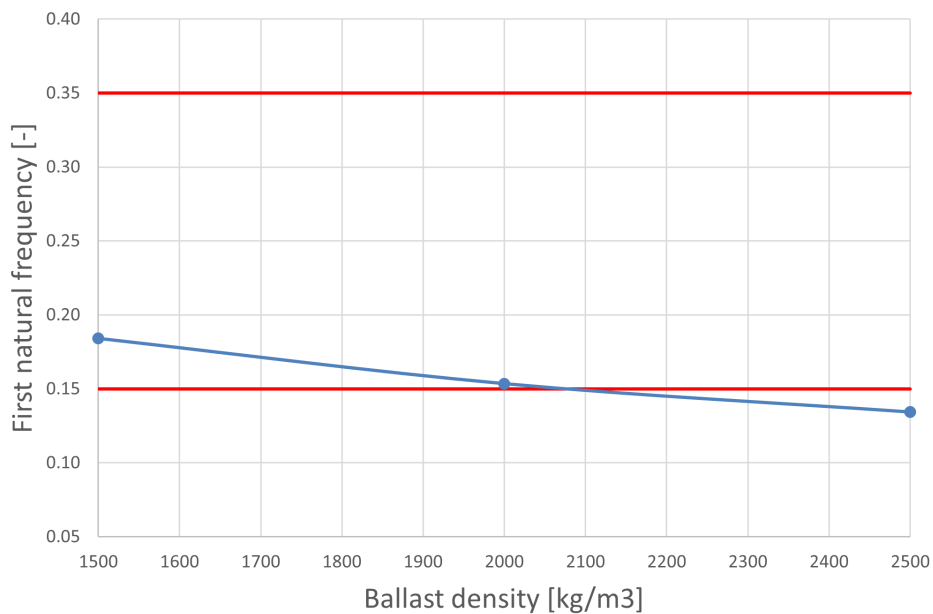


Figure 6.3: Dependency of the first natural frequency on the ballast density.

Based on the results, the following observations about the ballast density can be made:

- By increasing the ballast density, the total weight will increase, and subsequently, the overall geometrical eccentricity decreases, which benefits the design's stability. Therefore, the utilization ratios for the bearing capacity, sliding capacity, overturning capacity, and full contact check are reduced. It must be mentioned that this reduction seems to be exponential since the ratios decrease relatively more when the density changes from 1500 kg/m^3 to 2000 kg/m^3 in comparison with 2000 kg/m^3 to 2500 kg/m^3 .

- By increasing the mass, the stiffness of the structure increases as well. Although both the mass and stiffness determine the first natural frequency of the structure, it can be seen that the natural frequency decreases linearly (0.184 Hz to 0.134 Hz) for increasing ballast density. Therefore, it is evident that the mass increases relatively more than the stiffness.
- As the ballast density does not change the structure's geometry; the cone slope angle remains unaffected. In other words, it only influences the installation costs, whereas the manufacturing and transportation costs are both unaffected.
- The foundation stability for all design configurations are limited by either the bearing capacity or the first natural frequency.

6.1.2. Influence of footprint

This section studied the effect of varying the base diameter D_{base} in 35/40/45/50/55 m. This adjustment impacts the total weight of the structure and the hydrodynamic loads due to the changing shape of the cone. Subsequently, the footprint highly affects the required space for fabrication, transportation and installation. It must be emphasized that for all configurations, the cone top diameter remained 10 m, and the cone bottom diameter was kept 8 m smaller than the base diameter (27/32/37/42/47 m). For the sake of brevity, the analyses of only three structures (35/45/55 m) are given in Table 6.3-6.5. The results of all five configurations with varying base diameters have been provided in section D.1. In addition, the dependencies of the bearing capacity utilization ratios and the first natural frequency on the footprint are visualized in Figure 6.4 and Figure 6.5, where z_{trans} is -5.0 m and ρ_b is 2000 kg/m^3 .

Table 6.3: Sensitivity analysis results for the reference gravity-based foundation with a base diameter of 35.0 m, a cylinder-cone transition point located at -5.0 m, and varying ballast density (1500/2000/2500 kg/m^3).

Load case	LC 1			LC 2				
Ballast density [kg/m^3]	1500	2000	2500	1500	2000	2500		
Base diameter [m]	35.0	35.0	35.0	35.0	35.0	35.0		
Transition point [m]	-5.0	-5.0	-5.0	-5.0	-5.0	-5.0	Volume [m3]	
Bearing cap. utiliz. [%]	410.5	141.6	100.2	2159	340.3	182.0	Concrete	2679
Sliding cap. utiliz. [%]	69.3	47.6	36.3	107.0	73.7	56.2	Ballast	10857
Overturning cap. utiliz. [%]	84.0	57.8	44.1	85.8	59.1	45.1		
Full contact utiliz. [%]	97.1	66.8	51.0	99.2	68.3	52.1	Cone slope	13.0
1st Nat. frequency [Hz]	0.182	0.151	0.132	0.182	0.151	0.132	[deg]	

Table 6.4: Sensitivity analysis results for the reference gravity-based foundation with a base diameter of 45.0 m, a cylinder-cone transition point located at -5.0 m, and varying ballast density (1500/2000/2500 kg/m^3).

Load case	LC 1			LC 2				
Ballast density [kg/m^3]	1500	2000	2500	1500	2000	2500		
Base diameter [m]	45.0	45.0	45.0	45.0	45.0	45.0		
Transition point [m]	-5.0	-5.0	-5.0	-5.0	-5.0	-5.0	Volume [m3]	
Bearing cap. utiliz. [%]	118.0	58.5	49.3	886.9	150.4	91.4	Concrete	3687
Sliding cap. utiliz. [%]	73.3	47.6	35.3	116.6	75.8	56.2	Ballast	18653
Overturning cap. utiliz. [%]	46.1	30.0	22.2	47.8	31.1	23.0		
Full contact utiliz. [%]	53.3	34.7	25.7	55.2	35.9	26.6	Cone slope	19.3
1st Nat. frequency [Hz]	0.161	0.128	0.109	0.161	0.128	0.109	[deg]	

Table 6.5: Sensitivity analysis results for the reference gravity-based foundation with a base diameter of 55.0 m, a cylinder-cone transition point located at -5.0 m, and varying ballast density (1500/2000/2500 kg/m³).

Load case	LC 1			LC 2			Volume [m3]	
	1500	2000	2500	1500	2000	2500		
Ballast density [kg/m ³]	1500	2000	2500	1500	2000	2500		
Base diameter [m]	55.0	55.0	55.0	55.0	55.0	55.0		
Transition point [m]	-5.0	-5.0	-5.0	-5.0	-5.0	-5.0		
Bearing cap. utiliz. [%]	62.6	35.4	32.4	538.2	89.2	58.3	Concrete	4852
Sliding cap. utiliz. [%]	74.7	46.8	34.0	120.6	75.5	55.0	Ballast	28721
Overturing cap. utiliz. [%]	23.1	14.4	10.5	21.2	13.3	9.7		
Full contact utiliz. [%]	26.7	16.7	12.1	24.5	15.4	11.2	Cone slope	25.3
1st Nat. frequency [Hz]	0.143	0.110	0.093	0.143	0.110	0.093	[deg]	

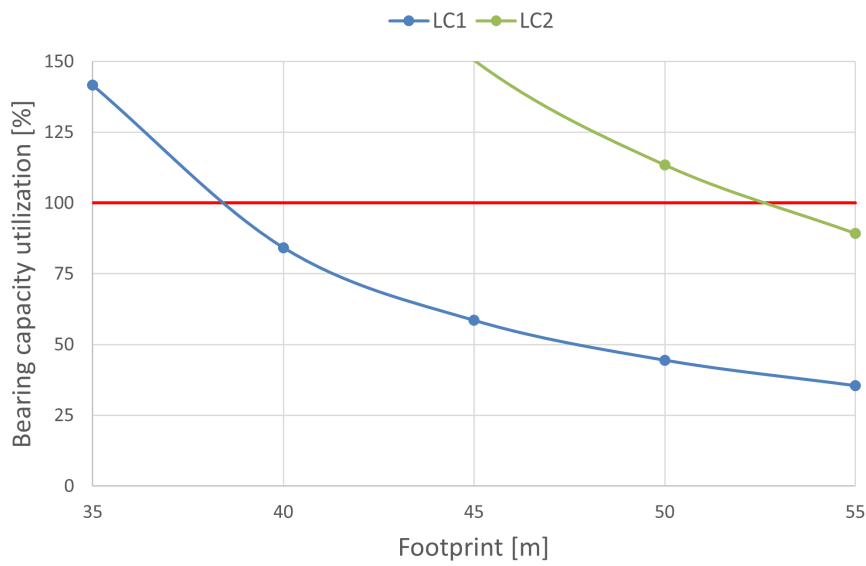


Figure 6.4: Dependency of the bearing capacity utilization ratio on the footprint/base diameter.

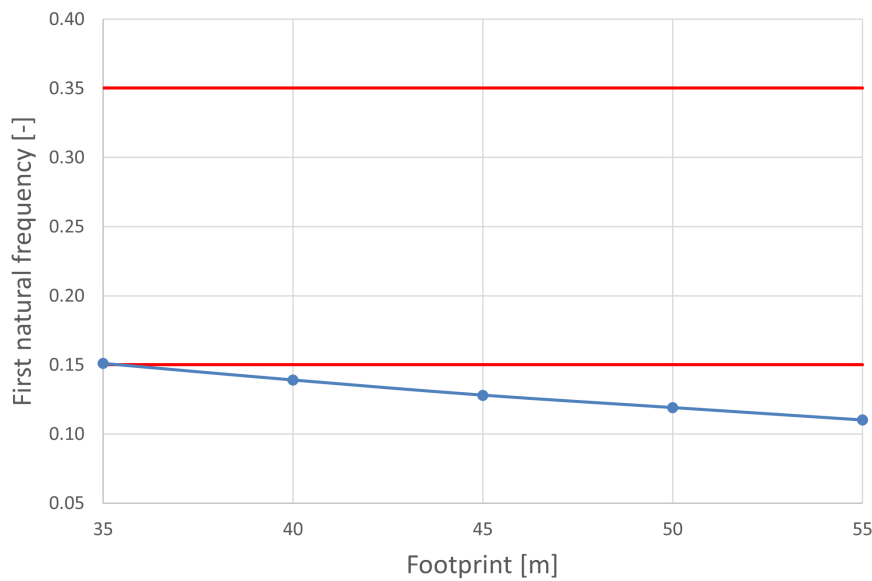


Figure 6.5: Dependency of the first natural frequency on the footprint/base diameter.

According to this analysis, the following conclusions regarding the influence of the footprint have been drawn:

- By increasing the base diameter, mainly the bottom part of the cone becomes larger. This results in larger hydrodynamic loads, where the relative increase for the base shear is far more significant than for the overturning moment. Even though the loads become more significant, the increased weight produces a more stable design since the required bearing capacity, sliding capacity, overturning capacity, and full contact decrease. It is noteworthy that the bearing capacity is significantly affected, whereas the sliding capacity is not as highly influenced.
- As previously mentioned, a larger base diameter results in a bigger cone and increases the structure's total weight and stiffness. However, the weight affects the structure more than the stiffness, so the first natural frequency declines.
- Both the volume of concrete is affected by the base diameter, as they both increase for a rising base diameter. It must be mentioned that the ballast volume increases relatively more than the concrete volume.
- For a valuable preliminary design, the optimal combination between the footprint and cone height is essential. As seen from the trend lines, merely adjusting the base diameter is insufficient and results in a lacking bearing capacity, sliding capacity, or an unacceptable first natural frequency.
- Lastly, the cone slope angle is highly dependent on the base diameter, considering that by increasing the base diameter, the cone slope also increases. Nevertheless, if this value stays below 45 degrees it will not cause any problems regarding reinforced concrete mechanics or complex manufacturing.

6.1.3. Influence of cone height

This section examines the influence of the cone height by varying the transition height between the cylinder and the cone z_{trans} at -5/-10/-15/-20/-25/-30 m (relative to the SWL). Similarly to the footprint, this parameter influences the structure's total weight and the hydrodynamic loads due to the adjusted shape of the cone. It must be emphasized that the cone top diameter (10 m), cone bottom diameter (37 m), and base diameter (45 m) remained unchanged for all configurations.

In Table 6.6-6.8, the results are provided for the designs with a transition point of -5/-15/-30 m. For the complete results of all six configurations, the reader is kindly referred to section D.2. Furthermore, the relation between the cone height with the bearing capacity utilization ratio and the first natural frequency are displayed in Figure 6.6 and Figure 6.7, where D_{base} is -45.0 m and ρ_b is 2000 kg/m^3 .

Table 6.6: Sensitivity analysis results for the reference gravity-based foundation with a cylinder-cone transition point located at -5.0 m, a base diameter of 45.0 m, and varying ballast density (1500/2000/2500 kg/m^3).

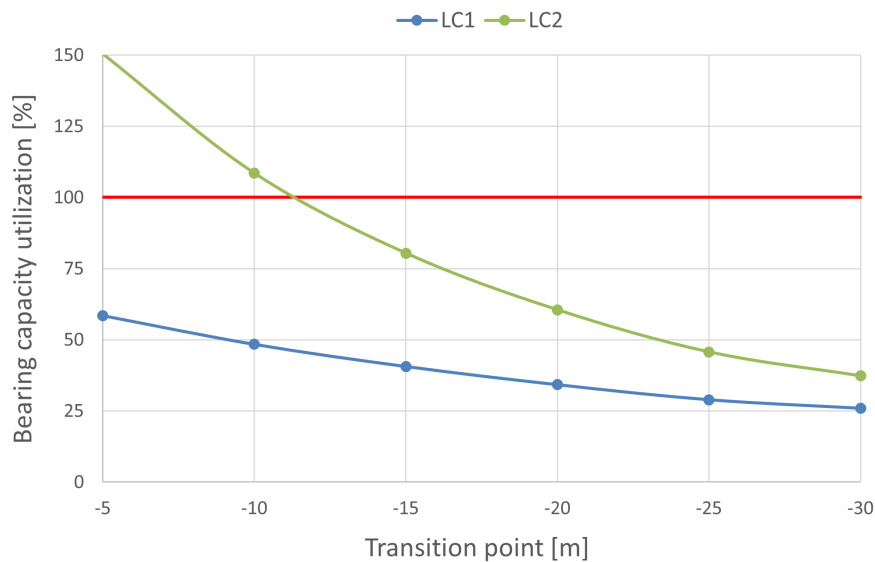
Load case	LC 1			LC 2			Volume [m3]	
	1500	2000	2500	1500	2000	2500		
Ballast density [kg/m^3]	1500	2000	2500	1500	2000	2500		
Base diameter [m]	45.0	45.0	45.0	45.0	45.0	45.0		
Transition point [m]	-5.0	-5.0	-5.0	-5.0	-5.0	-5.0	Volume [m3]	
Bearing cap. utiliz. [%]	118.0	58.5	49.3	886.9	150.4	91.4	Concrete	3687
Sliding cap. utiliz. [%]	73.3	47.6	35.3	116.6	75.8	56.2	Ballast	18653
Overturning cap. utiliz. [%]	46.1	30.0	22.2	47.8	31.1	23.0		
Full contact utiliz. [%]	53.3	34.7	25.7	55.2	35.9	26.6	Cone slope	19.3
1st Nat. frequency [Hz]	0.161	0.128	0.109	0.161	0.128	0.109	[deg]	

Table 6.7: Sensitivity analysis results for the reference gravity-based foundation with a cylinder-cone transition point located at -15.0 m, a base diameter of 45.0 m, and varying ballast density (1500/2000/2500 kg/m^3).

Load case	LC 1			LC 2			Volume [m3]	
	1500	2000	2500	1500	2000	2500		
Ballast density [kg/m^3]	1500	2000	2500	1500	2000	2500		
Base diameter [m]	45.0	45.0	45.0	45.0	45.0	45.0		
Transition point [m]	-15.0	-15.0	-15.0	-15.0	-15.0	-15.0	Volume [m3]	
Bearing cap. utiliz. [%]	64.7	40.6	36.5	242.2	80.4	58.0	Concrete	3459
Sliding cap. utiliz. [%]	64.4	43.2	32.5	101.0	67.8	51.0	Ballast	14857
Overturning cap. utiliz. [%]	38.0	25.5	19.2	30.0	20.1	15.2		
Full contact utiliz. [%]	43.9	29.5	22.2	34.6	23.3	17.5	Cone slope	24.9
1st Nat. frequency [Hz]	0.184	0.154	0.134	0.184	0.154	0.134	[deg]	

Table 6.8: Sensitivity analysis results for the reference gravity-based foundation with a cylinder-cone transition point located at -30.0 m, a base diameter of 45.0 m, and varying ballast density (1500/2000/2500 kg/m^3).

Load case	LC 1			LC 2			Volume [m3]	
	1500	2000	2500	1500	2000	2500		
Ballast density [kg/m^3]	1500	2000	2500	1500	2000	2500		
Base diameter [m]	45.0	45.0	45.0	45.0	45.0	45.0		
Transition point [m]	-30.0	-30.0	-30.0	-30.0	-30.0	-30.0	Volume [m3]	
Bearing cap. utiliz. [%]	33.9	25.9	24.3	61.3	37.3	31.6	Concrete	3117
Sliding cap. utiliz. [%]	51.2	37.0	28.9	77.3	55.8	43.7	Ballast	9163
Overturning cap. utiliz. [%]	38.6	27.9	21.8	21.9	15.8	12.4		
Full contact utiliz. [%]	44.6	32.2	25.2	25.3	18.3	14.3	Cone slope	41.7
1st Nat. frequency [Hz]	0.223	0.211	0.201	0.223	0.211	0.201	[deg]	

**Figure 6.6:** Dependency of the bearing capacity utilization ratio on the cone height (cylinder-cone transition point).

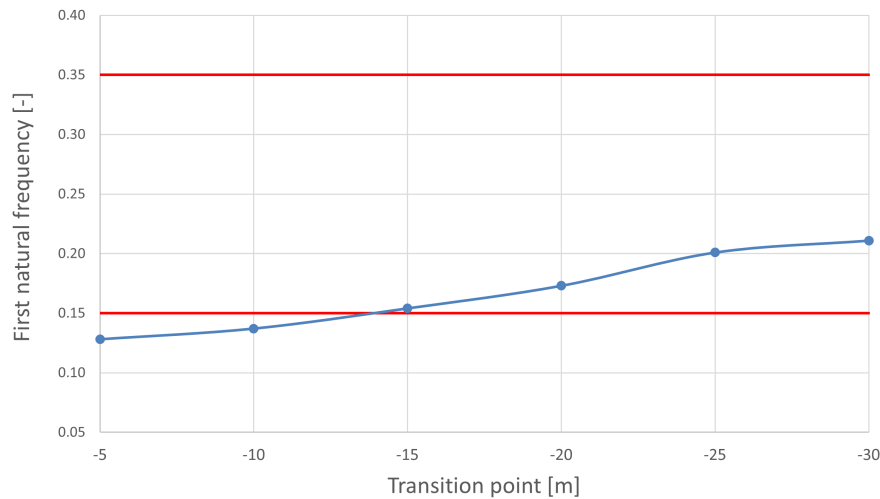


Figure 6.7: Dependency of the first natural frequency on the cone height (cylinder-cone transition point).

By analyzing the results, the following findings on the influence of the cylinder-cone transition point were made:

- By increasing the depth of the transition point, the conical section of the structure becomes smaller. Subsequently, the resulting hydrodynamic loads decrease, where the rate of decrease for the overturning moment is significantly greater than for the base shear. These smaller loads benefit the structure; therefore, the utilization ratio for the bearing capacity, sliding capacity, overturning capacity, and full contact decrease.
- The first natural frequency is linked to the transition point; if the depth of the transition point increases, the first natural frequency also increases.
- The required concrete volume, and to an even greater extent, the required ballast volume, both decrease when the transition point is lowered. This will reduce construction, transportation and installation costs.
- For a GBF, the foundation stability disturbance is predominantly determined by the wave loads. Therefore, the design load case with extreme waves (LC2) is the bottleneck for maximum load conditions.
- Lastly, the cone slope angle increases for larger depths of the transition point. To avoid local failures due to reinforced concrete mechanics, the angle must stay below the limit of 45 degrees.

6.2. Sensitivity analysis for optimization

For the preliminary design optimization, it is essential to study the dependencies between design parameters which are relevant for the optimization objective. In this section the relation between various parameters (bearing capacity utilization, first natural frequency, cone slope angle, and concrete weight,) and the shape of the GBF, which is determined by the base diameter D_{base} and the cylinder-cone transition point z_{trans} , are displayed using contour plots. The same dependencies can be displayed using three-dimensional plots (section D.4). The shown data is based on the sensitivity analysis results of 48 design configurations, which can be found in section D.3.

Based on the sensitivity analyses of the design parameters, the following conclusions can be made:

- If the adjustment of a parameter causes the total weight to rise, the decreased eccentricity will enhance the foundation stability. Additionally, this relative weight increase is always more significant than the stiffness increase; therefore, the first natural frequency decreases.
- By increasing the footprint or cone height, the conical section enlarges. The effect of the weight increase is considerably greater than the increased hydrodynamic loads, therefore it will positively influence the foundation stability.

- For a GBF, the foundation stability requirements are predominantly determined by the bearing capacity and wave loads. Therefore, the bottleneck is the bearing capacity utilization for the design load case with extreme waves (LC2), which are also the only stability check and load case that will be examined in this section.
- The cone slope angle increases by increasing the footprint or decreasing the cone height. A minimal cone slope angle is preferred since it will reduce the complexity and therefore the manufacturing costs. Nevertheless, if the limit of 45 degrees is unexceeded, local failures due to reinforced concrete mechanics will not occur.
- By continuously decreasing the cone height, the size of the cone and the total weight decreases. This is beneficial for the foundation stability, construction, transportation, and installation costs. Nonetheless, this is limited by the cone slope angle limit of 45 degrees and the maximum first natural frequency.

6.2.1. Influence of conical shape on the bearing capacity

The foundation stability of a GBF is generally limited by the bearing capacity utilization. To ensure that the soil does not collapse due to the structure's weight, the bearing capacity utilization ratio needs to remain below 100%. If maximum stability is desired, it would be beneficial to minimize this ratio. Nonetheless, to avoid overdesigning, a design near the limit of 100% is rather preferred.

In Figure 6.8, a contour plot is provided for LC2, which describes the dependency of the bearing capacity utilization ratio on the structural shape. Here, a ballast density of 2000 kg/m^3 and a reinforced concrete density of 2500 kg/m^3 have been used. The navy and dark green planes displays the only design configurations that result in an acceptable ratio below 100%, where the latter present the possible designs with a ratio of 50-100%. To remain in this favorable range, smaller footprints (35-40 m) should be combined with deep transition points (25-35 m below SWL), whereas larger footprints (40-45 m) with shallow transition points (15-25 m below SWL).

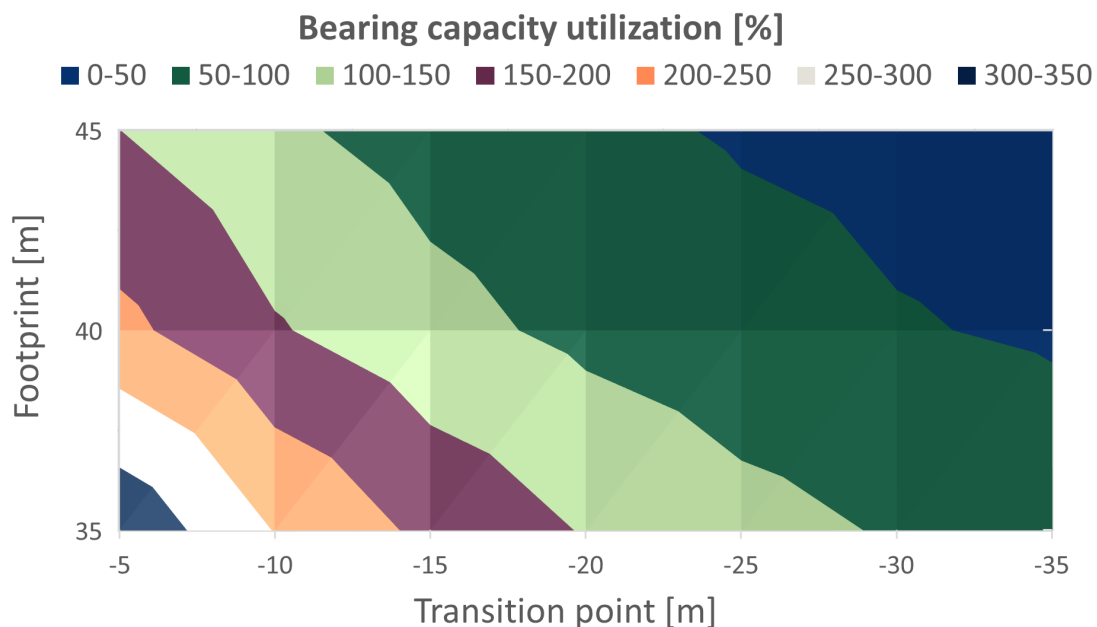


Figure 6.8: Contour plot of the dependency of the bearing capacity utilization ratio on the structure shape (cylinder-cone transition point and footprint). For the ballast and concrete material, a density of 2000 kg/m^3 and 2500 kg/m^3 were used, respectively. Values above the bearing capacity utilization ratio limit of 100% are result in foundation instability.

6.2.2. Influence of conical shape on the natural frequency

To maintain structural integrity, resonance due to the linear waves and critical rotor frequencies (1P and 3P) must be avoided. The conical shape of the GBF influences the first natural frequency since it determines the overall stiffness and mass of the system. For every project, the allowed first natural frequency range is provided by the WT manufacturer (0.15-0.35 Hz).

In Figure 6.9, the relation between the natural frequency and the cone' shape is described. For the ballast and concrete material, a density of 2000 kg/m^3 and 2500 kg/m^3 were used, respectively. It can be seen that this preliminary GBF design is only limited by the lower limit of 0.15 Hz, which generally only occurs for configurations with large footprints (>40 m) and shallow transition points (<-12.5 m). Therefore, to avoid excitations due to the rotor, the GBF should be designed with a base diameter smaller than 40 m and a transition point larger than 12.5 m below the SWL.

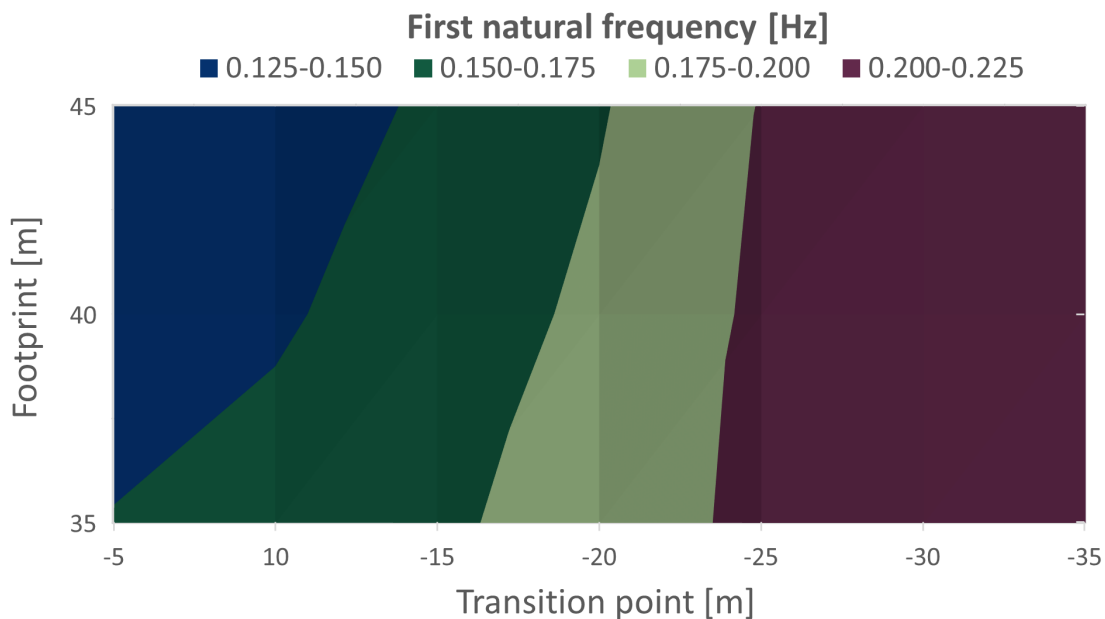


Figure 6.9: Contour plot of the dependency of the first natural frequency on the structure shape (cylinder-cone transition point and footprint). For the ballast and concrete material, a density of 2000 kg/m^3 and 2500 kg/m^3 were used, respectively. For the given reference wind turbine, all the values below the lower limit of the first natural frequency (0.15 Hz) are invalid since they would result in excitation due to the 1P (rotor) frequency.

6.2.3. Influence of conical shape on the cone slope angle

Based on the advice from concrete experts at Rambøll, the maximum limit for the cone slope angle is estimated to be 45 degrees. If this angle is exceeded, the structure will experience local failures near the cylinder-cone transition point due to reinforced concrete mechanics. Additionally, it will increase the manufacturing costs due to the higher complexity of the structure. Therefore, although a minimal cone slope angle is preferred, the exact cost-benefits per increased degree is unknown. The assumption is that this difference per degree is small and only becomes significant for large differences (e.g. more than 15 degrees). Nonetheless, a minimal cone slope angle will most likely result in an insufficient bearing capacity and a larger total weight, thus the optimal angle would rather be between 20-35 degrees.

In Figure 6.10, the connection between the cone slope angle and the structure shape is displayed using a contour plot. It can be generally observed that the cone slope angle limit of 45 degrees is exceeded for design configurations with large footprints (>45 m) and transition points (>30 m below SWL). Designs with a more convenient cone slope angle (20-35 degrees) are found for structures with:

- Small footprints (30-40 m) and a transition point smaller than 30 m below SWL;
- Large footprints (45-55 m) and a transition point smaller than 20 m below SWL.

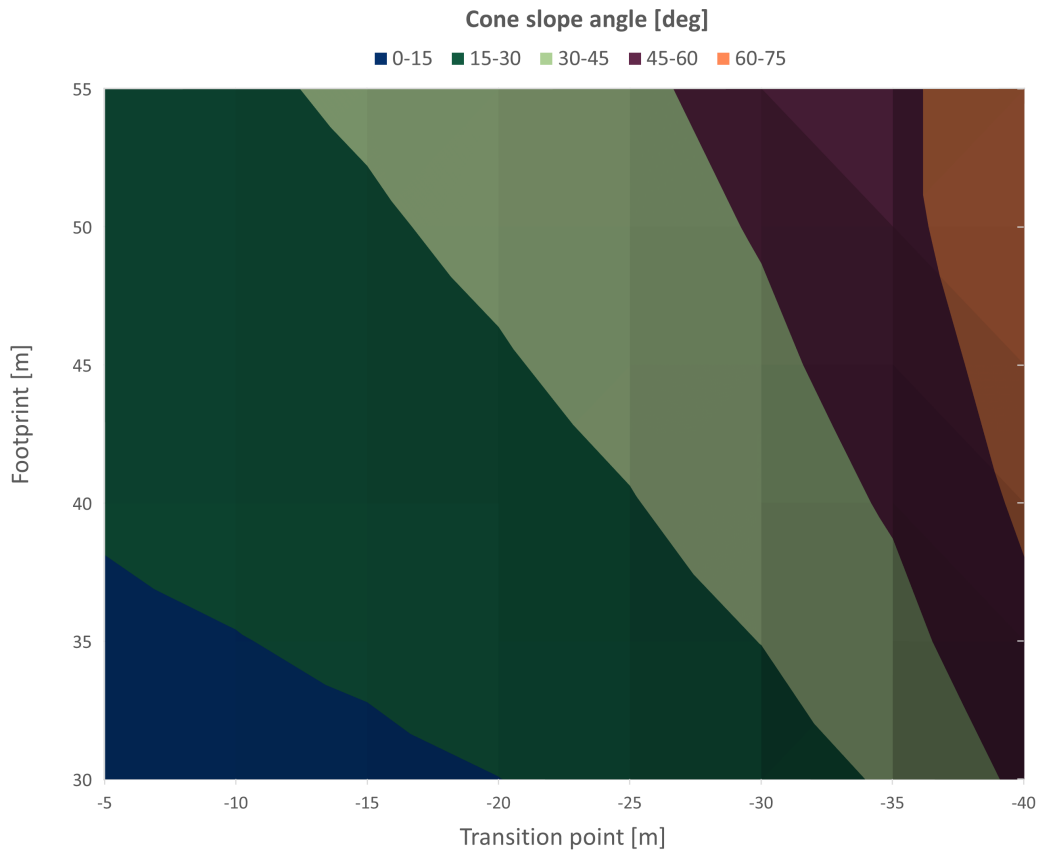


Figure 6.10: Contour plot of the dependency of the cone slope angle on the shape (cylinder-cone transition point and footprint). Values above the cone slope angle limit of 45 degrees are invalid since they would result in local weaknesses at the transition point due to reinforced concrete mechanics.

6.2.4. Influence of conical shape on the total concrete weight

Whereas the ballast weight has the highest contribution to the total installed weight, the required reinforced concrete weight is crucial for the pre-installation weight of the structure. It determines the requirements for the construction in the dock, transportation by towboats, and especially the installation using heavy-lift vessels. According to a 2020 market report of the global heavy lift vessel sector [67], in that year there were only nine heavy-lift vessels in the world that have the capacity to lift over more than 5000 tonnes. Although there are a lot of new vessels under construction or existing fleet being upgraded to meet the offshore heavy-lift demands [68], this remains a challenge for heavy foundations such as GBFs.

In Figure 6.11, a contour plot is displayed, which displays the dependency of the concrete weight on the structure shape. For the used reinforced concrete, a dry density of 2500 kg/m^3 was utilized. It can be noticed that the concrete weight is larger than 5000 tonnes for any design configuration, since it varies between 5500 and 9500 tonnes. Logically, if the conical section becomes bigger (large footprint and shallow transition point), the concrete weight increases. Therefore, to minimize the required weight, a minimal footprint and a maximal transition point is preferred. Although this does not result in conflicts regarding the cone slope angle and resonance, it will be limited by the bearing capacity utilization.

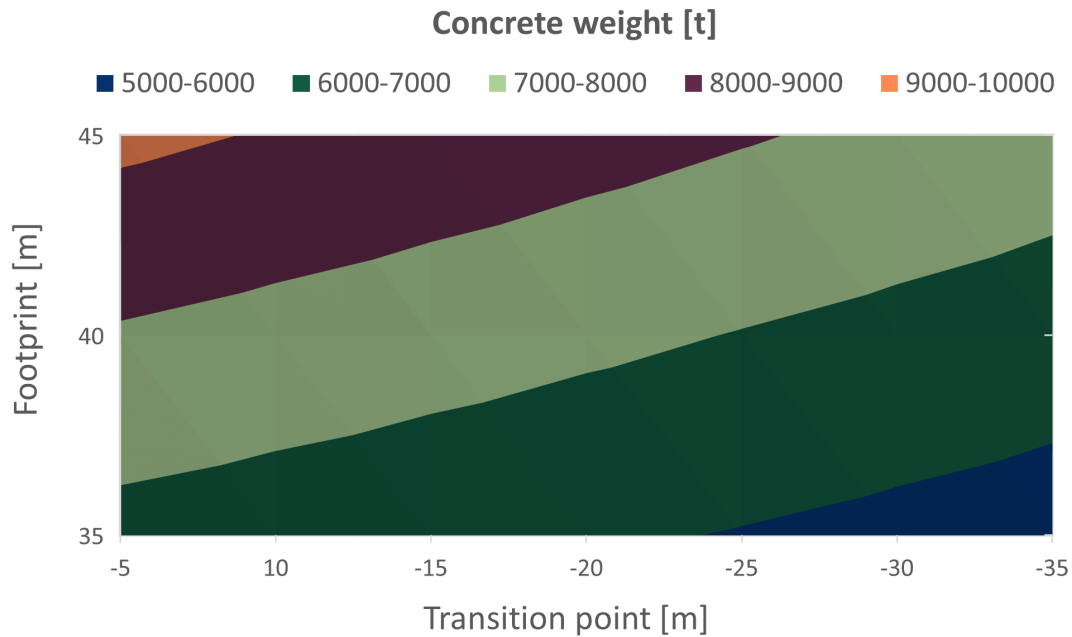


Figure 6.11: Contour plot of the dependency of the required concrete weight on the structure shape (cylinder-cone transition point and footprint). The used reinforced concrete has a density of 2500 kg/m^3 .

6.3. Optimal preliminary design based on objectives

Depending on the optimization objectives, there can be multiple optimal designs. For a GBF, these objectives are often related to weight, costs or both. For example, the amount of required material is directly related to material costs, whereas the complexity of the structure impacts the manufacturing costs. Additionally, the objectives change during the various phases (construction, transportation, installation, and operation). In the pre-installation phase, one of the biggest concerns with heavy offshore structures is the maximum lifting capacity and availability of modern installation vessels. Post-installation, the ballast material predominantly determines the weight, and hence, the bearing capacity of the structure.

This section gives multiple suggestions for an optimal preliminary design based on the chosen objectives. There are many more objectives that have not been considered within this thesis, e.g. size limitations for yard capacity, maximum lifting height of the cranes, or minimizing total costs. Nonetheless, based on discussion with industry experts from Rambøll, the following optimization objectives were chosen:

- Minimizing the concrete volume as it determines the pre-installation weight, which is limited by the capacity and availability of heavy-lift vessels.
- Using the ballast density of 2000 kg/m^3 , it is most commonly used and, therefore, cheaper. Furthermore, it has the largest contribution to the post-installation weight of the structure.
- Minimizing the cone slope (< 20 degrees) to lower the manufacturing costs due to the complexity of the structure. This does however not taken into account the increased material costs for both the concrete and the ballast material.
- A balance between these previously mentioned objectives, since an actual design is multi-objective and does not have only one optimized parameter.

6.3.1. Minimal concrete material and cheapest ballast material

The used amount of concrete highly influences the dry weight and, therefore, the material costs of the structure. In general, concrete is more expensive than ballast. Thus it would be sensible to focus on minimizing the concrete volume rather than the ballast volume. Additionally, as mentioned before, the transportation and installation capacity and costs are determined by the total dry weight of the structure. Generally, the weight of concrete is eight times larger than the weight of steel. Most installation vessels are focused on installing steel structures (e.g. monopiles/jackets) and are not used to the enormous weight of concrete GBFs. As a result, there are currently only a few operating heavy-lift vessels with the required lifting capacity.

Furthermore, different types of ballast are being used in the industry, and each has a different price. In the sensitivity analysis (subsection 6.1.1), three different ballast densities ($1500/2000/2500 \text{ kg/m}^3$) were compared. However, they do not all represent the same type of ballast. Based on discussions with industry experts from Rambøll, it was discovered that a ballast density of 2000 kg/m^3 corresponds to a commonly used ballast type, which also has the lowest cost per volume. Therefore, this section provides a potential optimal preliminary design, which has a minimal amount of concrete material and utilizes the cheapest ballast material.

To find the optimal design (in terms of minimal concrete volume), various configurations (based on experience gained from section 6.1) were analyzed. The results of the final design are shown in Table 6.9, whereas a graphical representation is given in Figure 6.12

This optimal design has a ballast density of 2000 kg/m^3 , a base diameter of 35.0 m, and a cylinder-cone transition point of -35.0 m below the SWL. Based on the results, it can be concluded that this configuration meets all the requirements regarding bearing capacity, sliding capacity, overturning capacity, full contact, first natural frequency, and cone slope angle. Moreover, in comparison with all the other configurations found in section D.3, it requires the least amount of both concrete (2231 m^3) and ballast (4888 m^3).

Table 6.9: Sensitivity analysis results of a preliminary design optimized for minimal concrete volume, where the base diameter is 35 m, the cylinder-cone transition point is located at -35.0 m, and the ballast density is varied ($1500/2000/2500 \text{ kg/m}^3$).

Load case	LC 1			LC 2			Volume [m3]	
	1500	2000	2500	1500	2000	2500		
Ballast density [kg/m^3]	1500	2000	2500	1500	2000	2500		
Base diameter [m]	35.0	35.0	35.0	35.0	35.0	35.0		
Transition point [m]	-35.0	-35.0	-35.0	-35.0	-35.0	-35.0	Volume [m3]	
Bearing cap. utiliz [%]	134.3	75.1	58.4	135.6	79.5	62.3	Concrete	2231
Sliding cap. utiliz [%]	48.6	37.6	30.6	68.9	53.4	43.6	Ballast	4888
Overturning cap. utiliz [%]	81.0	62.8	51.3	58.0	45.0	36.7		
Full contact utiliz. [%]	93.6	72.6	59.3	67.0	52.0	42.5	Cone slope	40.1
1st Nat. frequency [Hz]	0.225	0.217	0.208	0.225	0.217	0.208	[deg]	

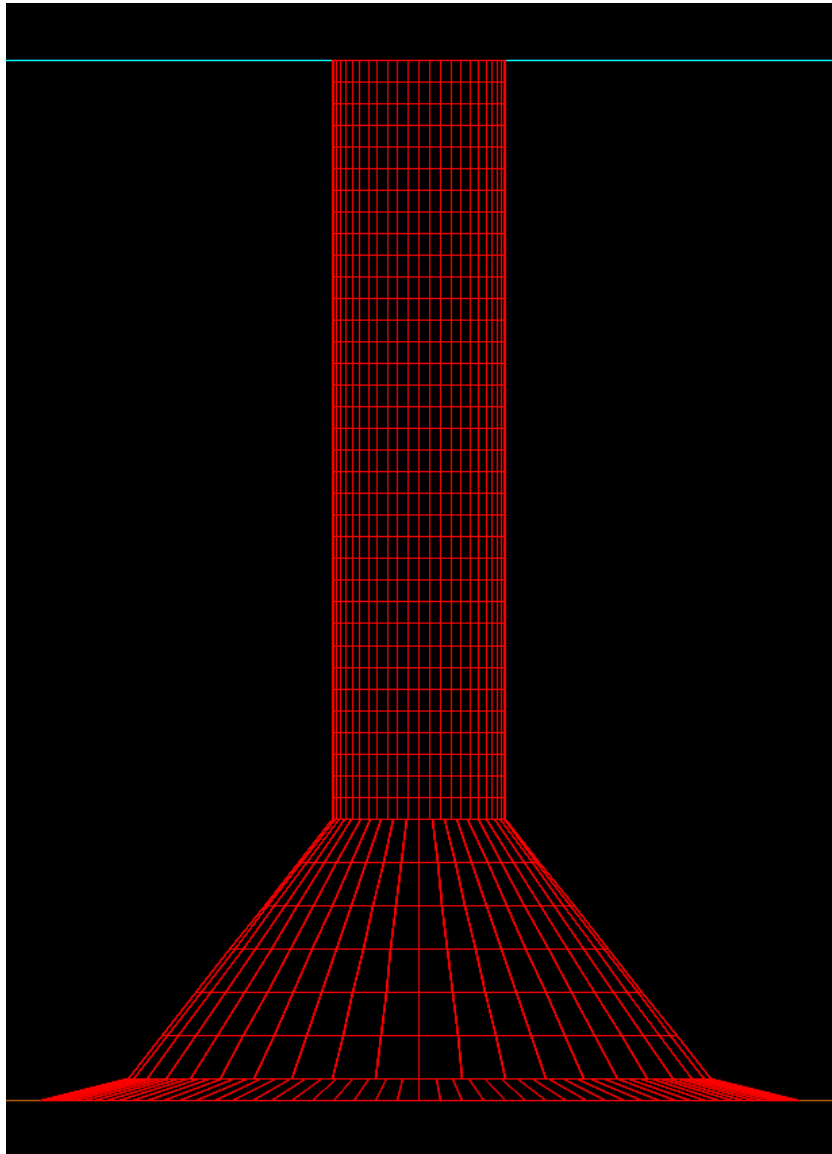


Figure 6.12: Mesh panel model for the preliminary design optimized for minimal concrete material and cheapest ballast material. The base diameter is 35 m, the transition point is located at 35.0 m below SWL, and the ballast density is 2000 kg/m^3 .

6.3.2. Ease of manufacturing

All the modelled designs in Appendix D passed the cone slope check, which means their cone slope angles are below 45 degrees. Any design that stays below this limit will be able to be produced and not have any additional local weaknesses. In practice, avoiding angles near this limit is best, as small angles are preferred. A larger cone angle increases the complexity of the design and therefore increases the manufacturing costs. Nevertheless, minimizing the total weight of the structure should be prioritized over minimizing the cone slope angle (while not exceeding the limit of 45 degrees).

Hence, in Table 6.10, a suggestion is given for an optimal preliminary design, where a maximum cone angle of 20 degrees is enforced. The proposed design is shown in Figure 6.13 and has a ballast density of 2500 kg/m^3 , a base diameter of 35.0 m, and a cylinder-cone transition point located at -20.0 m relative to the SWL.

Table 6.10: Sensitivity analysis results of a preliminary design optimized for manufacturing, where the base diameter is 35 m, the cylinder-cone transition point is located at -20.0 m, and the ballast density is varied (1500/2000/2500 kg/m^3).

Load case	LC 1			LC 2				
	1500	2000	2500	1500	2000	2500		
Ballast density [kg/m^3]	1500	2000	2500	1500	2000	2500		
Base diameter [m]	35.0	35.0	35.0	35.0	35.0	35.0		
Transition point [m]	-20.0	-20.0	-20.0	-20.0	-20.0	-20.0	Volume [m ³]	
Bearing cap. utiliz [%]	193.6	93.3	71.7	396.1	146.9	100.0	Concrete	2455
Sliding cap. utiliz [%]	58.8	42.4	33.2	88.2	63.6	49.8	Ballast	7873
Overturing cap. utiliz [%]	76.5	55.3	43.2	64.0	46.2	36.1		
Full contact utiliz. [%]	88.5	63.9	50.0	73.9	53.4	41.8	Cone slope	
1st Nat. frequency [Hz]	0.208	0.186	0.170	0.208	0.186	0.170	[deg]	19.9

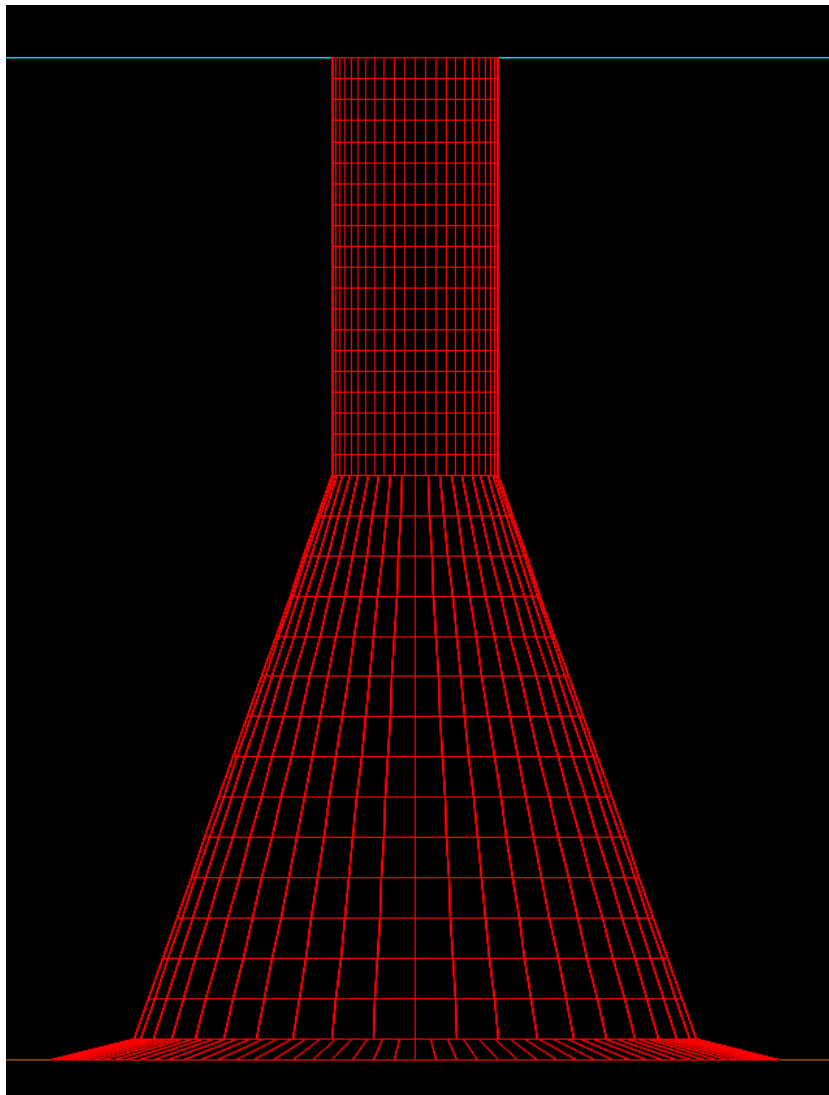


Figure 6.13: Mesh panel model for the preliminary design optimized for manufacturing, where the base diameter is 35 m, the cylinder-cone transition point is located at -20.0 m, and the ballast density is 2500 kg/m^3 .

6.3.3. Balanced design

In this section a balanced preliminary GBF design is provided, which takes into account all the design objectives from the previous sections. It was created by minimizing the required amount of concrete material while strictly using the cheapest ballast material (2000 kg/m^3) and a cone slope angle of approximately 30 degrees.

The final analysis results are given in Table 6.11, whereas the potential balanced design is shown in Figure 6.14. This design meets all the requirements and objectives while utilizing a ballast density of 2000 kg/m^3 , a base diameter of 35.0 m, and a cylinder-cone transition point of 30 m below the SWL.

Table 6.11: Sensitivity analysis results of a balanced preliminary design, where the base diameter is 35 m, the cylinder-cone transition point is located at -30.0 m, and the ballast density is varied ($1500/2000/2500 \text{ kg/m}^3$).

Load case	LC 1			LC 2				
Ballast density [kg/m^3]	1500	2000	2500	1500	2000	2500		
Base diameter [m]	35.0	35.0	35.0	35.0	35.0	35.0		
Transition point [m]	-30.0	-30.0	-30.0	-30.0	-30.0	-30.0	Volume [m3]	
Bearing cap. utiliz [%]	144.9	78.4	61.2	184.1	95.3	72.0	Concrete	2306
Sliding cap. utiliz [%]	52.0	39.2	31.4	75.5	56.9	45.7	Ballast	5883
Overturning cap. utiliz [%]	78.0	58.9	47.3	58.1	43.8	35.2		
Full contact utiliz. [%]	90.1	68.0	54.6	67.1	50.6	40.6	Cone slope	30.2
1st Nat. frequency [Hz]	0.224	0.213	0.204	0.224	0.213	0.204	[deg]	

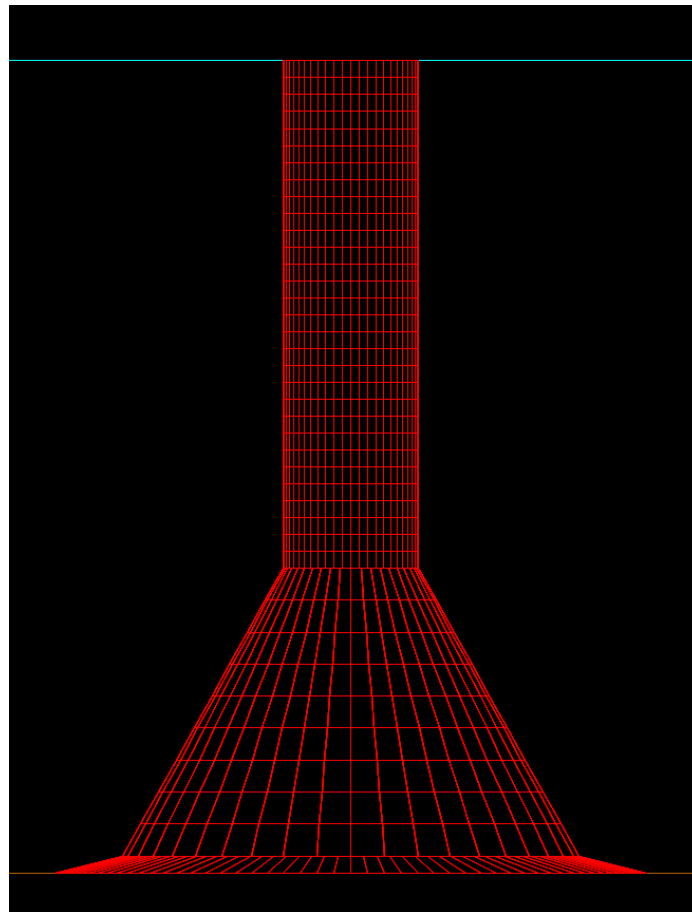


Figure 6.14: Mesh panel model for the balanced preliminary design, where the base diameter is 35 m, the cylinder-cone transition point is located at -30.0 m, and the ballast density is 2000 kg/m^3 .

Methodology for preliminary design of gravity-based offshore wind foundations

In the previous sections, the complete process of an optimal preliminary design for a reference gravity-based foundation (GBF) was successfully executed. This section will discuss the required design steps, as previously shown in Figure 1.8.

First, a hydrodynamic load model based on a linear potential flow (LPF) solution was created in OrcaFlex. To obtain a suitable GBF mesh panel model, a sensitivity study has to be performed to find the required number of elements to achieve mesh convergence. Besides diffraction effects, the vertical contribution of the pressure becomes significant for large conical structures (bottom diameter at least twice as large as top diameter). Since there is a phase lag between the horizontal and vertical hydrodynamic loads, this will produce a reduced overturning moment. Therefore, empirical wave load theories (e.g. Morison's equation or MacCamy-Fuchs correction) are always invalid for conical GBFs.

The LPF results deviated slightly from the Computational Fluid Dynamics (CFD) data, mainly due to the neglect of flow separation and complex phenomena such as breaking waves and fully nonlinear wave kinematics. Other phenomena (wave loads up to the instantaneous linear free surface, drag loads, and nonlinear second-order potential flow) were investigated to potentially improve the model's accuracy. The wave loads up to the instantaneous linear free surface are only relevant for waves with low wave periods, whereas the drag contribution is negligible due to the high dependency on inertia loads for large bodies. The nonlinear second-order potential flow solution produced illogical results due to its high complexity and dependency on convergence. Additionally, since it is significantly more computationally expensive than LPF, further investigations should be performed to study the influence of nonlinear wave loads.

Nevertheless, based on the provided CFD data of seven wave simulations, LPF was found to be sufficiently accurate and highly cost-efficient for the preliminary design phase. The GBF should be modelled in a broader range of wave cases in varying water depths using CFD to reinforce this conclusion. In the detailed design phase, CFD simulations are still required, but it must be acknowledged that the accuracy is highly dependent on the user's knowledge. It should only be considered a useful tool that adds value to the complete model since there are many uncertainties regarding the used turbulence models (e.g. inaccurate modelling of complex turbulence layers for oscillatory flow).

For a GBF in intermediate water depths, the overturning moment is the decisive force due to the arm's length. As most industry standards focus on calculations with absolute maximum loads, it is inevitable to differ from this. Nevertheless, a better measure would be the integrated impulse, which is the force over time. This is physically more correct since it considers the magnitude and duration of the load. To clarify, a long-lasting wave with a moderate magnitude could be more disastrous than a momentary extreme wave.

The initial design was determined using the environmental conditions, wind turbine data and design guidelines. As the environmental loads depend on the metocean data, this data must be of high quality. Furthermore, since the guidelines were based on standard industry practice from Rambøll, it does not guarantee an optimal starting point for all future projects. Therefore, an iterative optimization procedure will be unavoidable for any preliminary design.

The design basis is the primary document that contains all the essential information for a foundation designer. Since it is project-specific, the foundation type can depend on the feasibility (e.g. construction, transportation and installation) and technical details (e.g. scour protection or lifting lugs). By combining the design basis with the derived hydrodynamic load model and a simplified structural model in ROSAP, the full preliminary design model was complete.

The simplified structural model is used to perform a natural frequency analysis to ensure structural integrity. The aim is to avoid resonance caused by excitations due to environmental loads, the rotational frequency of the turbine (1P) and the blade-passing frequency (3P). Due to the high stiffness of GBFs, resonance is not the main challenge, and therefore it is relatively easy to design the first natural frequency to be within the desired soft-stiff region. For GBFs, the main concerns are regarding the weight and cost-efficiency of manufacturing, transporting, and installing.

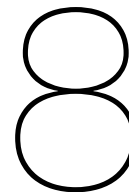
The complete model was verified using design checks based on industry standards and ensured foundation stability for all limit states. To ensure safety within any possible condition, dozens of realistic load conditions should be considered. The design checks are based on simplified geotechnical calculations (e.g. no scour, erosion, soil suction force, extreme eccentricity due to the RNA, marine growth or degrading properties over time) and include safety factors. These factors are defined by industry standards but also common practice, which brings additional uncertainty regarding the validity. Additionally, the various standards do not consistently apply the same formulas within the calculations.

The requirements for foundation stability are often driven by the size and weight of the structure. Therefore, sensitivity analyses were performed based on the following design parameters: ballast density, footprint and cone height. Although there are more potential design parameters (e.g. scour protection, concrete density, wall thickness, and base plate thickness), a general observation could be successfully made.

In essence, if the adjustment of a parameter causes the total weight to rise, the decreased eccentricity will enhance the foundation's stability. In all cases, the relative weight increase is more significant than the stiffness increase; therefore, the first natural frequency decreases. Similarly, if the conical section is enlarged by increasing the footprint or cone height, the effect of the weight increase is more significant than the larger hydrodynamic loads. Lastly, increasing the footprint or decreasing the cone height increases the cone slope angle.

Designs in the real world can have multiple objectives, and therefore there can be multiple optimal designs. For a GBF, these objectives are often related to weight, costs, or even both. A few potential design objectives could be: minimizing the construction (based on amount of material, dry weight and manufacturing complexity), transportation (based on concrete weight) or installation costs (based on dry weight and height of structure). Generally, a combination of design objectives with varying priorities should be considered for the final design. In addition, as this manual optimization of the preliminary design is a labour-intensive process, the implementation of optimization algorithms should be considered.

Lastly, GBFs are uncommonly used, so the design process can be considered obscure. This thesis presents a proposal for a simplified preliminary design methodology for concrete gravity-based foundations for offshore wind. Although it was established for conical GBFs, it can also be valid for different types of concrete GBFs. Furthermore, the hydrodynamic load model can be used for complex structures, and the structural model would only need minor modifications to function correctly. Nonetheless, for a complete preliminary design methodology that can be directly applied in the industry, it would require considerably more factors to be considered.



Conclusion and Recommendations

In this thesis, a simplified design methodology for the preliminary design of concrete gravity-based foundations (GBF) for offshore wind has successfully been established. The hydrodynamic load model is based on a linear potential flow solution calculated in the diffraction analysis program OrcaFlex. Although there were slight deviations in results between the hydrodynamic load model and the Computational Fluid Dynamics (CFD) simulations, they proved to be sufficiently accurate and highly cost-efficient for the conceptual design of GBFs. Nevertheless, as CFD offers state-of-the-art wave load modelling, it is still required for the detailed design.

A simplified structural model was created in Rambøll Offshore Structural Analysis Programs to perform a natural frequency analysis. Due to the high stiffness of GBFs, resonance is not considered the main challenge, and therefore it is reasonably easy to design the first natural frequency to be within the desired soft-stiff regions (between the 1P rotor frequency and 3P blade-passing frequency). The main concerns for GBFs depend on the weight and cost-efficiency of manufacturing, transportation, and installation.

The initial design was based on the environmental conditions, wind turbine data and design guidelines. Since the guidelines are based on standard industry practice, it does not guarantee an optimal starting point for every project; therefore, an iterative optimisation procedure of the design will always be required. The complete model was verified using design checks based on industry standards and ensured structural integrity for the primary limit states. These checks utilised simplified geotechnical calculations and partial load safety factors depending on the limit state.

The requirements for foundation stability are often driven by the size and weight of the structure. Therefore, sensitivity analyses were performed with various design parameters to identify the main factors influencing the design. In essence, if the weight or size of the structure increases, it will enhance the foundation's stability despite the increasing hydrodynamic loads. Additionally, since the relative weight increase is always more significant than the stiffness increase, the first natural frequency of the GBF decreases.

Designs often have multiple objectives, and therefore multiple optimal designs are available. For a GBF, these objectives are often related to weight, costs, or even both. Generally, a combination of design objectives with varying priorities should be considered. As this manual optimisation of the preliminary design is a labour-intensive process, implementing optimisation algorithms is recommended. The initial design workflow (Figure 1.8) was updated with an automated optimisation with a convergence check and is shown in Figure 8.1.

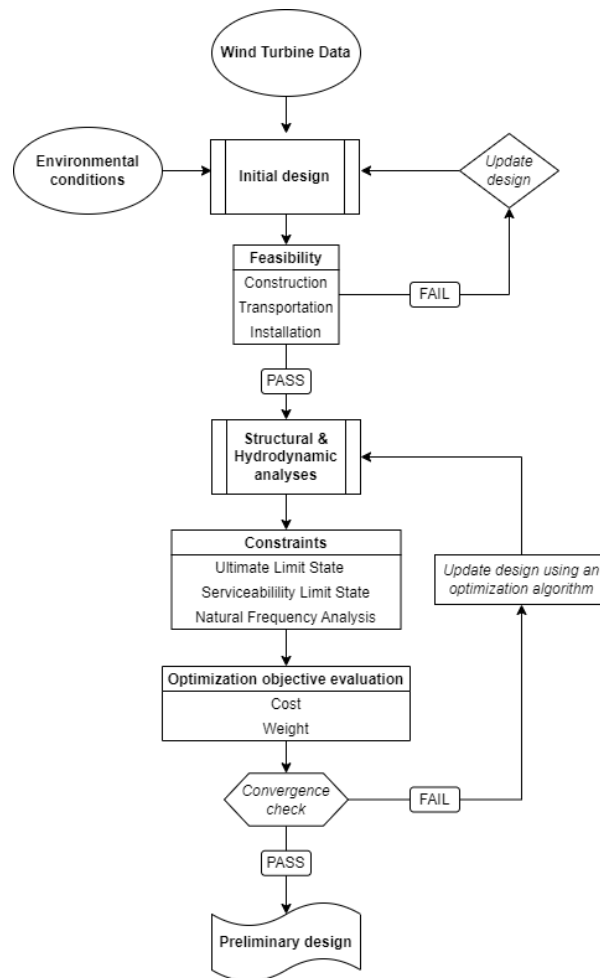


Figure 8.1: Preliminary design workflow for concrete gravity-based offshore wind foundations, where an optimization algorithm and automatic convergence check is implemented.

Although this design methodology is expected to work universally for a large variety of GBFs, it is still recommended to test it for case studies with different types of GBFs. Additionally, within the scope of this thesis, only two design load cases were treated. For a complete representative design, dozens of design load conditions should be examined to ensure safety within any scenario. Finally, the design guidelines are widely based on standard industry practice and could differ for other structures. Especially the validity of the load safety factors can be argued and should therefore be investigated.

Furthermore, it should be researched if the hydrodynamic load model is valid for all wave conditions. The GBF should be modelled in a broader range of wave cases in varying water depths using CFD to realise this. Contrarily, alternative hydrodynamic models or combinations of models could be considered to increase the accuracy. A few possibilities for further research regarding the hydrodynamic loads:

- A) In-depth study of the nonlinear second-order potential flow solution in OrcaFlex;
- B) Utilising nonlinear irregular wave models for the incident flow field (e.g. advanced Boussinesq models [48]);
- C) A model consisting of coupled domains, using potential flow-based wave models in the far-field and CFD models in the near-field of the structure to calculate the hydrodynamic loads. This can be achieved using various techniques where the main difference lies in whether the domains overlap (e.g. Euler Overlay Method [69]) or do not overlap (e.g. Domain Decomposition [70]).

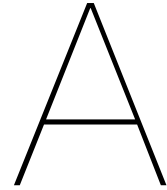
References

- [1] United Nations. "COP26 - The Glasgow Climate Pact." <https://ukcop26.org>. (Nov. 2021).
- [2] International Renewable Energy Agency, *Future of Wind - A Global Energy Transformation*, <https://www.irena.org/publications/2019/Oct/Future-of-wind>, Oct. 2019.
- [3] International Renewable Energy Agency, *Renewable Power Generation Costs in 2020*, <https://www.irena.org/publications/2021/Jun/Renewable-Power-Costs-in-2020>, Jun. 2021.
- [4] T. J. Stehly and P. C. Beiter, "2019 Cost of Wind Energy Review," National Renewable Energy Lab.(NREL), Golden, CO (United States), Tech. Rep., Dec. 2020.
- [5] O. Edenhofer, R. Pichs-Madruga, Y. Sokona, *et al.*, *Renewable energy sources and climate change mitigation: Special report of the intergovernmental panel on climate change*. Cambridge University Press, 2011.
- [6] Wind Europe, *Wind energy in Europe - 2020 Statistics and the outlook for 2021-2025*, <https://windeurope.org/intelligence-platform/product/wind-energy-in-europe-in-2020-trends-and-statistics>, Feb. 2021.
- [7] M. D. Esteban, J.-S. López-Gutiérrez, and V. Negro, "Gravity-based foundations in the offshore wind sector," *Journal of Marine Science and Engineering*, vol. 7, no. 3, p. 64, 2019.
- [8] V. Negro, J.-S. López-Gutiérrez, M. D. Esteban, P. Alberdi, M. Imaz, and J.-M. Serraclara, "Monopiles in offshore wind: Preliminary estimate of main dimensions," *Ocean Engineering*, vol. 133, pp. 253–261, 2017.
- [9] W. de Vries, N. K. Vemula, P. Passon, *et al.*, "Final report wp4. 2: Support structure concepts for deep water sites," *UpWind D4*, vol. 2, 2011.
- [10] F. A. Olutoge and G. M. Amusan, "The effect of sea water on compressive strength of concrete," *International Journal of Engineering Science Invention*, vol. 3, no. 7, pp. 23–31, 2014.
- [11] P. H. Dahl, C. A. de Jong, and A. N. Popper, "The underwater sound field from impact pile driving and its potential effects on marine life," *Acoustics Today*, vol. 11, no. 2, pp. 18–25, 2015.
- [12] R. P. Fernandez and M. L. Pardo, "Offshore concrete structures," *Ocean Engineering*, vol. 58, pp. 304–316, 2013.
- [13] A. Bolle, P. Mercelis, W. Goossens, and P. Haerens, "Scour monitoring and scour protection solution for offshore gravity based foundations," in *Scour and Erosion*, 2010, pp. 491–500.
- [14] K. P. Mehta, "Reducing the environmental impact of concrete," *Concrete international*, vol. 23, no. 10, pp. 61–66, 2001.
- [15] P. van der Male, *Lecture notes of OE44135: Offshore Wind Support Structures*. Delft University of Technology, 2021.
- [16] A. Henderson and M. Zaaijer, "Hydrodynamic loading of compact structures and the effect on foundation design," in *Proceedings of MAREC*, Citeseer, 2002.
- [17] International Electrotechnical Commission, *IEC 61400-3-1: Wind energy generation systems - Part 3-1: Design requirements for fixed offshore wind turbines*. Geneva: IEC, 2019.
- [18] International Organization for Standardization, *ISO 19903: Petroleum and natural gas industries – Concrete Offshore structures*. Geneva: ISO, 2019.
- [19] Det Norske Veritas, *DNV-ST-0126: Support structures for wind turbines*. Oslo: DNV, 2018.
- [20] Det Norske Veritas, *DNV-ST-0437: Loads and site conditions for wind turbines*. Oslo: DNV, 2016.
- [21] Det Norske Veritas, *DNV-RP-C205: Environmental Conditions and Environmental Loads*. Oslo: DNV, 2019.

- [22] Det Norske Veritas, *DNV-RP-C212: Offshore Soil Mechanics and Geotechnical Engineering*. Oslo: DNV, 2017.
- [23] Det Norske Veritas, *DNV-ST-C502: Offshore concrete structures*. Oslo: DNV, 2018.
- [24] J. Hu, *Comparison of Hydrodynamic Models for Gravity-Based Offshore Wind Foundations*. Norwegian University of Science and Technology, 2022.
- [25] J. Morison, J. Johnson, and S. Schaaf, "The force exerted by surface waves on piles," *Journal of Petroleum Technology*, vol. 2, no. 05, pp. 149–154, 1950.
- [26] R. MacCamy and R. A. Fuchs, *Wave forces on piles: a diffraction theory*, 69. US Beach Erosion Board, 1954.
- [27] C. Lee and J. Newman, "Journal of Ship Research First and Second-Order Wave Effects on a Submerged Spheroid," *Journal of ship research*, vol. 35, no. 03, pp. 183–190, 1991.
- [28] M. H. Patel, "14 - offshore engineering," in *Mechanical Engineer's Reference Book (Twelfth Edition)*, E. H. Smith, Ed., Twelfth Edition, Butterworth-Heinemann, 1994, pp. 14-1-14–34, ISBN: 978-0-7506-1195-4. DOI: <https://doi.org/10.1016/B978-0-7506-1195-4.50018-X>.
- [29] T. Sarpkaya, *Wave Forces on Offshore Structures*, 1st ed. Cambridge University Press, 2010.
- [30] B. Mutlu Sumer and J. Fredsøe, *Hydrodynamics around cylindrical structures*. World scientific, 2006, vol. 26.
- [31] R. Dean and R. Dalrymple, *Water Wave Mechanics for Engineers & Scientists*. WSPC, 1991, vol. 2.
- [32] G. N. Watson, *A treatise on the theory of Bessel functions*. Cambridge university press, 1995.
- [33] Orcina Ltd. "Orcina: Home of the world's leading software package, for marine systems design and analysis." <https://www.orcina.com/>. (2022).
- [34] T. Kristiansen, "Chapter 6: Rigid body motions and Chapter 7: Bodies in water," in *TMR4182 Marine Dynamics Compendium*, D. of Marine Technology, Ed., Norwegian University of Science and Technology, 2021, pp. 104–174.
- [35] A. Babarit and G. Delhommeau, "Theoretical and numerical aspects of the open source BEM solver NEMOH," in *11th European wave and tidal energy conference (EWTEC2015)*, 2015.
- [36] J. M. Journée and W. Massie, *Offshore hydromechanics*. CITG Section Hydraulic Engineering (<2005), 2000, vol. 1.
- [37] B. Andersson, R. Andersson, L. Håkansson, M. Mortensen, R. Sudiyo, and B. Van Wachem, *Computational fluid dynamics for engineers*. Cambridge university press, 2011.
- [38] M. C. Ong, "CFD applications in offshore engineering," in *EPJ Web of Conferences*, EDP Sciences, vol. 143, 2017, p. 01 002.
- [39] P. Sagaut, *Large eddy simulation for incompressible flows: an introduction*. Springer Science & Business Media, 2006.
- [40] F. R. Menter, M. Kuntz, and R. Langtry, "Ten years of industrial experience with the SST turbulence model," *Turbulence, heat and mass transfer*, vol. 4, no. 1, pp. 625–632, 2003.
- [41] G. Alfonsi, "Reynolds-averaged Navier–Stokes equations for turbulence modeling," 2009.
- [42] H. Schlichting and K. Gersten, *Boundary-layer theory*. Springer Science & Business Media, 2003.
- [43] T. L. Bergman, F. P. Incropera, D. P. DeWitt, and A. S. Lavine, *Fundamentals of heat and mass transfer*, 7th ed. John Wiley & Sons, 2011, pp. 389–391.
- [44] European Research Community on Flow, Turbulence and Combustion, *Best Practice Guidelines, Computational Fluid Dynamics of Dispersed Multi-Phase Flows*. ERCOFTAC, 2008.
- [45] C. W. Hirt and B. D. Nichols, "Volume of fluid (VOF) method for the dynamics of free boundaries," *Journal of computational physics*, vol. 39, no. 1, pp. 201–225, 1981.
- [46] H. Bredmose and N. G. Jacobsen, "Breaking wave impacts on offshore wind turbine foundations: focused wave groups and CFD," in *International Conference on Offshore Mechanics and Arctic Engineering*, vol. 49118, 2010, pp. 397–404.

- [47] G. Wu and O. H. Oakley Jr, "CFD modeling of fully nonlinear water wave tank," in *International Conference on Offshore Mechanics and Arctic Engineering*, vol. 43451, 2009, pp. 815–823.
- [48] P. A. Madsen, H. Bingham, and H. Liu, "A new Boussinesq method for fully nonlinear waves from shallow to deep water," *Journal of Fluid Mechanics*, vol. 462, pp. 1–30, 2002.
- [49] J. Sharma and R. Dean, "Second-order directional seas and associated wave forces," *Society of Petroleum Engineers Journal*, vol. 21, no. 01, pp. 129–140, 1981.
- [50] M. van der Meulen, T. Ashuri, G. van Bussel, and D. Molenaar, "Influence of Nonlinear Irregular Waves on the Fatigue Loads of an Offshore Wind Turbine," Nov. 2012. DOI: 10.13140/2.1.3034.5606.
- [51] M. Lewis, S. Neill, P. Robins, M. Hashemi, and S. Ward, "Characteristics of the velocity profile at tidal-stream energy sites," *Renewable Energy*, vol. 114, pp. 258–272, 2017, Wave and Tidal Resource Characterization, ISSN: 0960-1481. DOI: <https://doi.org/10.1016/j.renene.2017.03.096>.
- [52] Z. Peng, "Wave slamming impact on offshore wind turbine foundations," in *ICCE*, 2014, pp. 43–50.
- [53] B. T. Paulsen, B. de Sonnevile, M. van der Meulen, and N. G. Jacobsen, "Probability of wave slamming and the magnitude of slamming loads on offshore wind turbine foundations," *Coastal Engineering*, vol. 143, pp. 76–95, 2019.
- [54] A. Marson. "Breaking Waves in Offshore Wind." <https://www.empireengineering.co.uk/breaking-waves-in-offshore-wind>. (2019).
- [55] G. Z. Forristall and K. C. Ewans, "Worldwide Measurements of Directional Wave Spreading," *Journal of Atmospheric and Oceanic Technology*, vol. 15, no. 2, pp. 440–469, 1998.
- [56] S. K. Chakrabarti, *Handbook of Offshore Engineering*. Elsevier, 2005, pp. 79–131.
- [57] M. M. Rienecker and J. D. Fenton, "A Fourier approximation method for steady water waves," *Fluid Mechanics*, vol. 104, pp. 119–137, 1981.
- [58] S. K. Chakrabarti, *Hydrodynamics of offshore structures*. WIT press, 1987.
- [59] R. C. Nelson, "Depth limited design wave heights in very flat regions," *Coastal Engineering*, vol. 23, no. 1-2, pp. 43–59, 1994.
- [60] T. Kristiansen, R. Baarholm, and C. T. Stansberg, "Validation of second-order analysis in predicting diffracted wave elevation around a vertical circular cylinder," in *The Fourteenth International Offshore and Polar Engineering Conference*, OnePetro, 2004.
- [61] Siemens Digital Industries Software, *Simcenter STAR-CCM+, version 2021.1*, 2021.
- [62] Meteorological Service of New Zealand Ltd 2022. "Hindcast2 - MetoceanView." <https://app.metoceanview.com/hindcast-squared>. (2022).
- [63] K. Hasselmann, T. P. Barnett, E. Bouws, *et al.*, "Measurements of wind-wave growth and swell decay during the joint north sea wave project (jonswap).," *Ergaenzungsheft zur Deutschen Hydrographischen Zeitschrift, Reihe A*, 1973.
- [64] Det Norske Veritas, *Guidelines for Design of Wind Turbines*. Oslo: DNV, 2002.
- [65] J. B. Burland, A. Penman, and K. A. Gallagher, "Behaviour of a gravity foundation under working and failure conditions," in *SPE European Petroleum Conference*, OnePetro, 1978.
- [66] M. Gambhir, *Fundamentals of SOLID MECHANICS : A Treatise on Strength of Materials*. Prentice-Hall Of India Pvt. Limited, 2009, ISBN: 9788120338708.
- [67] C. Macfarlane. "Market Report: Global Heavy Lift Vessel Sector." (Aug. 2020), [Online]. Available: <https://www.oedigital.com/news/481219-market-report-global-heavy-lift-vessel-sector>.
- [68] J. Stumo. "Offshore wind market propels demand for heavy-lift vessels." (Feb. 2022), [Online]. Available: <https://www.offshore-mag.com/rigs-vessels/article/14224067/offshore-wind-market-propels-demand-for-heavylift-vessels>.

-
- [69] J. Kim, J. O'Sullivan, and A. Read, "Ringling analysis of a vertical cylinder by euler overlay method," in *International Conference on Offshore Mechanics and Arctic Engineering*, American Society of Mechanical Engineers, vol. 44915, 2012, pp. 855–866.
- [70] B. T. Paulsen, H. Bredmose, and H. B. Bingham, "An efficient domain decomposition strategy for wave loads on surface piercing circular cylinders," *Coastal Engineering*, vol. 86, pp. 57–76, 2014.



Data from literature study

In this appendix the used environmental conditions and GBF design dimensions from the reference study in [24] are provided.

Table A.1: Environmental conditions for the reference GBF study in [24].

Parameter	Value	Unit
Water depth d	48	m
Extreme wave height (50 y) H	24.18	m
Wave period T	13	s
Surface tidal current speed u_s	1.50	m/s

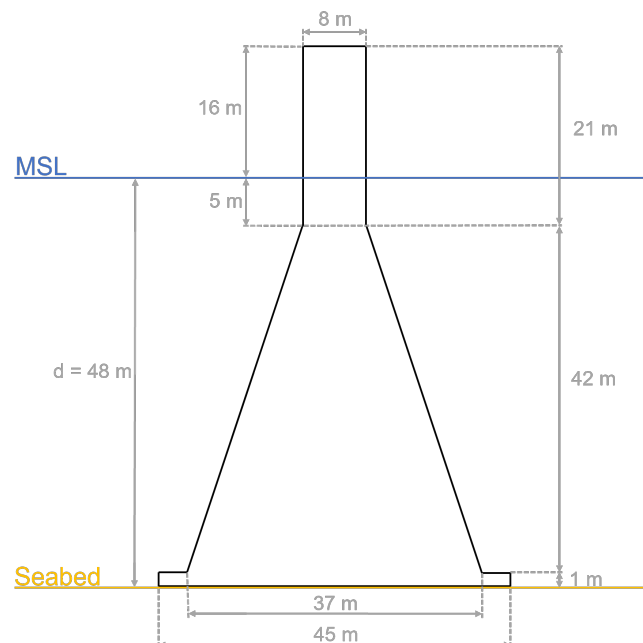


Figure A.1: Reference GBF design with dimensions.

B

Results of hydrodynamic load model validation

In this appendix the complete results of the hydrodynamic load model validation (chapter 4) is provided.

B.1. Comparison between CFD and LPF (OrcaWave)

The resulting hydrodynamic loads are given in values in Table B.1 and as figures for each individual wave simulation in Figure B.1-B.7.

Table B.1: Comparison between hydrodynamic load results of CFD and LPF (OrcaWave).

Wave	H [m]	T [s]	L [m]	CFD		LPF		Relative difference	
				$F_{x,max}$ [MN]	$M_{y,max}$ [MNm]	$F_{x,max}$ [MN]	$M_{y,max}$ [MNm]	$F_{x,max}$ [%]	$M_{y,max}$ [%]
1	13.2	9.0	133.3	57.0	1210	56.3	1017	-1.2%	-19.0%
2	19.7	11.5	200.0	91.3	2302	101.2	2789	10.8%	17.5%
3	19.7	14.0	258.1	99.2	2441	99.9	3114	0.7%	21.6%
4	4.0	7.0	78.3	10.4	42.0	9.9	31.4	-5.3%	-33.8%
5	4.0	9.0	122.5	16.9	353	17.0	308	0.6%	-14.6%
6	4.0	11.5	179.0	20.4	551	20.5	566	0.5%	2.7%
7	4.0	14.0	234.2	19.0	606	20.3	632	6.8%	4.1%

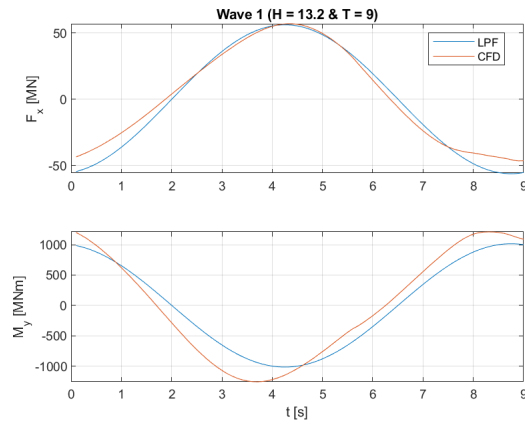


Figure B.1: Wave 1: Hydrodynamic loads (LPF and CFD)

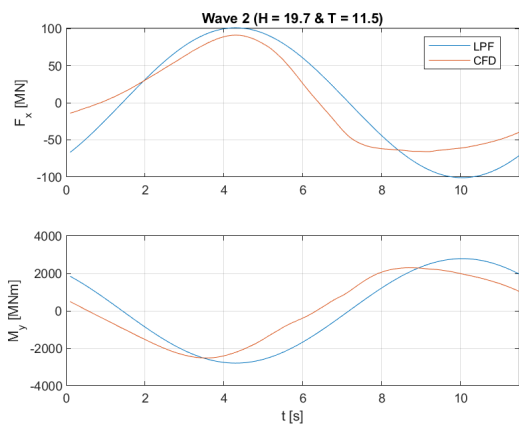


Figure B.2: Wave 2: Hydrodynamic loads (LPF and CFD)

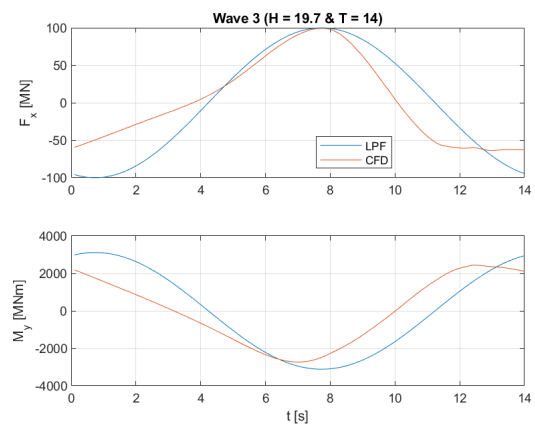


Figure B.3: Wave 3: Hydrodynamic loads (LPF and CFD)

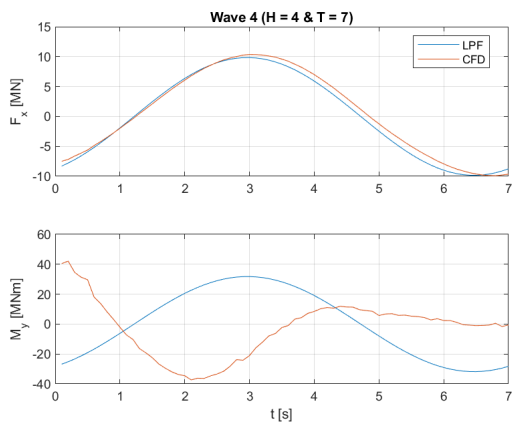


Figure B.4: Wave 4: Hydrodynamic loads (LPF and CFD)

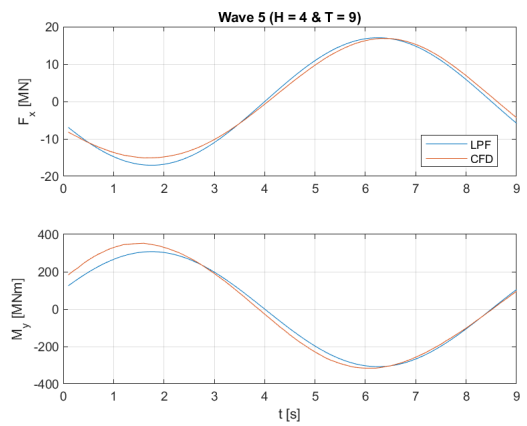


Figure B.5: Wave 5: Hydrodynamic loads (LPF and CFD)

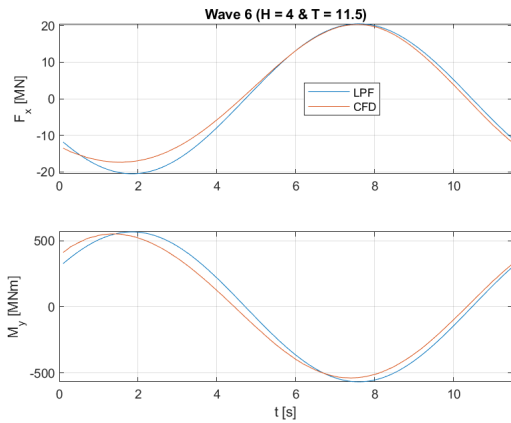


Figure B.6: Wave 6: Hydrodynamic loads (LPF and CFD)

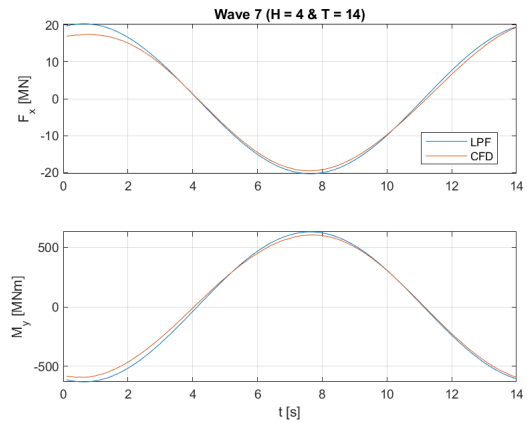


Figure B.7: Wave 7: Hydrodynamic loads (LPF and CFD)

B.2. Comparison between monopile and reference GBF

The resulting hydrodynamic loads for both a monopile (MP) with a 10 m diameter and the reference GBF are given in values in Table B.2 and as figures for each individual wave simulation in Figure B.8-B.14.

Table B.2: Comparison between hydrodynamic loads on reference GBF and monopile.

Wave	H [m]	T [s]	L [m]	GBF		Monopile		Difference	
				$F_{x,max}$	$M_{y,max}$	$F_{x,max}$	$M_{y,max}$	$F_{x,max}$	$M_{y,max}$
				[MN]	[MNm]	[MN]	[MNm]	[%]	[%]
1	13.2	9.0	121.0	56.3	1017	10.3	232	447%	338%
2	19.7	11.5	177.9	101.2	2789	13.7	282	639%	889%
3	19.7	14.0	232.4	99.9	3114	12.0	238	733%	1208%
4	4.0	7.0	76.1	9.9	31.4	3.2	83.2	208%	-62%
5	4.0	9.0	121.0	17.0	308	3.1	70.2	448%	339%
6	4.0	11.5	177.9	20.5	566	2.8	57.4	632%	886%
7	4.0	14.0	232.4	20.3	632	2.4	48.2	746%	1211%

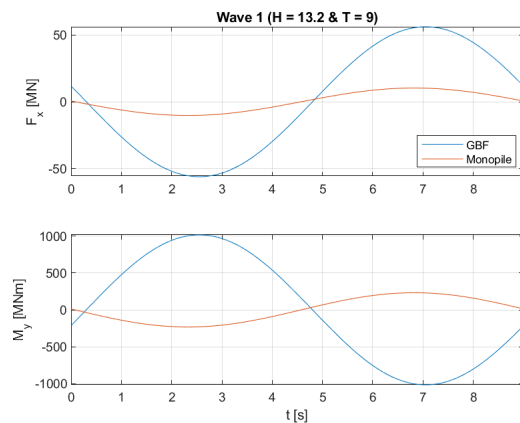


Figure B.8: Wave 1: Hydrodynamic loads (MP and GBF).

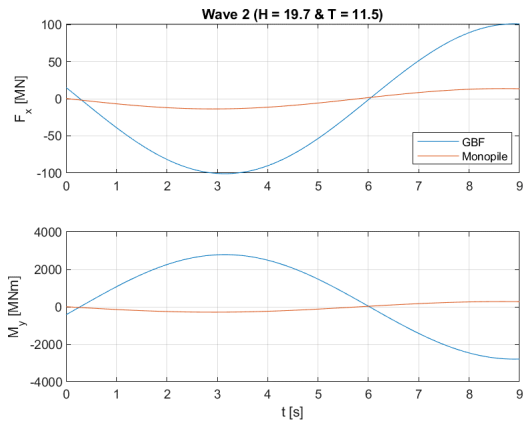


Figure B.9: Wave 2: Hydrodynamic loads (MP and GBF).

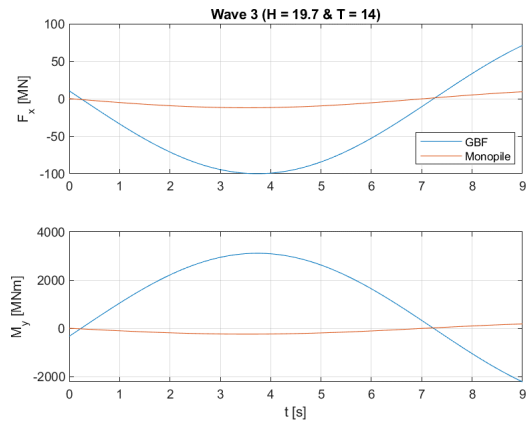


Figure B.10: Wave 3: Hydrodynamic loads (MP and GBF).

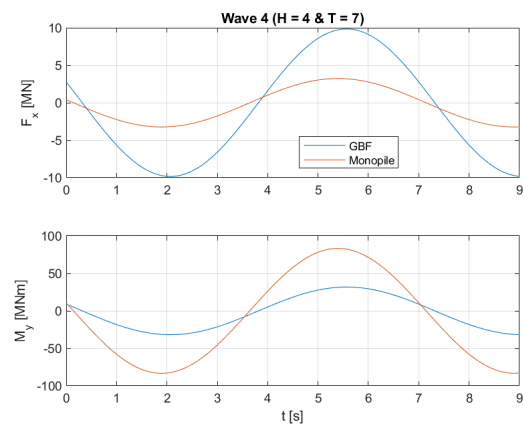


Figure B.11: Wave 4: Hydrodynamic loads (MP and GBF).

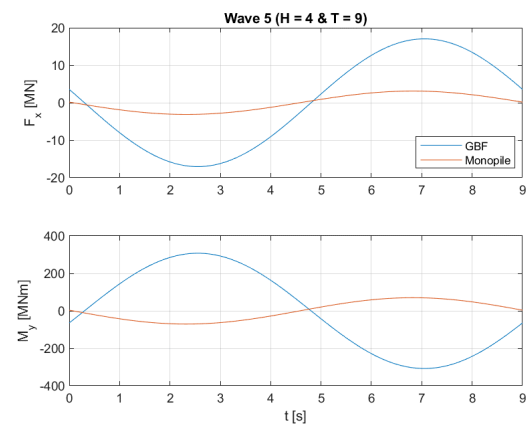


Figure B.12: Wave 5: Hydrodynamic loads (MP and GBF).

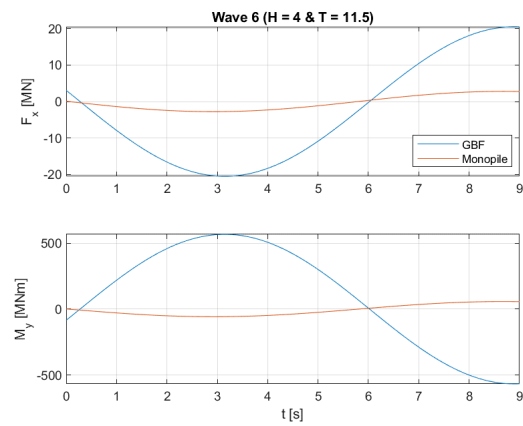


Figure B.13: Wave 6: Hydrodynamic loads (MP and GBF).

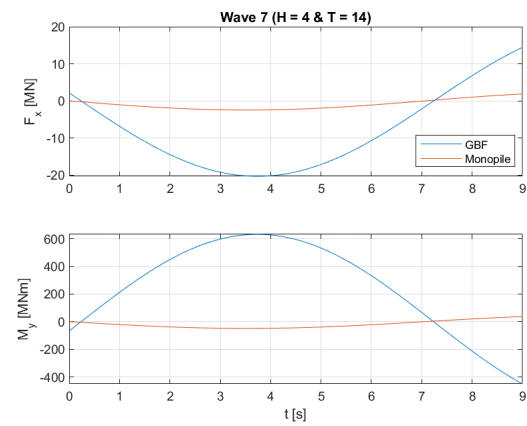


Figure B.14: Wave 7: Hydrodynamic loads (MP and GBF).

B.3. Comparison between first-order linear potential flow and second-order nonlinear potential flow

In this appendix the complete results can be found of the second-order nonlinear potential flow study treated in subsection 4.4.2. Multiple variants of the nonlinear second-order potential flow (NLPF) have been investigated to examine the effect of the QTF parameters. In Table B.3, each simulation and the values for the used parameters are described. For an in-depth description of these parameters, the reader is kindly referred to the Data: QTFs section within the OrcaWave manual [33].

The following NLPF simulations were executed:

- Free surface panelled zone (FSPZ) with inner radius R_{in} ;
- Free surface quadrature zone (FSQZ) with number of annuli A , radius step dR , radial nodes n_R , and azimuthal nodes n_A ;
- Free surface outer circle (FSOC) with outer radius R_{out} and number of segments dS ;
- Free surface asymptotic zone (FSAZ) with expansion order O_E ;
- All the above mentioned options enabled (All).

Table B.3: Values for used parameters for each executed simulation in the nonlinear potential flow study.

Simulation	R_{in} [m]	A [-]	dR [m]	n_R [-]	n_A [-]	R_{out} [m]	dS [-]	O_E [-]
Linear PF (until FS)	0	0	0	0	0	0	0	0
Nonlinear PF (FSPZ)	100	0	0	0	0	0	0	0
Nonlinear PF (FSQZ)	100	50	5	10	10	0	0	0
Nonlinear PF (FSOC)	100	0	0	0	0	350	100	0
Nonlinear LPF (FSAZ)	100	0	0	0	0	0	0	15
Nonlinear PF (All)	100	50	5	10	10	350	100	15

In Table B.4-B.10, the resulting hydrodynamic loads on the reference GBF, based on NLPF, were calculated for all seven wave conditions. To include some reference values for this comparison study, the CFD data and the linear potential flow solution until the instantaneous linear free surface (FS) have been provided. Lastly, besides the minimum and maximum hydrodynamic loads, the absolute maximum base shear Fx_{abs} and overturning moment My_{abs} were also specified.

Table B.4: Resulting hydrodynamic loads for the CFD, LPF, and NLPF simulations for wave 1 ($H = 13.2$ m & $T = 9.0$ s).

Wave 1 H = 13.2 m T = 9.0 s	Fx_min [MN]	Fx_max [MNm]	My_min [MN]	My_max [MNm]	Fx_abs [MN]	My_abs [MNm]
Computational Fluid Dynamics	-46.5	57.0	-1258	1210	57.0	1258
Linear PF (until FS)	-56.9	56.0	-1010	987	56.9	1010
Nonlinear PF (FS paneled zone)	-56.0	56.9	-1116	1021	56.9	1116
Nonlinear PF (FS quadrature zone)	-56.4	56.6	-1124	1002	56.6	1124
Nonlinear PF (FS outer circle)	-57.8	55.0	-1174	988	57.8	1174
Nonlinear PF (FS asymptotic zone)	-54.9	58.1	-1077	1037	58.1	1077
Nonlinear PF (All options)	-56.7	56.2	-1137	1000	56.7	1137

B.3. Comparison between first-order linear potential flow and second-order nonlinear potential flow⁹⁴

Table B.5: Resulting hydrodynamic loads for the CFD, LPF, and NLPF simulations for wave 2 ($H = 19.7$ m & $T = 11.5$ s).

Wave 2 H = 19.7 m T = 11.5 s	Fx_min [MN]	Fx_max [MNm]	My_min [MN]	My_max [MNm]	Fx_abs [MN]	My_abs [MNm]
Computational Fluid Dynamics	-66.0	91.3	-2515	2302	91.3	2515
Linear PF (until FS)	-100.7	99.8	-2785	2759	100.7	2785
Nonlinear PF (FS paneled zone)	-112.0	90.8	-3052	2530	112.0	3052
Nonlinear PF (FS quadrature zone)	-107.5	97.0	-2932	2687	107.5	2932
Nonlinear PF (FS outer circle)	-110.2	93.2	-3000	2598	110.2	3000
Nonlinear PF (FS asymptotic zone)	-111.3	91.8	-3030	2562	111.3	3030
Nonlinear PF (All options)	-109.9	94.9	-2987	2638	109.9	2987

Table B.6: Resulting hydrodynamic loads for the CFD, LPF, and NLPF simulations for wave 3 ($H = 19.7$ m & $T = 14.0$ s).

Wave 3 H = 19.7 m T = 14.0 s	Fx_min [MN]	Fx_max [MNm]	My_min [MN]	My_max [MNm]	Fx_abs [MN]	My_abs [MNm]
Computational Fluid Dynamics	-63.9	99.2	-2732	2441	99.2	2732
Linear PF (until FS)	-98.6	98.1	-3112	3097	98.6	3112
Nonlinear PF (FS paneled zone)	-119.3	93.3	-3183	3136	119.3	3183
Nonlinear PF (FS quadrature zone)	-113.3	98.3	-3161	3157	113.3	3161
Nonlinear PF (FS outer circle)	-116.9	96.5	-3170	3145	116.9	3170
Nonlinear PF (FS asymptotic zone)	-117.1	91.8	-3183	3141	117.1	3183
Nonlinear PF (All options)	-114.4	95.1	-3171	3151	114.4	3171

Table B.7: Resulting hydrodynamic loads for the CFD, LPF, and NLPF simulations for wave 4 ($H = 4.0$ m & $T = 7.0$ s).

Wave 4 H = 4.0 m T = 7.0 s	Fx_min [MN]	Fx_max [MNm]	My_min [MN]	My_max [MNm]	Fx_abs [MN]	My_abs [MNm]
Computational Fluid Dynamics	-9.9	10.4	-37.3	42.1	10.4	42.1
Linear PF (until FS)	-10.1	9.9	-41.7	34.3	10.1	41.7
Nonlinear PF (FS paneled zone)	-9.6	10.2	-58.1	44.3	10.2	58.1
Nonlinear PF (FS quadrature zone)	-9.7	10.1	-62.4	45.4	10.1	62.4
Nonlinear PF (FS outer circle)	-9.7	10.1	-60.9	43.5	10.1	60.9
Nonlinear PF (FS asymptotic zone)	-9.5	10.3	-55.0	43.4	10.3	55.0
Nonlinear PF (All options)	-9.7	10.2	-57.9	42.5	10.2	57.9

B.3. Comparison between first-order linear potential flow and second-order nonlinear potential flow⁹⁵

Table B.8: Resulting hydrodynamic loads for the CFD, LPF, and NLPF simulations for wave 5 ($H = 4.0$ m & $T = 9.0$ s).

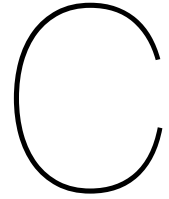
Wave 5 H = 4.0 m T = 9.0 s	Fx_min [MN]	Fx_max [MNm]	My_min [MN]	My_max [MNm]	Fx_abs [MN]	My_abs [MNm]
Computational Fluid Dynamics	-15.1	16.9	-316	353	16.9	353
Linear PF (until FS)	-17.0	17.0	-306	303	17.0	306
Nonlinear PF (FS paneled zone)	-17.0	17.1	-315	303	17.1	315
Nonlinear PF (FS quadrature zone)	-17.1	17.1	-316	302	17.1	316
Nonlinear PF (FS outer circle)	-17.2	16.9	-320	298	17.2	320
Nonlinear PF (FS asymptotic zone)	-16.9	17.2	-311	306	17.2	311
Nonlinear PF (All options)	-17.1	17.0	-317	301	17.1	317

Table B.9: Resulting hydrodynamic loads for the CFD, LPF, and NLPF simulations for wave 6 ($H = 4.0$ m & $T = 11.5$ s).

Wave 6 H = 4.0 m T = 11.5 s	Fx_min [MN]	Fx_max [MNm]	My_min [MN]	My_max [MNm]	Fx_abs [MN]	My_abs [MNm]
Computational Fluid Dynamics	-17.4	20.4	-537	551	20.4	551
Linear PF (until FS)	-20.3	20.3	-566	564	20.3	566
Nonlinear PF (FS paneled zone)	-21.0	20.1	-578	556	21.0	578
Nonlinear PF (FS quadrature zone)	-20.8	20.3	-573	562	20.8	573
Nonlinear PF (FS outer circle)	-20.9	20.2	-576	559	20.9	576
Nonlinear PF (FS asymptotic zone)	-20.9	20.1	-577	557	20.9	577
Nonlinear PF (All options)	-20.9	20.2	-575	560	20.9	575

Table B.10: Resulting hydrodynamic loads for the CFD, LPF, and NLPF simulations for wave 7 ($H = 4.0$ m & $T = 14.0$ s).

Wave 7 H = 4.0 m T = 14.0 s	Fx_min [MN]	Fx_max [MNm]	My_min [MN]	My_max [MNm]	Fx_abs [MN]	My_abs [MNm]
Computational Fluid Dynamics	-19.5	19.0	-595	606	19.5	606
Linear PF (until FS)	-19.9	19.9	-632	631	19.9	632
Nonlinear PF (FS paneled zone)	-20.9	19.7	-635	634	20.9	635
Nonlinear PF (FS quadrature zone)	-20.6	20.0	-635	635	20.6	635
Nonlinear PF (FS outer circle)	-20.8	19.9	-635	634	20.8	635
Nonlinear PF (FS asymptotic zone)	-20.9	19.8	-635	634	20.9	635
Nonlinear PF (All options)	-20.7	19.9	-635	634	20.7	635



Scatter bin diagram for SLS loads

		Tp [s]										
		0-2 1.0	2-4 3.0	4-6 5.0	6-8 7.0	8-10 9.0	10-12 11.0	12-14 13.0	14-16 15.0	16-18 17.0	18-20 19.0	
Hs [m]	Range	AVG	0.0000	0.0076	0.1442	0.1910	0.0910	0.0530	0.0322	0.0134	0.0032	0.0016
	0-2	1.0	0.0000	0.0000	0.0022	0.1664	0.1360	0.0430	0.0190	0.0024	0.0016	0.0012
	2-4	3.0	0.0000	0.0000	0.0000	0.0004	0.0418	0.0260	0.0024	0.0016	0.0014	0.0002
	4-6	5.0	0.0000	0.0000	0.0000	0.0000	0.0002	0.0060	0.0020	0.0018	0.0004	0.0000
	6-8	7.0	0.0000	0.0000	0.0000	0.0000	0.0000	0.0000	0.0010	0.0010	0.0002	0.0000
	8-10	9.0	0.0000	0.0000	0.0000	0.0000	0.0000	0.0000	0.0000	0.0008	0.0004	0.0000
10-12	11.0	0.0000	0.0000	0.0000	0.0000	0.0000	0.0000	0.0000	0.0000	0.0000	0.0000	

Figure C.1: Reduced omnidirectional scatter diagram for a sea with a significant 50-year wave height H_{s50} of 13.0 m, which was obtained from MetoceanView hindcast data [62]. For each range of significant wave heights H_s and peak periods T_p , the average value is considered to reduce the size of the scatter table. The probabilities vary from nonexistent (green), low (yellow), medium (orange), and high (red).

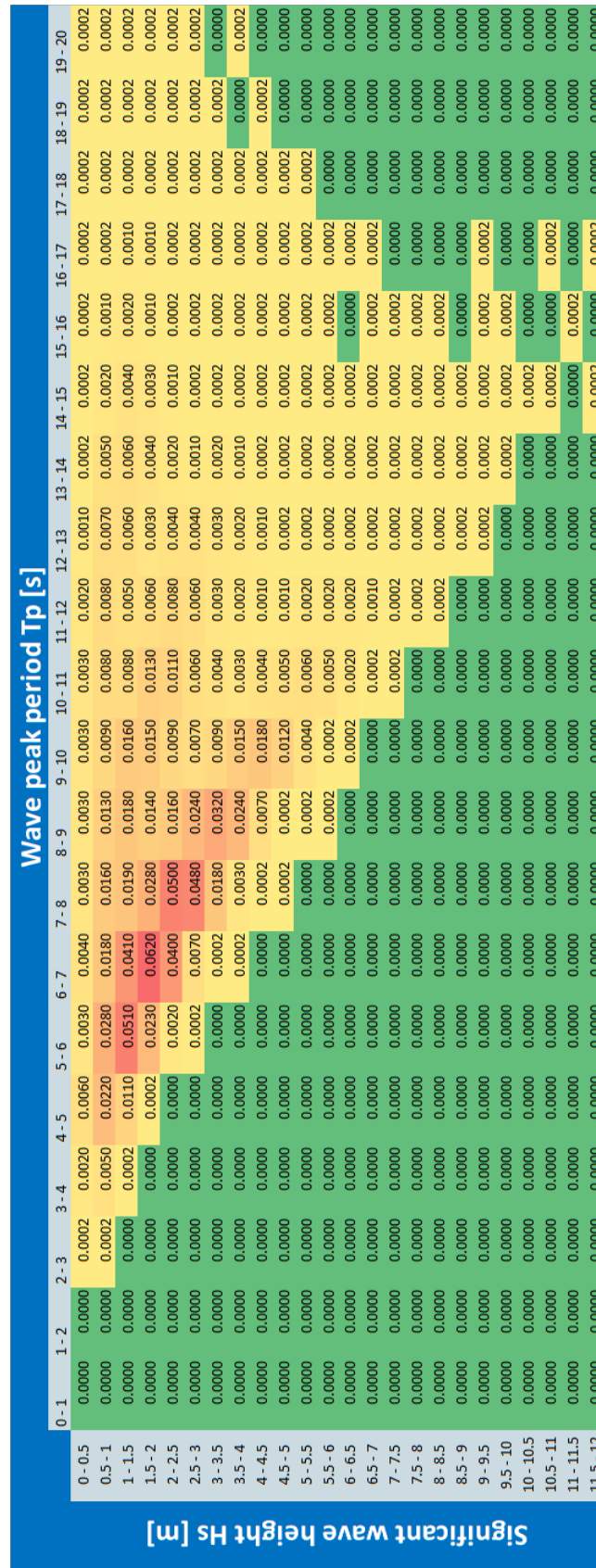
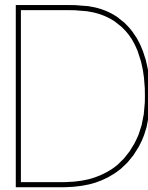


Figure C.2: Complete omnidirectional scatter diagram for a sea with a significant 50 year wave height H_s of 13.0 m, which was obtained from MeteoceanView hindcast data [62].



Sensitivity analysis results

In this appendix, the complete results of the sensitivity analysis from section 6.1 are given for all three design parameters and preliminary design optimizations.

D.1. Base diameter sensitivity analysis

Table D.1: Sensitivity analysis results for the reference GBF with a base diameter of 35.0 m, a cylinder-cone transition point located at -5.0 m, and varying ballast density (1500/2000/2500 kg/m^3).

Load case	LC 1			LC 2				
Ballast density [kg/m^3]	1500	2000	2500	1500	2000	2500		
Base diameter [m]	35.0	35.0	35.0	35.0	35.0	35.0		
Transition point [m]	-5.0	-5.0	-5.0	-5.0	-5.0	-5.0	Volume [m ³]	
Bearing cap. utiliz. [%]	410.5	141.6	100.2	2159	340.3	182.0	Concrete	2679
Sliding cap. utiliz. [%]	69.3	47.6	36.3	107.0	73.7	56.2	Ballast	10857
Overturning cap. utiliz. [%]	84.0	57.8	44.1	85.8	59.1	45.1		
Full contact utiliz. [%]	97.1	66.8	51.0	99.2	68.3	52.1	Cone slope	13.0
1st Nat. frequency [Hz]	0.182	0.151	0.132	0.182	0.151	0.132	[deg]	

Table D.2: Sensitivity analysis results for the reference GBF with a base diameter of 40.0 m, a cylinder-cone transition point located at -5.0 m, and varying ballast density (1500/2000/2500 kg/m^3).

Load case	LC 1			LC 2				
Ballast density [kg/m^3]	1500	2000	2500	1500	2000	2500		
Base diameter [m]	40.0	40.0	40.0	40.0	40.0	40.0		
Transition point [m]	-5.0	-5.0	-5.0	-5.0	-5.0	-5.0	Volume [m ³]	
Bearing cap. utiliz. [%]	191.7	84.2	66.4	1254	213.1	123.1	Concrete	3163
Sliding cap. utiliz. [%]	71.6	47.8	35.8	112.7	75.2	56.4	Ballast	14471
Overturning cap. utiliz. [%]	62.4	41.7	31.3	64.9	43.3	32.5		
Full contact utiliz. [%]	72.2	48.2	36.1	75.0	50.0	37.5	Cone slope	16.2
1st Nat. frequency [Hz]	0.172	0.139	0.120	0.172	0.139	0.120	[deg]	

Table D.3: Sensitivity analysis results for the reference GBF with a base diameter of 45.0 m, a cylinder-cone transition point located at -5.0 m, and varying ballast density (1500/2000/2500 kg/m^3).

Load case	LC 1			LC 2				
	1500	2000	2500	1500	2000	2500		
Ballast density [kg/m^3]	1500	2000	2500	1500	2000	2500		
Base diameter [m]	45.0	45.0	45.0	45.0	45.0	45.0		
Transition point [m]	-5.0	-5.0	-5.0	-5.0	-5.0	-5.0	Volume [m3]	
Bearing cap. utiliz. [%]	118.0	58.5	49.3	886.9	150.4	91.4	Concrete	3687
Sliding cap. utiliz. [%]	73.3	47.6	35.3	116.6	75.8	56.2	Ballast	18653
Overturning cap. utiliz. [%]	46.1	30.0	22.2	47.8	31.1	23.0		
Full contact utiliz. [%]	53.3	34.7	25.7	55.2	35.9	26.6	Cone slope	19.3
1st Nat. frequency [Hz]	0.161	0.128	0.109	0.161	0.128	0.109	[deg]	

Table D.4: Sensitivity analysis results for the reference GBF with a base diameter of 50.0 m, a cylinder-cone transition point located at -5.0 m, and varying ballast density (1500/2000/2500 kg/m^3).

Load case	LC 1			LC 2				
	1500	2000	2500	1500	2000	2500		
Ballast density [kg/m^3]	1500	2000	2500	1500	2000	2500		
Base diameter [m]	50.0	50.0	50.0	50.0	50.0	50.0		
Transition point [m]	-5.0	-5.0	-5.0	-5.0	-5.0	-5.0	Volume [m3]	
Bearing cap. utiliz. [%]	82.8	44.4	39.1	679.3	113.4	71.7	Concrete	4250
Sliding cap. utiliz. [%]	74.2	47.3	34.7	119.1	75.9	55.7	Ballast	23403
Overturning cap. utiliz. [%]	33.4	21.3	15.6	33.4	21.3	15.6		
Full contact utiliz. [%]	38.6	24.6	18.0	38.6	24.6	18.1	Cone slope	22.4
1st Nat. frequency [Hz]	0.152	0.119	0.100	0.152	0.119	0.100	[deg]	

Table D.5: Sensitivity analysis results for the reference GBF with a base diameter of 55.0 m, a cylinder-cone transition point located at -5.0 m, and varying ballast density (1500/2000/2500 kg/m^3).

Load case	LC 1			LC 2				
	1500	2000	2500	1500	2000	2500		
Ballast density [kg/m^3]	1500	2000	2500	1500	2000	2500		
Base diameter [m]	55.0	55.0	55.0	55.0	55.0	55.0		
Transition point [m]	-5.0	-5.0	-5.0	-5.0	-5.0	-5.0	Volume [m3]	
Bearing cap. utiliz. [%]	62.6	35.4	32.4	538.2	89.2	58.3	Concrete	4852
Sliding cap. utiliz. [%]	74.7	46.8	34.0	120.6	75.5	55.0	Ballast	28721
Overturning cap. utiliz. [%]	23.1	14.4	10.5	21.2	13.3	9.7		
Full contact utiliz. [%]	26.7	16.7	12.1	24.5	15.4	11.2	Cone slope	25.3
1st Nat. frequency [Hz]	0.143	0.110	0.093	0.143	0.110	0.093	[deg]	

D.2. Transition point sensitivity analysis

Table D.6: Sensitivity analysis results for the reference GBF with a cylinder-cone transition point located at -10.0 m, a base diameter of 45.0 m, and varying ballast density (1500/2000/2500 kg/m^3).

Load case	LC 1			LC 2				
Ballast density [kg/m^3]	1500	2000	2500	1500	2000	2500		
Base diameter [m]	45.0	45.0	45.0	45.0	45.0	45.0		
Transition point [m]	-10.0	-10.0	-10.0	-10.0	-10.0	-10.0	Volume [m3]	
Bearing cap. utiliz. [%]	85.9	48.4	42.3	440.6	108.5	72.4	Concrete	3573
Sliding cap. utiliz. [%]	68.7	45.3	33.8	108.6	71.7	53.5	Ballast	16755
Overturning cap. utiliz. [%]	41.5	27.4	20.4	38.1	25.1	18.8		
Full contact utiliz. [%]	47.9	31.7	23.6	44.0	29.0	21.7	Cone slope	21.8
1st Nat. frequency [Hz]	0.170	0.137	0.118	0.170	0.137	0.118	[deg]	

Table D.7: Sensitivity analysis results for the reference GBF with a cylinder-cone transition point located at -15.0 m, a base diameter of 45.0 m, and varying ballast density (1500/2000/2500 kg/m^3).

Load case	LC 1			LC 2				
Ballast density [kg/m^3]	1500	2000	2500	1500	2000	2500		
Base diameter [m]	45.0	45.0	45.0	45.0	45.0	45.0		
Transition point [m]	-15.0	-15.0	-15.0	-15.0	-15.0	-15.0	Volume [m3]	
Bearing cap. utiliz. [%]	64.7	40.6	36.5	242.2	80.4	58.0	Concrete	3459
Sliding cap. utiliz. [%]	64.4	43.2	32.5	101.0	67.8	51.0	Ballast	14857
Overturning cap. utiliz. [%]	38.0	25.5	19.2	30.0	20.1	15.2		
Full contact utiliz. [%]	43.9	29.5	22.2	34.6	23.3	17.5	Cone slope	24.9
1st Nat. frequency [Hz]	0.184	0.154	0.134	0.184	0.154	0.134	[deg]	

Table D.8: Sensitivity analysis results for the reference GBF with a cylinder-cone transition point located at -20.0 m, a base diameter of 45.0 m, and varying ballast density (1500/2000/2500 kg/m^3).

Load case	LC 1			LC 2				
Ballast density [kg/m^3]	1500	2000	2500	1500	2000	2500		
Base diameter [m]	45.0	45.0	45.0	45.0	45.0	45.0		
Transition point [m]	-20.0	-20.0	-20.0	-20.0	-20.0	-20.0	Volume [m3]	
Bearing cap. utiliz. [%]	49.9	34.2	31.5	141.9	60.5	46.6	Concrete	3345
Sliding cap. utiliz. [%]	60.0	41.1	31.3	93.3	63.9	48.6	Ballast	12959
Overturning cap. utiliz. [%]	35.5	24.3	18.5	23.3	16.0	12.2		
Full contact utiliz. [%]	41.0	28.1	21.4	27.0	18.5	14.0	Cone slope	28.9
1st Nat. frequency [Hz]	0.199	0.173	0.155	0.199	0.173	0.155	[deg]	

Table D.9: Sensitivity analysis results for the reference GBF with a cylinder-cone transition point located at -25.0 m, a base diameter of 45.0 m, and varying ballast density (1500/2000/2500 kg/m^3).

Load case	LC 1			LC 2				
	1500	2000	2500	1500	2000	2500		
Ballast density [kg/m^3]	1500	2000	2500	1500	2000	2500		
Base diameter [m]	45.0	45.0	45.0	45.0	45.0	45.0		
Transition point [m]	-25.0	-25.0	-25.0	-25.0	-25.0	-25.0	Volume [m3]	
Bearing cap. utiliz. [%]	39.1	28.9	27.2	86.8	45.7	37.5	Concrete	3231
Sliding cap. utiliz. [%]	55.7	39.1	30.1	85.4	60.0	46.2	Ballast	11061
Overturning cap. utiliz. [%]	34.2	24.0	18.5	18.1	12.7	9.8		
Full contact utiliz. [%]	39.5	27.7	21.3	20.9	14.7	11.3	Cone slope	34.2
1st Nat. frequency [Hz]	0.217	0.201	0.187	0.217	0.201	0.187	[deg]	

Table D.10: Sensitivity analysis results for the reference GBF with a cylinder-cone transition point located at -30.0 m, a base diameter of 45.0 m, and varying ballast density (1500/2000/2500 kg/m^3).

Load case	LC 1			LC 2				
	1500	2000	2500	1500	2000	2500		
Ballast density [kg/m^3]	1500	2000	2500	1500	2000	2500		
Base diameter [m]	45.0	45.0	45.0	45.0	45.0	45.0		
Transition point [m]	-30.0	-30.0	-30.0	-30.0	-30.0	-30.0	Volume [m3]	
Bearing cap. utiliz. [%]	33.9	25.9	24.3	61.3	37.3	31.6	Concrete	3117
Sliding cap. utiliz. [%]	51.2	37.0	28.9	77.3	55.8	43.7	Ballast	9163
Overturning cap. utiliz. [%]	38.6	27.9	21.8	21.9	15.8	12.4		
Full contact utiliz. [%]	44.6	32.2	25.2	25.3	18.3	14.3	Cone slope	41.7
1st Nat. frequency [Hz]	0.223	0.211	0.201	0.223	0.211	0.201	[deg]	

D.3. Optimization analysis results for preliminary design

Results for a GBF design with a base diameter of 40.0 m

Table D.11: Sensitivity analysis results for the reference GBF with a cylinder-cone transition point located at -10.0 m, a base diameter of 40.0 m, and varying ballast density (1500/2000/2500 kg/m^3).

Load case	LC 1			LC 2				
	1500	2000	2500	1500	2000	2500		
Ballast density [kg/m^3]	1500	2000	2500	1500	2000	2500		
Base diameter [m]	40.0	40.0	40.0	40.0	40.0	40.0		
Transition point [m]	-10.0	-10.0	-10.0	-10.0	-10.0	-10.0	Volume [m3]	
Bearing cap. utiliz. [%]	140.9	70.5	57.6	635.9	154.5	98.1	Concrete	3069
Sliding cap. utiliz. [%]	67.5	45.7	34.5	105.4	71.3	53.9	Ballast	13057
Overturning cap. utiliz. [%]	58.1	39.4	29.8	55.3	37.5	28.3		
Full contact utiliz. [%]	67.2	45.5	34.4	63.9	43.3	32.7	Cone slope	18.3
1st Nat. frequency [Hz]	0.179	0.147	0.128	0.179	0.147	0.128	[deg]	

Table D.12: Sensitivity analysis results for the reference GBF with a cylinder-cone transition point located at -15.0 m, a base diameter of 40.0 m, and varying ballast density (1500/2000/2500 kg/m^3).

Load case	LC 1			LC 2				
	1500	2000	2500	1500	2000	2500		
Ballast density [kg/m^3]	1500	2000	2500	1500	2000	2500		
Base diameter [m]	40.0	40.0	40.0	40.0	40.0	40.0		
Transition point [m]	-15.0	-15.0	-15.0	-15.0	-15.0	-15.0	Volume [m3]	
Bearing cap. utiliz. [%]	107.9	59.9	50.5	358.1	115.6	79.4	Concrete	2975
Sliding cap. utiliz. [%]	63.6	43.7	33.3	98.3	67.7	51.6	Ballast	11643
Overturning cap. utiliz. [%]	55.1	37.9	28.9	47.6	32.8	25.0		
Full contact utiliz. [%]	63.7	43.8	33.4	55.0	37.8	28.9	Cone slope	21.0
1st Nat. frequency [Hz]	0.191	0.162	0.143	0.191	0.162	0.143	[deg]	

Table D.13: Sensitivity analysis results for the reference GBF with a cylinder-cone transition point located at -20.0 m, a base diameter of 40.0 m, and varying ballast density (1500/2000/2500 kg/m^3).

Load case	LC 1			LC 2				
	1500	2000	2500	1500	2000	2500		
Ballast density [kg/m^3]	1500	2000	2500	1500	2000	2500		
Base diameter [m]	40.0	40.0	40.0	40.0	40.0	40.0		
Transition point [m]	-20.0	-20.0	-20.0	-20.0	-20.0	-20.0	Volume [m3]	
Bearing cap. utiliz. [%]	85.2	51.6	44.4	216.1	88.2	64.8	Concrete	2881
Sliding cap. utiliz. [%]	59.6	41.8	32.2	91.3	64.1	49.4	Ballast	10230
Overturning cap. utiliz. [%]	53.2	37.3	28.8	41.4	29.1	22.4		
Full contact utiliz. [%]	61.5	43.1	33.2	47.8	33.6	25.9	Cone slope	24.5
1st Nat. frequency [Hz]	0.204	0.180	0.163	0.204	0.180	0.163	[deg]	

Table D.14: Sensitivity analysis results for the reference GBF with a cylinder-cone transition point located at -25.0 m, a base diameter of 40.0 m, and varying ballast density (1500/2000/2500 kg/m^3).

Load case	LC 1			LC 2				
	1500	2000	2500	1500	2000	2500		
Ballast density [kg/m^3]	1500	2000	2500	1500	2000	2500		
Base diameter [m]	40.0	40.0	40.0	40.0	40.0	40.0		
Transition point [m]	-25.0	-25.0	-25.0	-25.0	-25.0	-25.0	Volume [m3]	
Bearing cap. utiliz. [%]	69.0	44.9	39.3	137.0	68.1	53.1	Concrete	2786
Sliding cap. utiliz. [%]	55.7	40.0	31.2	84.1	60.4	47.1	Ballast	8816
Overturning cap. utiliz. [%]	52.5	37.7	29.4	36.8	26.4	20.6		
Full contact utiliz. [%]	60.7	43.6	34.0	42.5	30.5	23.8	Cone slope	29.4
1st Nat. frequency [Hz]	0.219	0.204	0.191	0.219	0.204	0.191	[deg]	

Table D.15: Sensitivity analysis results for the reference GBF with a cylinder-cone transition point located at -30.0 m, a base diameter of 40.0 m, and varying ballast density (1500/2000/2500 kg/m^3).

Load case	LC 1			LC 2				
	1500	2000	2500	1500	2000	2500		
Ballast density [kg/m^3]	1500	2000	2500	1500	2000	2500		
Base diameter [m]	40.0	40.0	40.0	40.0	40.0	40.0		
Transition point [m]	-30.0	-30.0	-30.0	-30.0	-30.0	-30.0	Volume [m3]	
Bearing cap. utiliz. [%]	57.3	39.5	34.9	90.5	53.2	43.6	Concrete	2692
Sliding cap. utiliz. [%]	51.6	38.1	30.1	76.7	56.5	44.8	Ballast	7402
Overturing cap. utiliz. [%]	53.2	39.2	31.1	33.9	25.0	19.8		
Full contact utiliz. [%]	61.5	45.3	35.9	39.2	28.9	22.9	Cone slope	36.4
1st Nat. frequency [Hz]	0.223	0.212	0.203	0.223	0.212	0.203	[deg]	

Results for a GBF design with a base diameter of 35.0 m

Table D.16: Sensitivity analysis results for the reference GBF with a cylinder-cone transition point located at -15.0 m, a base diameter of 35.0 m, and varying ballast density (1500/2000/2500 kg/m^3).

Load case	LC 1			LC 2				
	1500	2000	2500	1500	2000	2500		
Ballast density [kg/m^3]	1500	2000	2500	1500	2000	2500		
Base diameter [m]	35.0	35.0	35.0	35.0	35.0	35.0		
Transition point [m]	-15.0	-15.0	-15.0	-15.0	-15.0	-15.0	Volume [m3]	
Bearing cap. utiliz. [%]	237.4	105.0	79.2	633.9	188.3	120.2	Concrete	2530
Sliding cap. utiliz. [%]	62.2	44.1	34.1	94.4	66.9	51.8	Ballast	8867
Overturing cap. utiliz. [%]	77.8	55.2	42.7	69.5	49.3	38.2		
Full contact utiliz. [%]	89.9	63.7	49.4	80.3	57.0	44.1	Cone slope	16.9
1st Nat. frequency [Hz]	0.198	0.171	0.153	0.198	0.171	0.153	[deg]	

Table D.17: Sensitivity analysis results for the reference GBF with a cylinder-cone transition point located at -20.0 m, a base diameter of 35.0 m, and varying ballast density (1500/2000/2500 kg/m^3).

Load case	LC 1			LC 2				
	1500	2000	2500	1500	2000	2500		
Ballast density [kg/m^3]	1500	2000	2500	1500	2000	2500		
Base diameter [m]	35.0	35.0	35.0	35.0	35.0	35.0		
Transition point [m]	-20.0	-20.0	-20.0	-20.0	-20.0	-20.0	Volume [m3]	
Bearing cap. utiliz. [%]	193.6	93.3	71.7	396.1	146.9	100.0	Concrete	2455
Sliding cap. utiliz. [%]	58.8	42.4	33.2	88.2	63.6	49.8	Ballast	7873
Overturing cap. utiliz. [%]	76.5	55.3	43.2	64.0	46.2	36.1		
Full contact utiliz. [%]	88.5	63.9	50.0	73.9	53.4	41.8	Cone slope	19.9
1st Nat. frequency [Hz]	0.208	0.186	0.170	0.208	0.186	0.170	[deg]	

Table D.18: Sensitivity analysis results for the reference GBF with a cylinder-cone transition point located at -25.0 m, a base diameter of 35.0 m, and varying ballast density (1500/2000/2500 kg/m^3).

Load case	LC 1			LC 2				
	1500	2000	2500	1500	2000	2500		
Ballast density [kg/m^3]	1500	2000	2500	1500	2000	2500		
Base diameter [m]	35.0	35.0	35.0	35.0	35.0	35.0		
Transition point [m]	-25.0	-25.0	-25.0	-25.0	-25.0	-25.0	Volume [m3]	
Bearing cap. utiliz. [%]	164.1	84.5	65.8	263.2	117.1	84.4	Concrete	2381
Sliding cap. utiliz. [%]	55.5	40.8	32.3	81.9	60.3	47.8	Ballast	6878
Overturing cap. utiliz. [%]	76.6	56.4	44.7	60.1	44.3	35.1		
Full contact utiliz. [%]	88.5	65.2	51.6	69.5	51.2	40.5	Cone slope	24.0
1st Nat. frequency [Hz]	0.220	0.206	0.195	0.220	0.206	0.195	[deg]	

Table D.19: Sensitivity analysis results for the reference GBF with a cylinder-cone transition point located at -30.0 m, a base diameter of 35.0 m, and varying ballast density (1500/2000/2500 kg/m^3).

Load case	LC 1			LC 2				
	1500	2000	2500	1500	2000	2500		
Ballast density [kg/m^3]	1500	2000	2500	1500	2000	2500		
Base diameter [m]	35.0	35.0	35.0	35.0	35.0	35.0		
Transition point [m]	-30.0	-30.0	-30.0	-30.0	-30.0	-30.0	Volume [m3]	
Bearing cap. utiliz. [%]	144.9	78.4	61.2	184.1	95.3	72.0	Concrete	2306
Sliding cap. utiliz. [%]	52.0	39.2	31.4	75.5	56.9	45.7	Ballast	5883
Overturing cap. utiliz. [%]	78.0	58.9	47.3	58.1	43.8	35.2		
Full contact utiliz. [%]	90.1	68.0	54.6	67.1	50.6	40.6	Cone slope	30.2
1st Nat. frequency [Hz]	0.224	0.213	0.204	0.224	0.213	0.204	[deg]	

Table D.20: Sensitivity analysis results for the reference GBF with a cylinder-cone transition point located at -35.0 m, a base diameter of 35.0 m, and varying ballast density (1500/2000/2500 kg/m^3).

Load case	LC 1			LC 2				
	1500	2000	2500	1500	2000	2500		
Ballast density [kg/m^3]	1500	2000	2500	1500	2000	2500		
Base diameter [m]	35.0	35.0	35.0	35.0	35.0	35.0		
Transition point [m]	-35.0	-35.0	-35.0	-35.0	-35.0	-35.0	Volume [m3]	
Bearing cap. utiliz. [%]	134.3	75.1	58.4	135.6	79.5	62.3	Concrete	2231
Sliding cap. utiliz. [%]	48.6	37.6	30.6	68.9	53.4	43.6	Ballast	4888
Overturing cap. utiliz. [%]	81.0	62.8	51.3	58.0	45.0	36.7		
Full contact utiliz. [%]	93.6	72.6	59.3	67.0	52.0	42.5	Cone slope	40.1
1st Nat. frequency [Hz]	0.225	0.217	0.208	0.224	0.216	0.209	[deg]	

D.4. Three-dimensional plots of sensitivity analysis

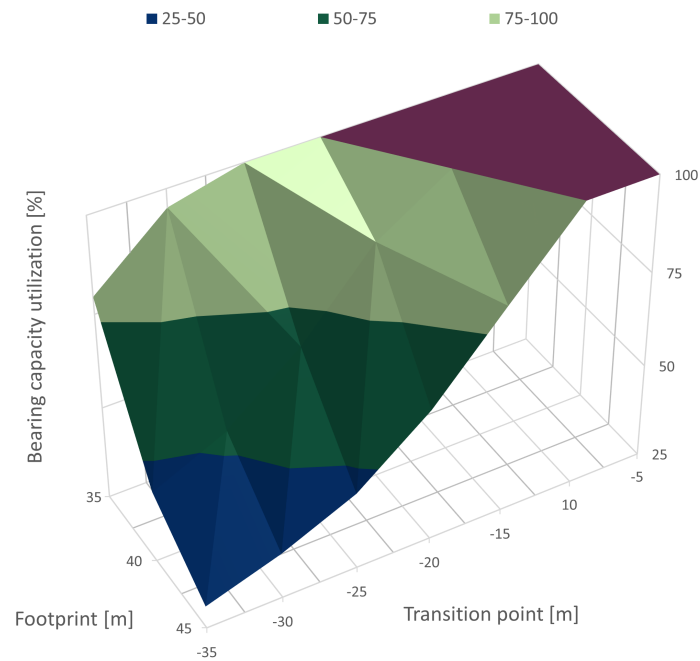


Figure D.1: Three-dimensional plot of the dependency of the bearing capacity utilization ratio on the structure shape (cylinder-cone transition point and footprint). For the ballast and concrete material, a density of 2000 kg/m^3 and 2500 kg/m^3 were used, respectively. Values above the bearing capacity utilization ratio limit of 100% are disregarded.

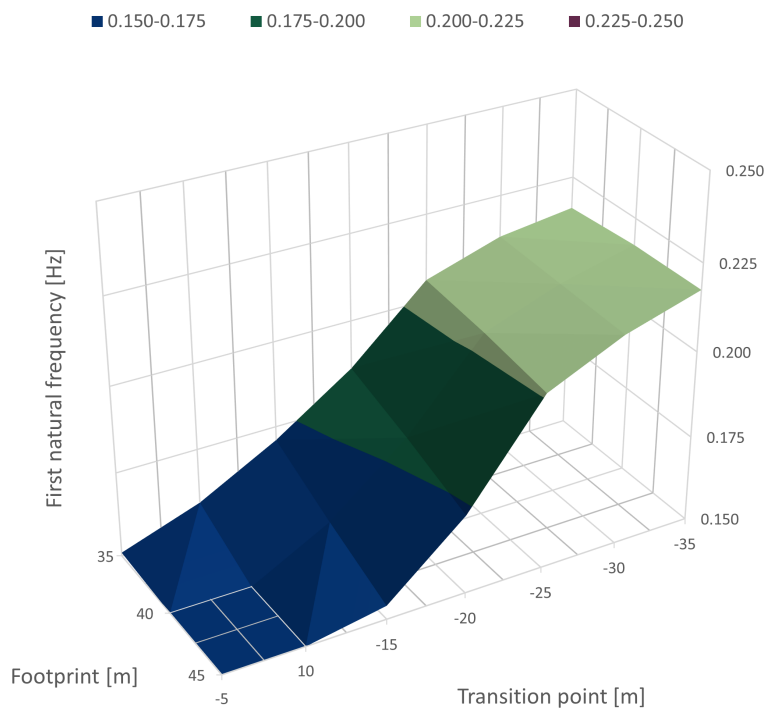


Figure D.2: Three-dimensional plot of the dependency of the first natural frequency on the structure shape (cylinder-cone transition point and footprint). For the ballast and concrete material, a density of 2000 kg/m^3 and 2500 kg/m^3 were used, respectively. Lastly, all the values below the lower limit of the first natural frequency (0.15 Hz) were cut off.

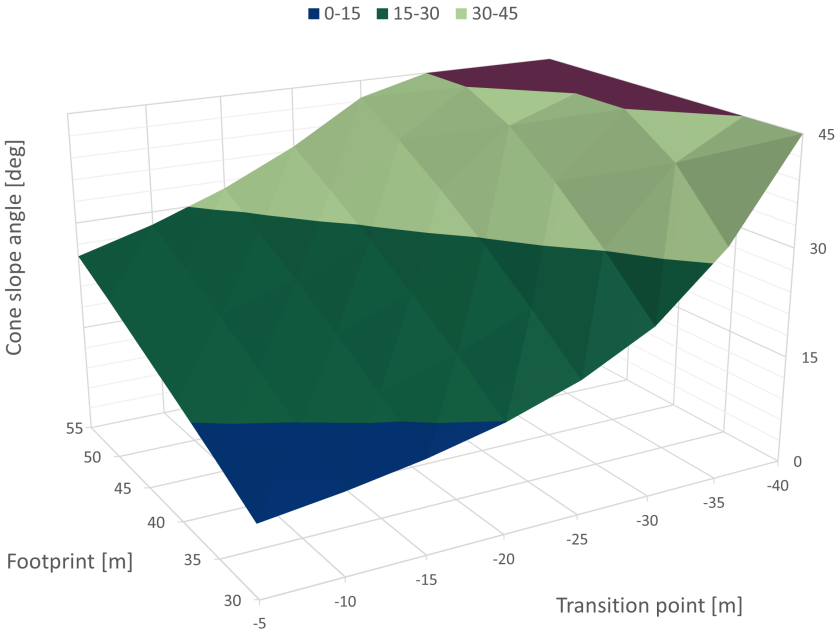


Figure D.3: Three-dimensional plot of the dependency of the cone slope angle on the shape (cylinder-cone transition point and footprint). Values above the cone slope angle limit of 45 degrees are disregarded.

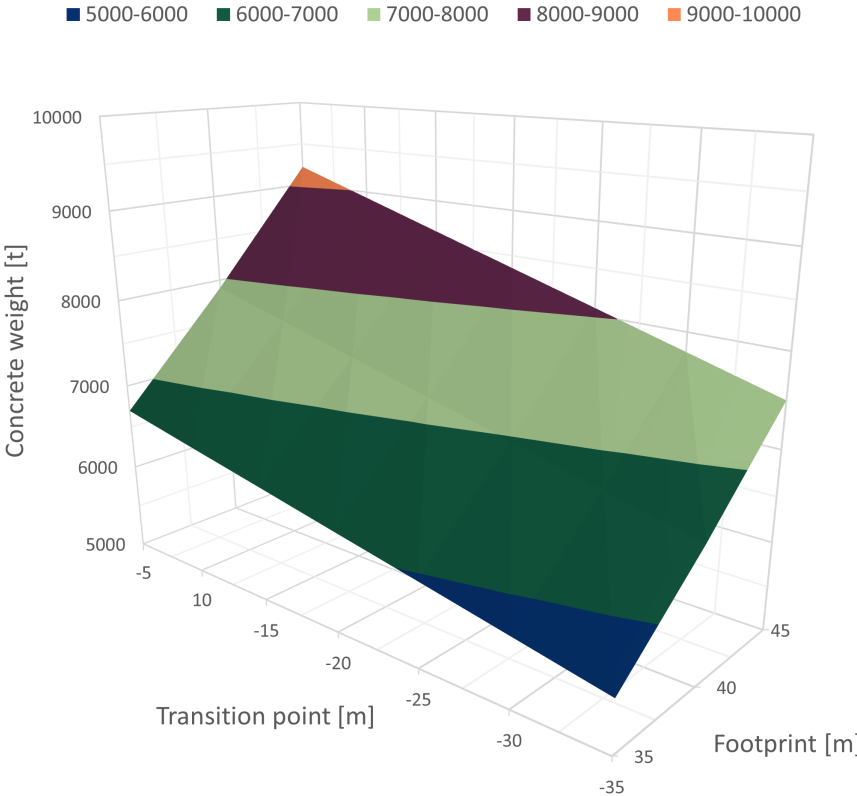


Figure D.4: Three-dimensional plot of the dependency of the required concrete weight on the structure shape (cylinder-cone transition point and footprint). The used reinforced concrete has a density of 2500 kg/m^3 .